Exhumation history of the Qilian Shan, constrained by apatite U-Pb & fission track thermochronology.

Thesis submitted in accordance with the requirements of the University of Adelaide for an Honours Degree in Geology

Christopher Boutsalis

October 2019

Word Count: 7109

19 Figures and 4 Tables

THE UNIVERSITY *of* ADELAIDE

Exhumation history of the Qilian Shan, constrained by apatite U-Pb & fission track thermochronology.

RUNNING TITLE

Exhumation history of the Qilian Shan

ABSTRACT

The NW-SE trending Qilian Shan defines the NE border of Tibet and SE China. This study applies apatite U-Pb and low temperature thermochronology to constrain the exhumation history of the Qilian Shan through the Mesozoic-Cenozoic. AU-Pb and AFT analysis indicate that the eastern Qilian Shan has experienced a 3 stage cooling history since the early Mesozoic, consisting of: (i) rapid initial cooling during the late Triassic-early Jurassic (~240-170 Ma); (ii) either rapid cooling in the middle-late Cretaceous (~130-75 Ma) or a stage of quasi isothermal quiescence, depending on sample elevation and proximity to major E-W faults; and (iii) rapid subsequent cooling during the late Cenozoic (~30-10 Ma). Cooling in the late Triassic-early Jurassic is likely related to the closure of the Palaeo-Asian Ocean and/or the early Triassic Qiangtang collision to Eurasia. The middle-late Cretaceous cooling can be attributed to the collision of the Lhasa Block with southern Eurasia and/or subsequent extension within the Tethys Ocean due to slab roll-back. Finally, the late Cenozoic cooling can be related to the India-Eurasia Collision. Hence, the cooling histories obtained in this study indicate the Qilian Shan has undergone 3 main stages of exhumation in response to far-field tectonic events. Results obtained from this study support previous work done in the Qilian Shan area, improving the overall understanding of strain propagation through Central Asia.

KEYWORDS

Qilian Shan, northeastern Tibet, AFT, thermochronology, fault reactivation, Mesozoic, Cenozoic, Qiangtang, Lhasa, India-Eurasia Collision

TABLE OF CONTENTS

LIST OF FIGURES AND TABLES

1. INTRODUCTION

Large scale intracontinental deformation is widespread in the Eurasian continent that can be predominantly linked to the tectonic history of the closure of the Tethys Ocean at the southern Eurasian margin (Glorie and De Grave 2016). The Cenozoic India-Eurasia collision and ongoing convergence is the latest tectonic event that resulted from the final closure of the Tethys Ocean, which is responsible for large scale propagation of stress and intracontinental orogenesis (Tapponnier et al. 2001, Tapponnier et al. 1986). Plate kinematic studies suggest that India has moved northward approximately 2500 km relative to Asia since the early Cenozoic collision began (Jolivet et al. 2001 and references therein). This convergence between the Indian and Eurasian continents has led to the uplift and lateral expansion of the Tibetan Plateau (Tapponnier et al. 2001, Jolivet et al. 2001). This collision is responsible for mountain building in Central Asia, several thousands of kilometres away from the collisional front (George et al. 2001). Active crustal shortening accommodated by major lithospheric structures, such as the prominent Kunlun and Altyn-Tagh faults, has induced a series of mountain ranges (Kunlun, Altun Shan, Qilian Shan) at the northern edge of the Tibetan Plateau (Tapponnier and Molnar 1977, Jolivet et al. 2001, Tapponnier et al. 1986) (Figure 1). Separating these mountain ranges are intermontane basins hosting several kilometres of Tertiary and Quaternary sediments that are indicative of active erosion over this time period (Metivier et al. 1998). The northwest-southeast trending Qilian Shan is a Cenozoic reactivated thrust belt that defines the northeastern margin of the Tibetan Plateau. Reconnaissance low-temperature thermochronology studies in the Qilian Shan and the surrounding basins have revealed 3 distinct cooling periods: (i) initial rapid cooling in the Cretaceous indicating a period of rapid exhumation and mountain building, (ii) followed by slow cooling until the middle-late Miocene and (iii) rapid cooling rates from the early Miocene to present that built the uplifted Qilian Shan observed today (Qi et al. 2016, George et al. 2001, Baotian et al. 2013, Jolivet et al. 2001). Rapid cooling events in the Qilian Shan have been linked to large scale tectonic processes such as the docking of the Lhasa block in the Cretaceous and the India-Eurasia collision in the Cenozoic (Baotian et al. 2013, Qi et al. 2016). Previous thermochronological studies on the Qilian Shan were mostly undertaken in small study areas, and more systematic studies that investigate the thermo-tectonic history across the crustal architecture are currently lacking. In comparison to previous studies, this work presents the results from apatite fission track (AFT) thermochronology on samples that were collected over a 345 km NE-SW transect across a wide range of elevations (1500-3150m) and structural features (Figure 1). The new AFT data, obtained in this study has been integrated with published data to reveal a more complete picture of the cooling and exhumation history of the Qilian Shan in response to distal tectonic events. Knowledge on the timing and tempo of intracontinental deformation within the Qilian Shan region is key to understanding the propagation of strain through the crustal architecture of eastern Asia. The overall aim of this study is to derive the low-temperature cooling and exhumation history of the Qilian Shan and to correlate it with the tectonic history of the southern Eurasian margin in relation to the progressive consumption of the Tethys Ocean. New thermochronological data are presented for seventeen samples that were analysed by AFT and apatite U-Pb (AU-Pb) methods. In addition, thermal history models were created for samples with high quality AFT data to constrain the cooling and exhumation history of the Qilian Shan Mountain belt.

2. GEOLOGICAL SETTING

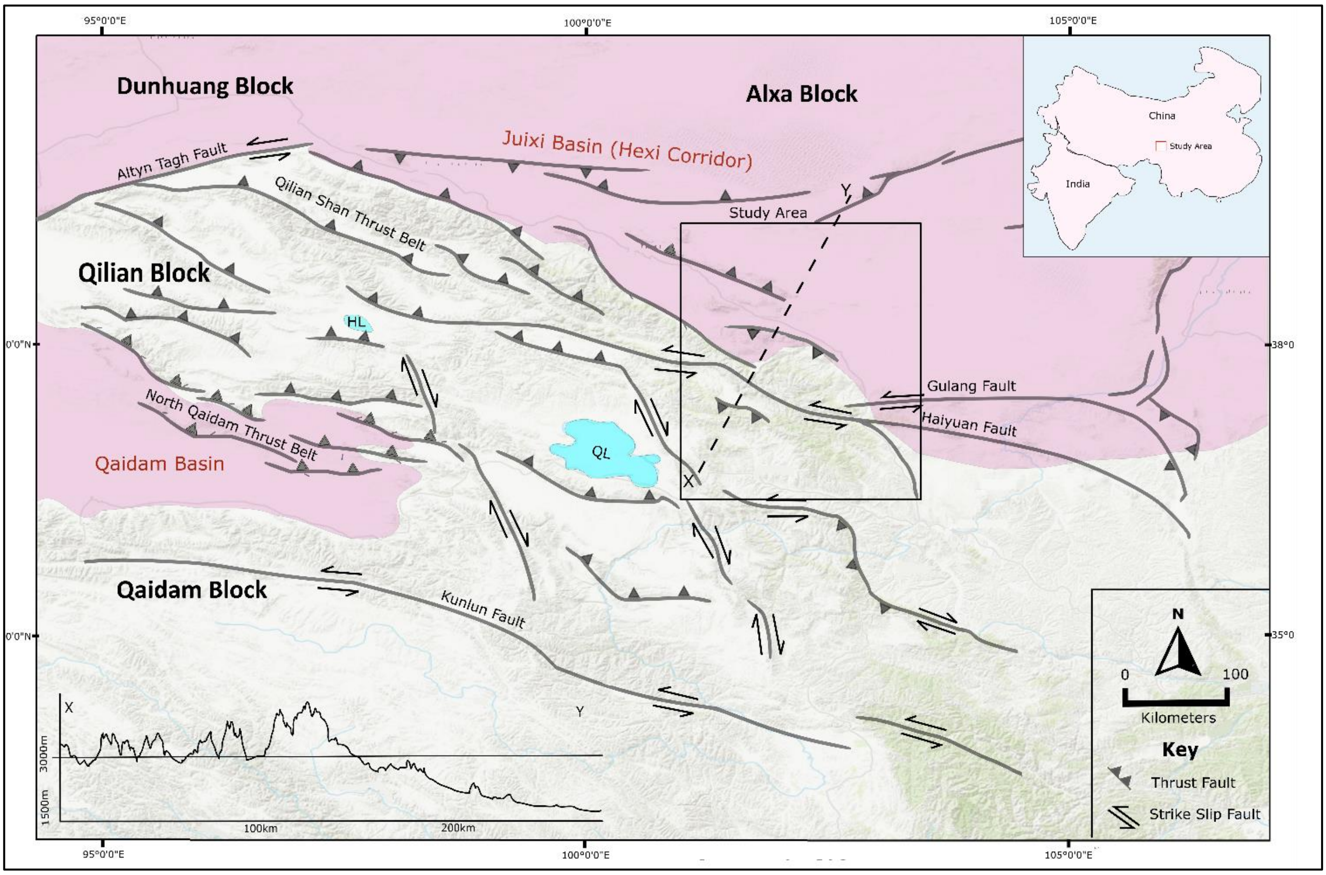

Figure 1 – Topographic map of the Qilian Shan. The shaded pink areas represent adjacent basins, the Hexi Corridor and Qaidam Basin, with the outlined area indicating the study area. The dashed line intersecting the study area represents an elevation transect with the elevation being shown in the bottom right plot. HL and QL represent the Hala Lake and Qinhai Lake respectively.

2.1 Tectonic Structure of the Qilian Shan

The northeastern margin of the Tibetan Plateau is defined by a 500 km wide, northwest-southeast trending fold thrust belt known as the Qilian Shan Mountains (Guo et al. 2009, Qi et al. 2016). The Qilian Shan has traditionally been split into 3 distinct structural units: North, Central and South Qilian Shan (He et al. 2018, Yin and Harrison 2000, Qi et al. 2016, Li et al. 2019, Gehrels et al. 2003). The Central Qilian Shan is separated from the north and south sections by the North Central Qilian fault belt and the South Central Qilian fault belt respectively (Qi et al. 2016). Deformed Palaeozoic arc-type metasedimentary and metavolcanic strata comprise the Northern and Central Qilian Shan (Baotian et al. 2013, George et al. 2001, Zheng et al. 2017) with Precambrian metamorphic basement and Jurassic-Cretaceous groups exposed in some thrust sheets (Guo et al. 2009). The Southern Qilian Shan consists of Ordovician-Silurian sedimentary rocks (Zheng et al. 2017).

Often viewed as the northeast orogenic front of the Tibetan Plateau, the Qilian Shan is characterised by thrust and strike-slip faulting that accommodates northeast convergence (Tapponnier et al. 1990, Zhang et al. 2017). Crustal-scale faulting that has propagated north-eastward across the northern Tibetan Plateau has long been proposed to have deformed the Qilian Shan in a stepwise manner (Tapponnier et al. 2001, Qi et al. 2016, Zheng et al. 2017, Li et al. 2019) with pulses of deformation occurring in the Eocene (Jolivet et al. 2001, Yin et al. 2008a), Oligocene (Xiaomin et al. 2005, Lin et al. 2011) and Miocene (George et al. 2001, Zheng et al. 2017).

2.2 Major Strike-Slip Faults

2.2.1 ALTYN TAGH FAULT SYSTEM

The north-west end of the Qilian Shan is truncated by the Altyn Tagh Fault (Guo et al. 2009) (Figure 1), an ~2000 km long, left-lateral, strike slip fault zone. Left-lateral strike-slip movement along the Altyn Tagh fault is interpreted to have initiated in the early to mid-Eocence and accommodates slip imposed by the extrusion of the Tibetan plateau in the Cenozoic (Cheng et al. 2016, Yin et al. 2002, Cowgill et al. 2003, Wang et al. 2016). Evidenced by the offset of the Eboliang and Huatugou sections in conjunction with sealing of drainage into the northwestern Qaidam Basin, it is interpreted that the Altyn Tagh Fault has been offset ~360 ± 40 km since the early Eocene (Cheng et al. 2016 and references therein). With average slip rates of 9 ± 2 mm/yr, similar to GPS (Global Positioning System) estimates, the Altyn Tagh has been interpreted as steadily deforming over millions of years during continental collision (Yin et al. 2002 and references therein).

2.2.2 HAIYUAN FAULT SYSTEM

The Haiyuan Fault bisects the Central Qilian Shan into its northern and southern portions (Figure 1). The Haiyuan Fault is an active, east-striking, left-lateral strike-slip fault that extends >1000 km in length (Zhang et al. 2017, Li et al. 2009, Jolivet et al. 2012). The initiation of the Haiyuan strike-slip fault has been linked to the most recent phase of rapid cooling and exhumation at ~15-10 Ma (Li et al. 2019, Duvall et al. 2013, Tada et al. 2016). Quaternary slip rates for the Haiyuan Fault vary from 11-19 mm/yr in Central Qilian Shan (Lasserre et al. 1999), <5 mm/yr in the east (Li et al. 2009) and <2-4 mm/yr in the west (Duvall and Clark 2010). The Haiyuan Fault in conjunction with the Altyn Tagh and Kunlun Faults are thought to accommodate the present day deformation related to the India-Eurasia Collision. Previous studies (Jolivet et al. 2012, Gaudemer et al. 1995, Lasserre et al. 1999, Li et al. 2019) interpret slip rates to be showing strain being partitioned between left-lateral east-striking faults (Haiyuan, Kunlun and Gulang) and NNE shortening across thrust systems.

2.2.3 KUNLUN FAULT SYSTEM

The southern end of the Qilian Shan is bordered by the Kunlun Fault, one of the major left-lateral strike-slip faults in northeastern Tibet (Zhang et al. 2014). The Kunlun fault strikes east-west and extends ~1500 km running near parallel to the Haiyuan fault a few hundred km to the northeast (Duvall and Clark 2010) (Figure 1). The initiation age of east-west strike-slip movements is very controversial and varies from the late Eocene (Jolivet et al. 2003) to the late Miocene (Fu and Awata 2007, Kidd and Molnar 1988). While the Kunlun fault presently accommodates lateral extrusion to the east from the India-Eurasia Collision, geodetic and

Quaternary slip rates (10 mm/yr) suggest that a large portion of fast slip is transferred northward in the direction of plate convergence (Duvall and Clark 2010).

2.3 Surrounding Basins

2.3.1 THE QAIDAM BASIN

The Qaidam Basin, located southwest of the Qilian Shan covers an area of ~120,000 km^2 and is the largest intermontane basin along the northeastern margin of the Tibetan Plateau (Hu et al. 2017, Sun et al. 2018). The basement of the Qaidam Basin is composed of Precambrian-Silurian metamorphic rocks, overlain by Devonian-Cenozoic sedimentary strata (Yin et al. 2008b, Metivier et al. 1998). Surrounded on all sides, the Qaidam Basin sources sediments from the Altyn Tagh Mountains to the northwest, Qilian Shan Mountains to the northeast, Ela Mountains to the east and the Kunlun Mountains to the south (Hu et al. 2017, Yin et al. 2008a). Present within the Qaidam Basin are Mesozoic and Cenozoic sedimentary successions between 3-16 km thick (Jian et al. 2013, Fang et al. 2007). The Mesozoic succession is incomplete and features an unconformity of ~40 Ma while the Cenozoic sedimentation is a complete record (~12,000 m) is preserved within the basin with ~3200 m being Quaternary sediments (Hu et al. 2017, Yin et al. 2008a, He et al. 2018, Zheng et al. 2017, Fang et al. 2007). The early Cretaceous Quanyagou *Formation* features red conglomerates coinciding with the timing of the Lhasa collision (Jian et al. 2013). The next stratigraphic units featured in the Qaidam Basin are Cenozoic that sit unconformably upon early Cretaceous rocks. From oldest to youngest, the formations are: the Lulehe *Formation* (Palaeocene-Eocene alluvial conglomerates and gravelly sandstone), Xia Ganchaigou *Formation* (Oligocene alluvial to fluvial conglomerates and gravelly sandstones), Shang Ganchaigou *Formation* (early Miocene sandstones), Xia Youshashan *Formation* (mid Miocene sandstone to mudstone), Shang Youshashan *Formation* (Late Miocene conglomerate and gravelly sandstone), Shizigou *Formation* (Pliocene conglomerate and gravelly sandstone) and the Qiegequan *Formation* (early Pleistocene thick, grey conglomerate intercalated with sandstone) (Fang et al. 2007). Relief differences of up to 2 km between the Qaidam Basin and surrounding mountains have been generated by large boundary faults (Yin and Harrison 2000). While the surrounding mountains uplifted in response to the India-Eurasia Collision (Tapponnier et al. 2001), the Qaidam Basin was shortened (NE-SW), resulting in the basin propagating to the southeast (Wang et al. 1999, Yin et al. 2008b).

2.3.2 THE HEXI CORRIDOR AND JUIXI BASIN

The Hexi Corridor basin, situated immediately north of the Qilian Shan is a narrow topographic depression ~1000 km in length and 20-80 km wide (Guo et al. 2009). The basin sits between 1.5-2 km elevation above sea level and features >2 km thick Cenozoic terrigenous sediments sourced from the Qilian Shan Mountains (Zheng et al. 2017, Pan et al. 2013). The north Qilian Fault, comprised of an array of thrust faults (e.g. the Huangcheng-Taerzhuang fault) separates the Qilian Shan from the Hexi Corridor by a 2-3 km high escarpment (Baotian et al. 2013). This thrust system also controls juxtaposition of low grade metamorphic, early Palaeozoic rocks over Cenozoic sediments within the Hexi Corridor Basin (Zheng et al. 2017).

The Juixi basin, within the Hexi Corridor (Wang et al. 2016) can be divided into 3 structural belts: the southern uplift, central downfolding and northern monocline belt (Guo et al. 2009). The basin features 2-7 km of Mesozoic-Cenozoic strata overlying the southward-tilting basement of the Juixi Basin. Present within the Jiuxi Basin are 5 Cenozoic stratigraphic units (from oldest to youngest) the Huoshaogou *Formation* (Oligocene alluvial conglomerates), Baiyanghe *Formation* (late Oligocene purple mudstones), Shulehe

Formations (Miocene-early Pliocene sandy conglomerates), Yumen *Formation* (early Pliocene conglomerates) and the Jiuquan *Formation* (Quaternary conglomerates) are present within the Juixi Basin (Wang et al. 2016, Zheng et al. 2017). Within the Hexi Corridor Basin, Upper Cretaceous-Eocene Strata are typically absent (Guo et al. 2009, George et al. 2001, Wang and Coward 1993).

2.4.3 THE TARIM BASIN

The Tarim Basin, covering an area of 530,000 km^2 is a giant intermontane basin west of the Qilian Shan. It is situated between the Tian Shan mountain range to the north and the Kunlun Mountain range to the south (Yang et al. 2018). The basement of the Tarim Basin is characterised by Neoarchean to Palaeoproterozoic metamorphic granites, gneisses, schists, marbles quartzite and stromatolitic limestones (Yang et al. 2018). Late Jurassic conglomerates are present within the Tarim Basin coinciding with the collision of the Qiangtang terrane with the Tarim Block (Glorie and De Grave 2016, Chang et al. 2014). In the Central Tarim Basin, Cenozoic strata (sandstones, mudstones and Eocene-Neogene conglomerates) are seen unconformably overlying Mesozoic formations (Chang et al. 2014). The youngest sediments in the basin are made up of a 0-400 m band of Quaternary strata which unconformably overlies the older Cenozoic strata and features conglomerate packages aged at ~2.6 Ma and ~1 Ma (Chang et al. 2014).

2.4 Previous Thermochronology Data

AFT Thermochronological results for the Qilian Shan region are inconsistent, with the history of cooling and exhumation being topics of heavy debate. A study by Li et al. (2019) took samples along the Haiyuan fault and interpreted slow cooling from the late Triassic to early Cenozoic with rapid cooling and exhumation from 10-15 Ma resulting from initiation of the Haiyuan Fault. He et al. (2018) studied Cenozoic synorogenic sediments from the northeastern Qaidam basin and concluded 4 tectonic deformation events occurred during ~60-54 Ma, ~42-38 Ma, ~12 Ma and ~2.1 Ma, linking Cenozoic deformation to the India-Eurasia Collision. Further studies (Qi et al. 2016, Baotian et al. 2013, Guo et al. 2009) all identify cooling periods with little correlation to each other. Both Qi et al. (2016) and Baotian et al. (2013) identify rapid cooling phases during the cretaceous with a long period of quasi isothermal quiescence till the late Eocene (~36 Ma) and Miocene (~24 Ma) respectively, where the cooling rates become rapid. Guo, Lu & Zhang (2009) analyzed samples from the Juixi basin in addition to the Qilian Shan and interpreted rapid cooling due to exhumation initiated in the late Oligocene. Previous studies mentioned above generally correlate periods of rapid cooling within the Cretaceous to be related to the collision and docking of the Lhasa Block. Cenozoic rapid cooling is generally attributed to the India-Eurasia collision, however, the timing of cooling remains controversial.

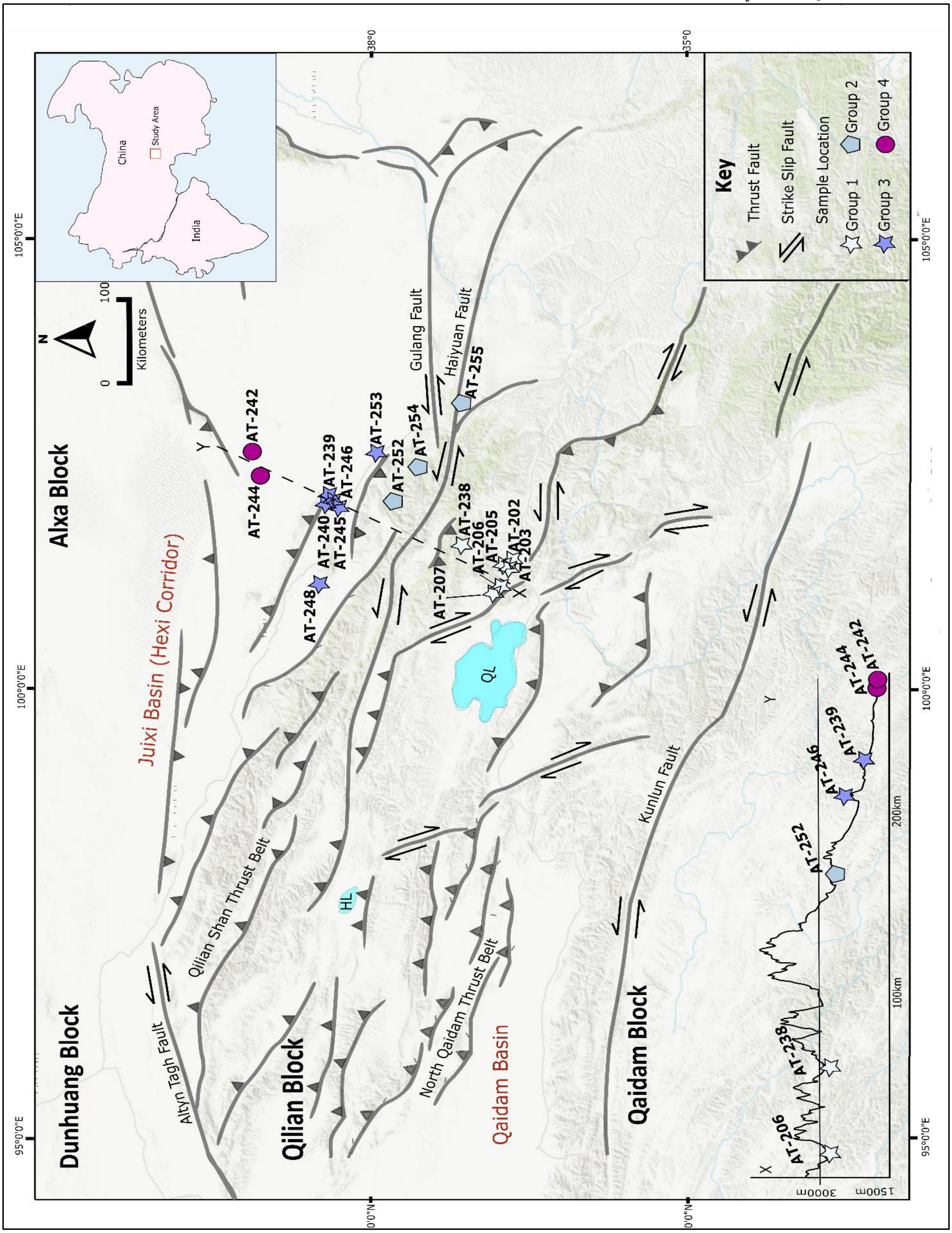

Figure 2 – Topographic map of the Qilian Shan with sample locations and groups shown. Groups are represented by different shapes and colours. The dashed line represents an elevation transect through the study area linking to the elevation plot with samples superimposed upon it. QL and HL represent Qinhai Lake and Hala Lake respectively.

3. METHODS

3.1 Laboratory processing

Samples were collected in the Qilian Shan by Prof. Marc Jolivet and prepared by crushing, sieving and mineral separation using a combination of magnetic and heavy liquid processing at the University of Rennes 1, France. At The University of Adelaide, the apatite grains were mounted in EpoxyCure resin onto thin section slides, then ground and polished to expose the grains (See Appendix A for the complete process outline). Each sample was etched in a solution of 5.5M nitric acid (HNO^3) at 20 ± 0.5°C for 20 ± 0.5 seconds to reveal the natural fission tracks.

3.2 Apatite Fission Track Counting

Apatite grains were imaged with a Zeiss AXIO Imager M2m Autoscan System at a magnification of x1000 using FastTracks software. Using TrackWorks software, fission track densities and confined track (fission tracks that are etched for their full length) lengths were measured. The apatite fission track (AFT) age was calculated using the fission track density and records the timing of passage through the apatite partial annealing zone (APAZ) between ~ 120-60 ° C (Wagner et al. 1989). The confined track length distributions are used in subsequent thermal history modelling to reconstruct the thermal history through the APAZ.

3.3 LA-ICP-MS Analysis

LA-ICP-MS was utilised to determine elemental concentrations (e.g. U, Pb and Cl) in apatite. A laser beam of 29 µm was used, focused on areas of homogeneous fission track density. Each laser ablation session required a block of standards before every block of 10 ‘unknown’ grains. Standard blocks contained 1x Durango, 1x McClure, 2x Madagascar apatite standards and 2x NIST 610 standards.

3.4 Data Reduction

The process of data reduction was achieved using the Iolite software (Paton, Hellstrom, Paul, Woodhead, & Hergt, 2011) utilising the Madagascar apatite as the primary standard for the U-Pb analysis and NIST 610 for the primary standard in AFT analysis. To test the accuracy of the analysed data, secondary standards of Durango (Chew et al. 2014) and McClure (Schoene and Bowring 2006) apatite were used.

Apatite Fission track ages were calculated by comparing the ^{238}U concentrations obtained from the LA-ICP-MS against the number of spontaneous fission tracks in each grain using in-house Excel spreadsheets, following the methodology outlined in (Gillespie et al., 2017) and (Glorie et al., 2017).

Analysis of the standard Durango apatite and the unknown samples were completed simultaneously. A zeta calibration factor was calculated for unknown samples (using the 238U concentrations and fission track densities of Durango apatites) and applied to the calculated AFT ages (Vermeesch 2017) to minimise the uncertainty of fission track analysis, by comparing unknown data to a known standard, in this case Durango apatite.

3.5 ^{252}Cf Fission Fragments Irradiation

Samples in this study with less than 60 confined tracks were exposed to ^{252}Cf fission fragments (dosage = 1.4238 MBQ) in order to induce more confined tracks to assist with thermal history modelling. The samples were exposed to the ^{252}CF fission fragments by loading them onto an unsealed source for 45 minutes under a vacuum.

3.6 Radial Plots

Radial plots were produced using the Java plugin RadialPlotter (Vermeesch, 2009, 2017) in order to determine the central AFT ages and associated uncertainties of samples. Samples that passed the X^2 test (chi^2) with values greater than 0.05 and recorded single grain age dispersions of less than 25% were considered to constrain a single AFT age population. In comparison, samples that failed the X^2 test or recorded single-grain age dispersions greater than 25% were considered to contain multiple age populations (Galbraith & Laslett, 1993). RadialPlotter was used in order to statistically define age populations. Chlorine weight percent (wt %) was input to observe whether trends showing differential annealing of fission tracks were present in the samples. Higher Cl has been correlated with higher closure temperatures in apatite and track which samples are thermally resistant (Green et al. 1986).

3.7 Low Temperature Thermal History Modelling

Thermal history modelling of the samples was completed in the QTQt software (Gallagher, 2012). Inputs used for modelling included single grain AFT age with the uncertainty, number of counted fission tracks, weight percent (wt%) of chlorine within each grain, confined fission track lengths and the angle of the lengths to the C-axis.

The granite samples were constrained beneath the APAZ with U-Pb ages at temperatures of 475± 75ºC in order to model the rock evolution through the APAZ. The models were further constrained to a present day temperature range of 25±5ºC.

A Monte-Carlo approach was used during modelling, with the best models being retained based on the fit between model data and measured data. Initially, the models were conducted by running 10,000 possible models (10,000 Burn-in and 10,000 Post-Burn-in) to determine the plausibility of the thermal history model. Models found to be statistically significant were then further refined by running a second simulation with an extra 200,000 models (200,000 Burn-in and 200,000 Post-Burn-in).

Table 1 - Analytical details for the LA-ICP-MS as used in AFT and AU–Pb dating.

Laser ASI 193	
Type	Excimer laser
Brand and Model	Resonetics M-50-LR
Wavelength	193 nm
Pulse Duration	20 ns
Spot Size	29 um
Repetition Rate	5 Hz
Laser Fluence	~3.5J/cm2
ICP-MS	
Brand and Model	Agilent 7700s
Forward Power	1300W
Gas Flow (L min-1)	
Cool (Ar)	15
Auxiliary (Ar)	0.89
Carrier (He)	0.7
Sample (Ar)	0.93
Data Acquisition Parameters	
Data Acquisition Protocol	Time-resolved analysis
Scanned Masses	29Si, 35Cl, 43Ca, 55Mn, 88Sr, 89Y, 202Hg, 204Pb, 206Pb, 207Pb, 208Pb, 232U, 238U
Detector Mode	Pulse counting
Background Collection	15 s
Ablation for Age Calculation	30 s
Washout	15 s
Standards	
Primary Standards	NIST610, Madagascar Apatite
Secondary Standards	Durango Apatite, McClure Mountain Apatite

4. RESULTS

4.1 Samples

Table 2 – Sample locations, elevations and lithology details.

Sample	Latitude	Longitude	Elevation (m)	Lithology
AT-202	36.669	101.4059	2550	Granitoid
AT-203	36.674	101.3576	2611	Gneiss
AT-205	36.674	101.3569	2597	Leucocrate Granite
AT-206	36.776	101.1222	2927	Pink Granite
AT-207	36.846	101.0660	2958	Gneiss
AT-238	37.139	101.5728	2850	Deformed Granite
AT-239	38.389	102.1203	1691	Granite
AT-240	38.389	102.1203	1691	Red Granite
AT-242	39.156	102.5675	1508	Diorite??
AT-244	39.080	102.4545	1585	Gneiss
AT-246	38.345	102.0417	1800	Biotite Granite
AT-248	38.493	101.1485	2226	Gneiss
AT-252	37.889	102.1727	2319	Pink Granite
AT-253	37.882	102.5386	1816	Granodiorite
AT-254	37.518	102.4078	3066	Granite
AT-255	37.139	103.1850	3142	Large Grained Granite

A total of twenty-three samples were collected (Figure 2). Sixteen samples were analysed using the AFT and AU-Pb methods (7 samples were removed due to low abundance of apatite). Sample locations and rock descriptions are listed in Table 2 with their locations shown in Figure 2.

Samples in this study were grouped into 4 different fault blocks with respect to the main fault architecture, in order to observe whether differential exhumation between the fault blocks is present.

- Group 1 consisted of six samples, AT-202, AT-203, AT-205, AT-206, AT-207 and AT-238. The samples were collected in in Central Qilian Shan, China and recorded AFT ages spanning the Late Triassic – Middle Cretaceous.

- Group 2 consisted of three samples, AT-252, AT-254 and AT-255. The samples were collected in the Central Qilian Shan, China and recorded AFT ages spanning Early – Late Cretaceous.

- Group 3 consisted of six samples, AT-239, AT-240, AT-246, AT-248 and AT-253. The samples were collected in the Northern Qilian Shan, China and recorded AFT ages spanning Late Jurassic – Late Cretaceous.

- Group 4 consisted of two samples, AT-242 and AT-244. The samples were collected in the Juixi Basin (North of Qilian Shan) China and recorded AFT ages spanning Late Triassic – Early Jurassic.

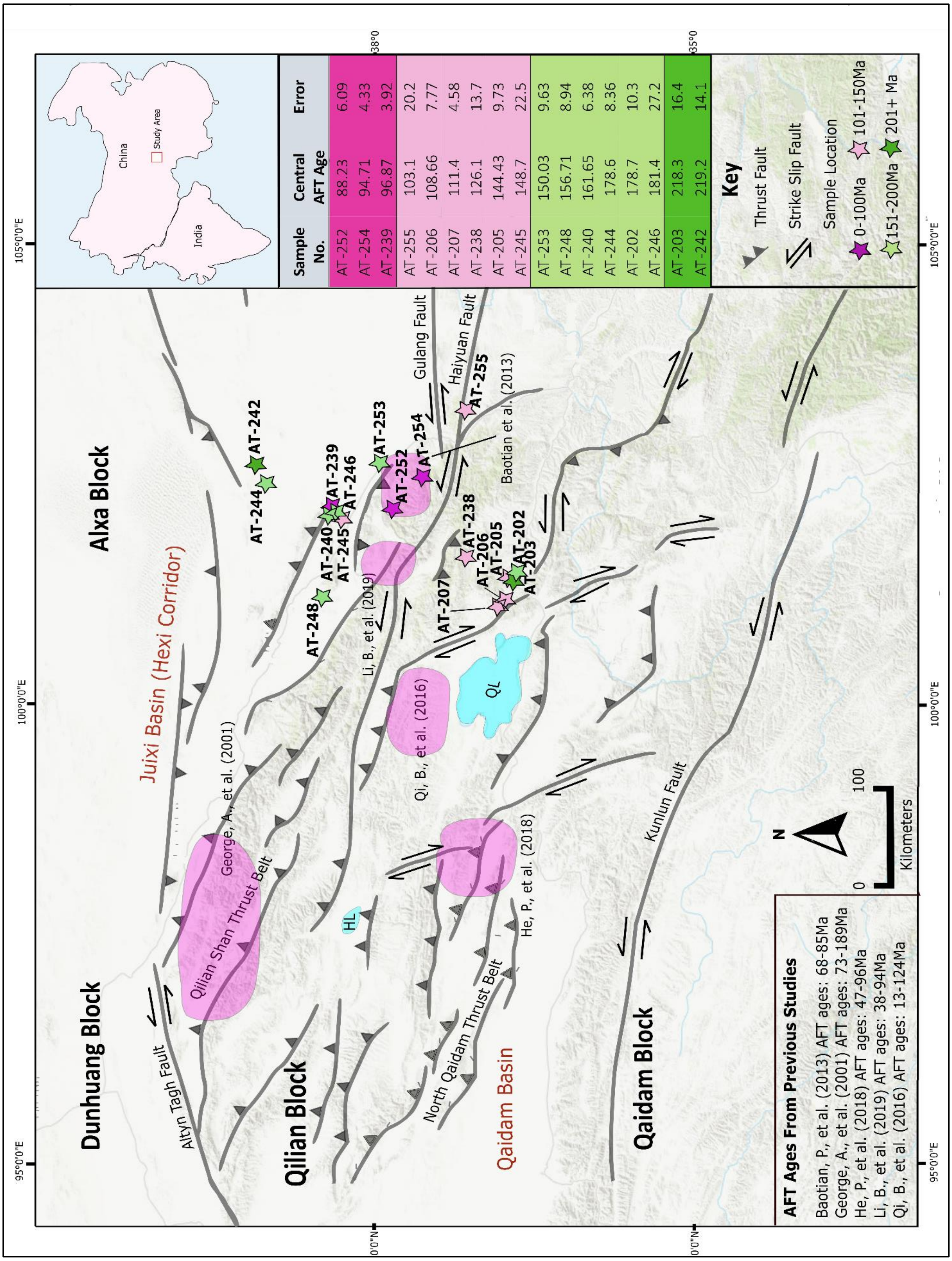

Figure 3 – Topographic map of the Qilian Shan featuring study areas of previously published data (Pink Zones). The coloured stars represent the AFT ages of the samples. Green = 0-100 Ma, Yellow = 101-150 Ma, Blue = 151-200 Ma and Red = 200+ Ma. Full AFT ages of the samples are listed on the right side of the map. Black zones represent sample groups and succeed south to north, with Group 1 being the most southernmost.

4.2 Apatite fission track results

Table 3 – AFT summary table organised by groups. ρs represents the density of fission tracks within each sample, Ns represents the total number of tracks within the sample, n represents the amount of grains used for analysis within each sample. ^{35}Cl and ^{238}U represent the concentration in ppm within the analysed grains with 1σ being the uncertainty on these values. t represents the central AFT age in Ma calculated using RadialPlotter (Vermeesch, 2009) with 1σ representing the associated uncertainty. nl is the number of confined lengths measured within the sample, with MTL representing the mean track length and SD being the 1σ standard deviation of distribution. Disp represents the % of dispersion among single grain ages and P(x^2) represents the probability of the analysed grains belonging to a single population, calculated with RadialPlotter.

ample	ρs ($x10^5/cm^2$)	Ns	n	35Cl (ppm)	1σ (ppm)	238U (ppm)	1σ (ppm)	t (Ma)	1σ (Ma)	nl	MTL (µm)	SD (µm)	Disp (%)	P(χ^2)
Group 1														
AT-202	45.1	1211	22	692	200	47.60	1.04	179	10	100	11.59	1.77	23.14	0
AT-203	20.1	672	25	684	202	16.98	0.56	218	16	90	10.11	2.13	31	0
AT-205	29.9	221	6	467	188	38.70	0.73	144	10	95	10.95	2.28	0	0.89
AT-206	18.4	647	18	796	224	22.26	0.68	109	8	86	10.46	2.16	20.1	0.0054
AT-207	9.5	850	37	499	192	15.98	0.43	111	5	100	11.39	2.32	13.13	0.068
AT-238	33.1	530	14	531	212	52.70	1.35	126	14	98	10.98	2.02	36.8	0
Group 2														
AT-252	21.5	1784	24	887	221	45.66	1.03	88	6	99	11.22	1.96	31.41	0
AT-254	24.6	1841	31	875	203	49.08	1.04	95	4	99	11.57	1.75	21.25	0
AT-255	4.5	23	3	1117	178	5.27	0.18	103	20	16	11.88	1.87	0	0.55
Group 3														
AT-239	11.8	604	20	446	180	22.81	0.58	97	4	91	11.52	2.10	0	0.64
AT-240	18.28	1182	30	464	204	21.32	0.53	162	6	100	11.12	2.26	13.58	0.007
AT-246	13.5	731	26	616	195	14.22	0.40	181	14	97	11.40	1.89	33.5	0
AT-248	11.1	341	18	1270	245	13.68	0.38	157	9	100	11.38	1.85	6.79	0.32
AT-253	10.3	517	25	354	130	12.29	0.29	150	10	97	11.63	2.16	22.5	0.00085
Group 4														
AT-242	10.9	364	23	3326	350	9.17	0.31	223	14	78	11.46	2.28	16.3	0.084
AT-244	14.2	860	18	1144	215	14.25	0.34	179	8	94	11.94	2.28	12.95	0.015

4.2.1 DATA ACCURACY

Durango apatite was used for zeta calibration (Vermeesch 2017) of single-grain AFT ages for unknown apatite samples. The weighted average AFT age yielded by Durango apatite in this work was 31.45 ± 2.17 Ma (Figure 4). This is within the uncertainty of the published $^{40}Ar/^{39}Ar$ age of 31.4 4 ± 0.18 Ma (McDowell et al. 2005), suggesting reliable fission track age results.

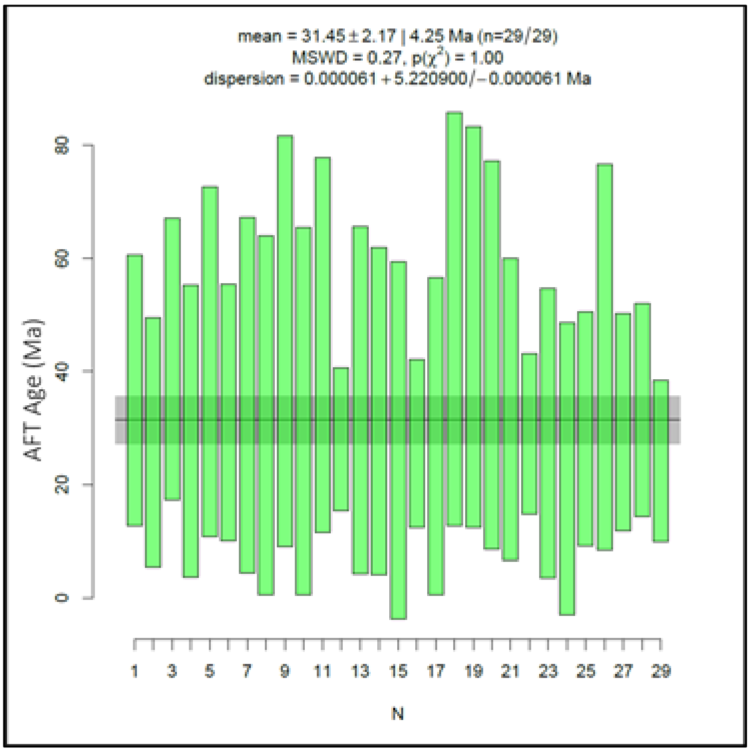

Figure 4 – AFT weighted average for primary standard Durango Apatite

4.2.2 GROUP 1

Central AFT ages within Group 1 range from 218 ± 32 Ma to 109 ± 15 Ma (Figure 5). In more detail, samples AT-202, AT-203, AT-205, AT-206, AT-207 and AT-238 yield central AFT ages of 179 ± 10 Ma, 218 ± 16 Ma, 144 ± 10 Ma, 109 ± 8 Ma, 111 ± 5 Ma and 126 ± 14 Ma respectively. Two samples passed the χ^2 test and yield single-grain age population dispersions of <25% (AT-205 and AT-207) suggesting each sample records a single-grain age population. Four samples failed the χ^2 test (AT-202, AT-203, AT-206 and AT-238) with two yielding single-grain age dispersions of >25% (AT-203 & AT-238) suggesting these samples likely contain multiple age populations. Sufficient number of confined tracks (>80) were measured in all samples, producing mean track lengths of 11.59 ± 1.77 µm, 10.11 ± 2.13 µm, 10.95 ± 2.28 µm, 10.46 ± 2.16 µm, 11.39 ± 2.32 µm and 10.98 ± 2.02 µm respectively (Table 3, Figure 5). The pooled radial plot for Group 1 yields a central AFT age of 152 ± 5 Ma and yields two statistically defined age peaks, with Peak 1 AFT age of 113 ± 5 Ma and Peak 2 AFT age of 207 ± 7 Ma (Figure 5). No observable Cl trends are seen within the samples of Group 1, suggesting samples have not undergone differential annealing of fission tracks.

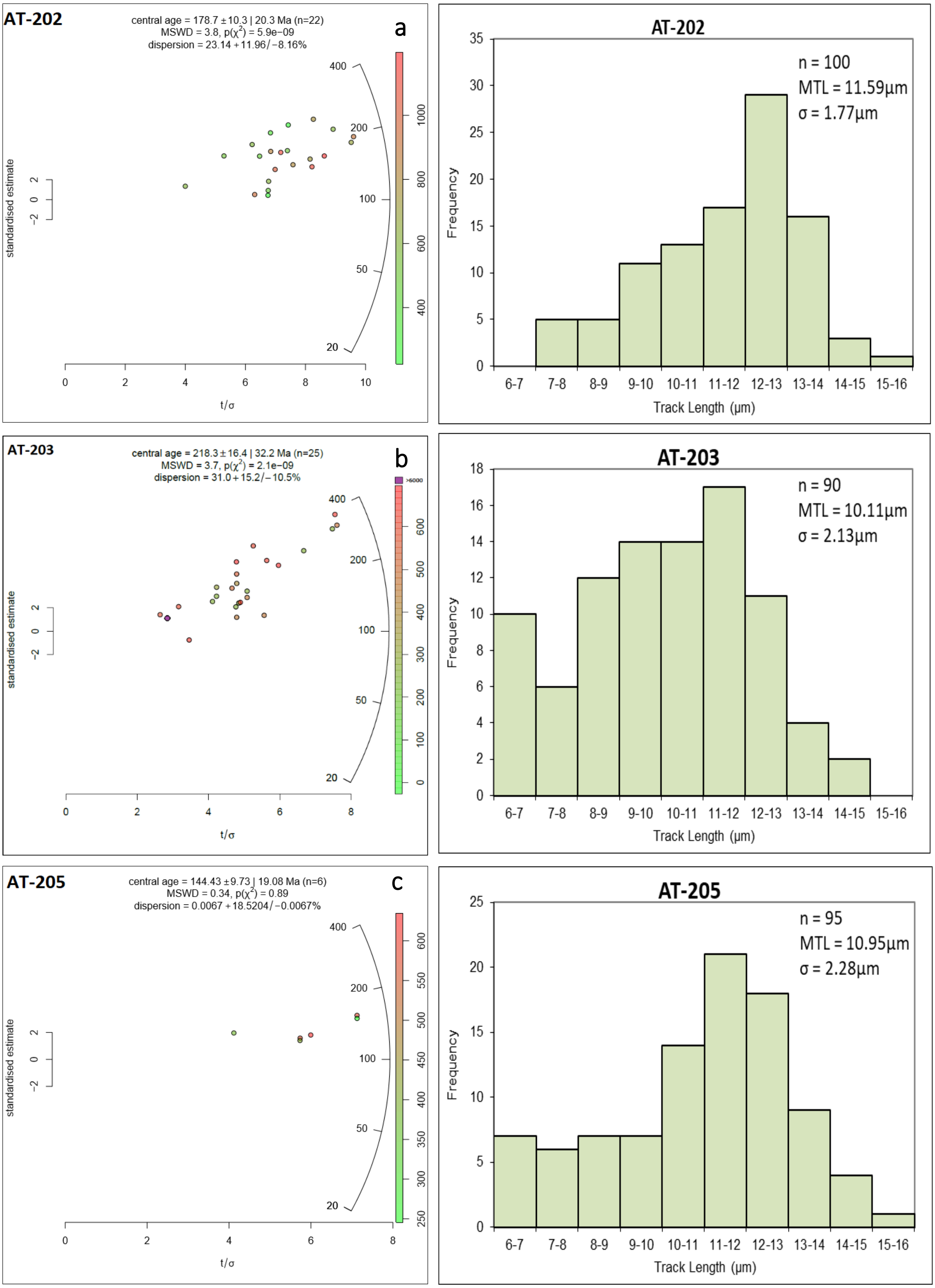
AT-202
central age = 178.7 ± 10.3 | 20.3 Ma (n=22)
MSWD = 3.8, p(χ2) = 5.9e−09
dispersion = 23.14 + 11.96/ −8.16%
a
standardised estimate
t/σ
AT-202
n = 100
MTL = 11.59µm
σ = 1.77µm
Frequency
Track Length (µm)
AT-203
central age = 218.3 ± 16.4 | 32.2 Ma (n=25)
MSWD = 3.7, p(χ2) = 2.1e−09
dispersion = 31.0 + 15.2/ −10.5%
b
standardised estimate
t/σ
AT-203
n = 90
MTL = 10.11µm
σ = 2.13µm
Frequency
Track Length (µm)
AT-205
central age = 144.43 ± 9.73 | 19.08 Ma (n=6)
MSWD = 0.34, p(χ2) = 0.89
dispersion = 0.0067 + 18.5204/ −0.0067%
c
standardised estimate
t/σ
AT-205
n = 95
MTL = 10.95µm
σ = 2.28µm
Frequency
Track Length (µm)

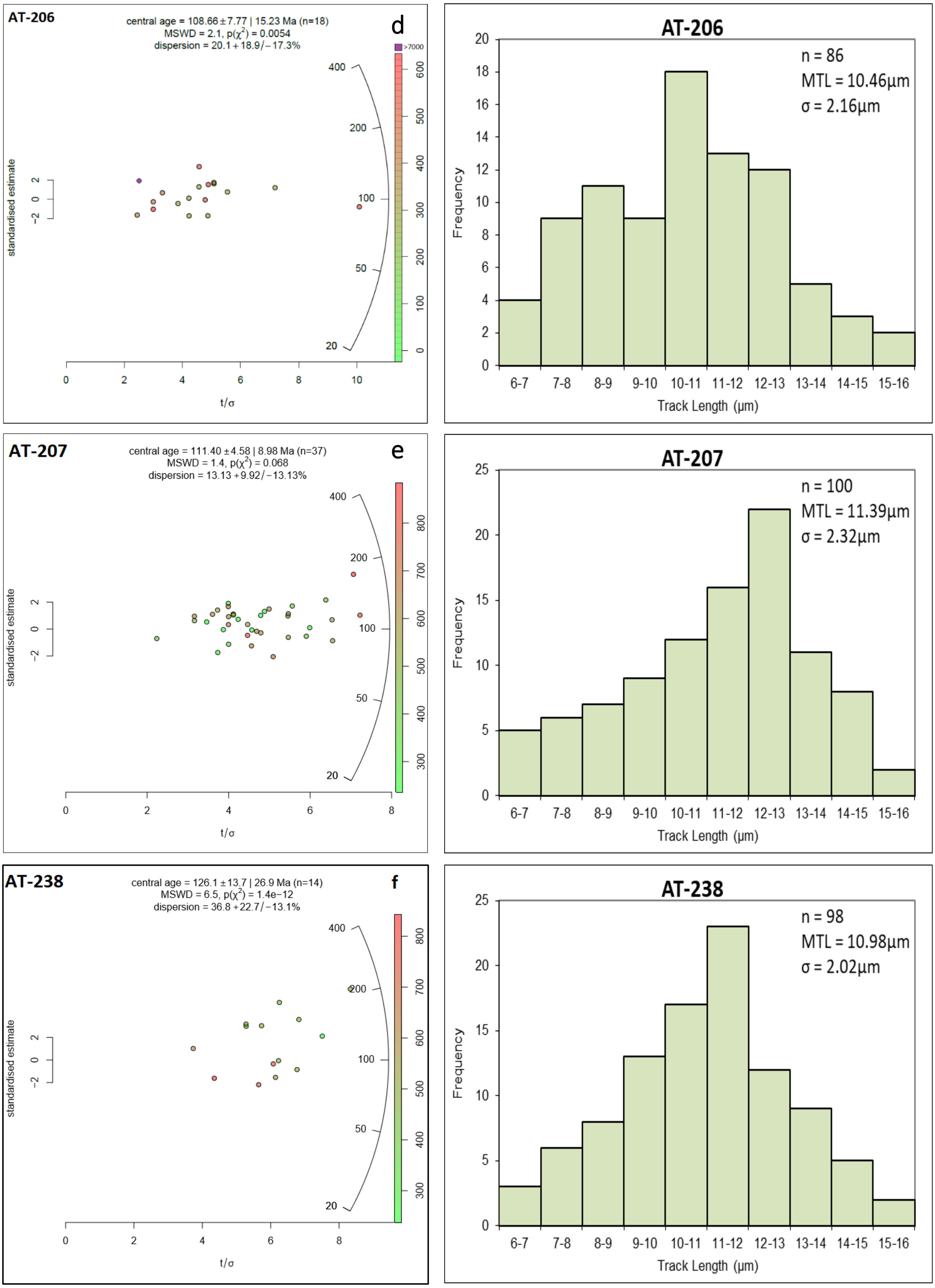
AT-206
central age = 108.66 ± 7.77 | 15.23 Ma (n=18)
MSWD = 2.1, p(χ2) = 0.0054
dispersion = 20.1 + 18.9/ − 17.3%
d
standardised estimate
t/σ
AT-206
n = 86
MTL = 10.46μm
σ = 2.16μm
Frequency
Track Length (μm)
AT-207
central age = 111.40 ± 4.58 | 8.98 Ma (n=37)
MSWD = 1.4, p(χ2) = 0.068
dispersion = 13.13 + 9.92/ − 13.13%
e
standardised estimate
t/σ
AT-207
n = 100
MTL = 11.39μm
σ = 2.32μm
Frequency
Track Length (μm)
AT-238
central age = 126.1 ± 13.7 | 26.9 Ma (n=14)
MSWD = 6.5, p(χ2) = 1.4e−12
dispersion = 36.8 + 22.7/ − 13.1%
f
standardised estimate
t/σ
AT-238
n = 98
MTL = 10.98μm
σ = 2.02μm
Frequency
Track Length (μm)

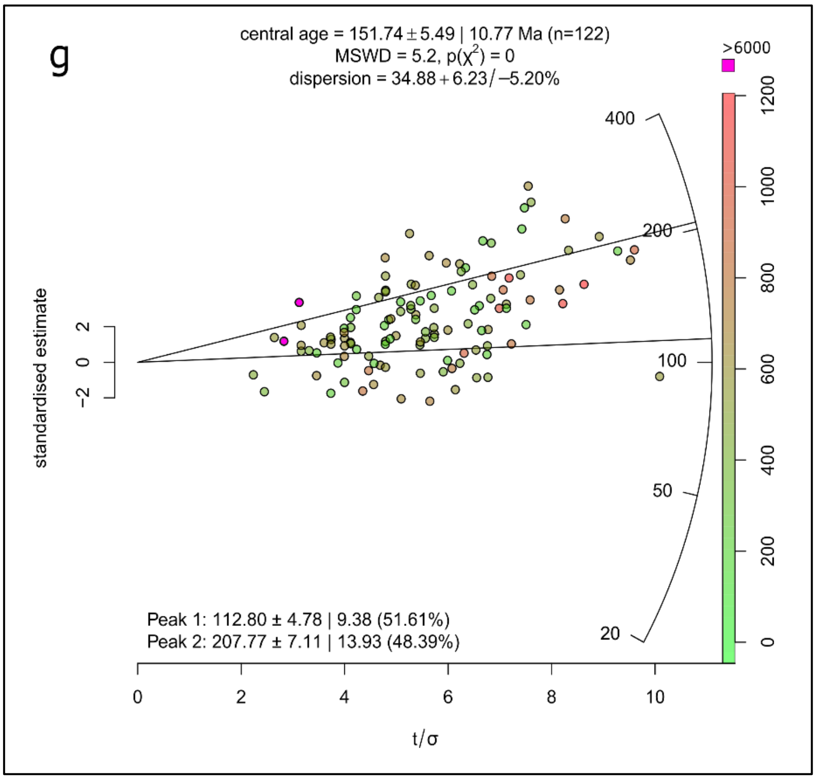

Figure 5 – Radial plots of calculated AFT ages for samples within Group 1 (a-f) and a combined radial plot (g) containing all analysed grains in Group 1. Central AFT age values and age peaks were calculated with the RadialPlotter software (Vermeesch, 2009). The percentage of data within each peak is bracketed next to the peak ages. The right hand side coloured scale represents the concentration of ^{35}Cl in ppm within each of the analysed grains. The y-axis to the left represents the 2σ error from the central AFT values with the right y-axis representing the age in Ma. The x-axis represents the uncertainty in the single grain ages and decreases from left to right. The frequency plots represent the mean track length of confined fission tracks within each sample. Number of tracks measured (n), mean track length (MTL) and standard deviation of measured track lengths (σ) are featured in the right corner of the plots.

4.2.2 GROUP 2

Central AFT ages within Group 2 range from 103± 20 Ma to 88 ± 6 Ma (Figure 6). In more detail, samples AT-252, AT-254 and AT-255 yield central AFT ages of 88 ± 6 Ma, 95 ± 4 Ma and 103 ± 20 Ma respectively. One sample passed the χ^2 test and yield single age population dispersions of <25% (AT-255) suggesting the sample records a single-grain age population. Two samples failed the X^2 test (AT-252 & AT-254), with one yielding a single-grain age dispersion of >25% (AT-252) suggesting these sample likely contain multiple grain age populations. 99 confined tracks were measured in samples AT-252 and AT-254, producing mean track lengths of 11.22 ± 1.96 μm and 11.57 ± 1.75 μm respectively. Only 16 confined tracks were measured in sample AT-255 producing a mean track length of 11.88 ± 1.87 μm (Table 3, Figure 6). The pooled radial plot for Group 2 yields a central AFT age of 92 ± 4 Ma and yields two statistically defined age peaks, with Peak 1 AFT age of 72 ± 3 Ma and Peak 2 AFT age of 11 3± 8 Ma (Figure 6). No observable Cl trends are seen within the samples of Group 2, suggesting samples have not undergone differential annealing of fission tracks.

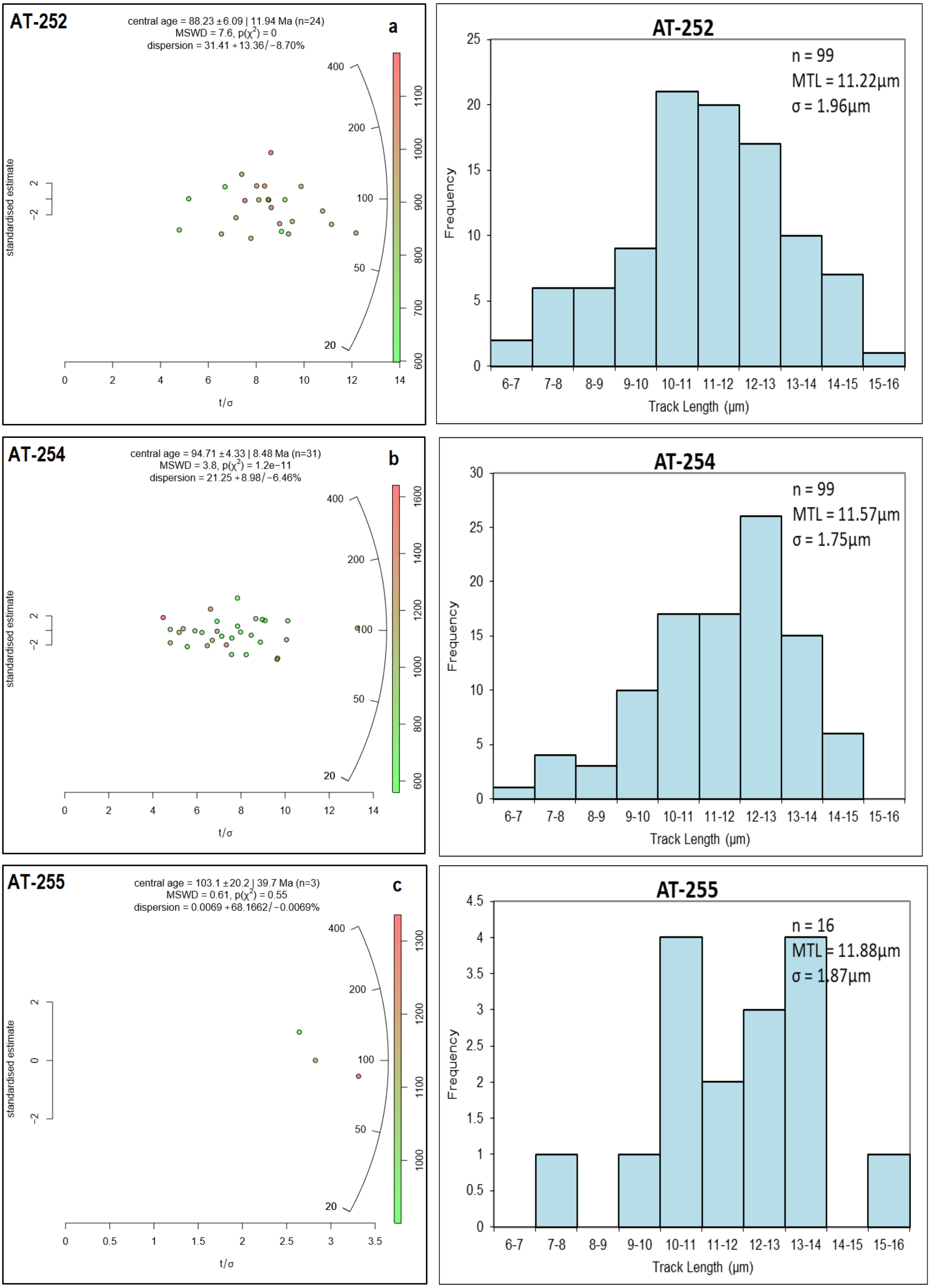
AT-252
central age = 88.23 ±6.09 | 11.94 Ma (n=24)
MSWD = 7.6, p(χ2) = 0
dispersion = 31.41 +13.36/−8.70%
a
standardised estimate
t/σ
AT-252
n = 99
MTL = 11.22µm
σ = 1.96µm
Frequency
Track Length (µm)
AT-254
central age = 94.71 ±4.33 | 8.48 Ma (n=31)
MSWD = 3.8, p(χ2) = 1.2e−11
dispersion = 21.25 +8.98/−6.46%
b
standardised estimate
t/σ
AT-254
n = 99
MTL = 11.57µm
σ = 1.75µm
Frequency
Track Length (µm)
AT-255
central age = 103.1 ±20.2 | 39.7 Ma (n=3)
MSWD = 0.61, p(χ2) = 0.55
dispersion = 0.0069 +68.1662/−0.0069%
c
standardised estimate
t/σ
AT-255
n = 16
MTL = 11.88µm
σ = 1.87µm
Frequency
Track Length (µm)

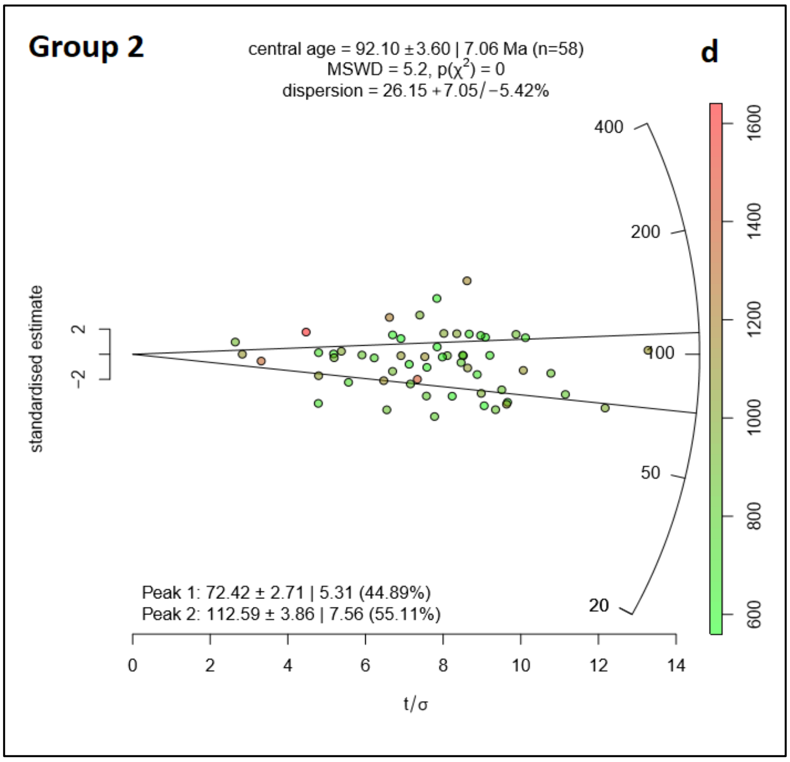

Figure 6 – Radial plots of calculated AFT ages for samples associated with Group 2 (a-c) and a pooled sample radial plot (d) with all analysed grains in Group 2 (caption as in Figure 5).

4.2.3 GROUP 3

Central AFT ages within Group 3 range from 181 ± 14 Ma to 97 ± 4 Ma (Figure 7). In more detail, samples AT-239, AT- AT-240, AT-246, AT- 248 and AT-253 yield central AFT ages of 97 ± 4 Ma, 162 ± 6 Ma, 181 ± 14 Ma, 157 ± 9 Ma and 150 ± 10 Ma respectively. Two samples passed the χ^2 test and yield single-grain age population dispersions of <25% (AT-239 and AT-248) suggesting each sample records a single-grain age population. Three samples failed the χ^2 test (AT-240, AT-246 and AT-253) suggesting these samples likely contain multiple age populations. Sufficient number of confined tracks (>90) were measured in all samples producing mean track lengths of 11.52 ± 2.1 µm, 11.12 ± 2.26 µm, 11.4 ± 1.89 µm, 11.38 ± 1.85 µm and 11.63 ± 2.16 µm respectively (Table 3, Figure 7). The pooled radial plot for Group 3 yields a central AFT age of 148 ± 5 Ma and yields two statistically defined age peaks, with Peak 1 AFT age of 115 ± 5 Ma and Peak 2 AFT age of 189 ± 7 Ma (Figure

7). No observable Cl trends are seen within the samples of Group 3, suggesting samples have not undergone differential annealing of fission tracks.

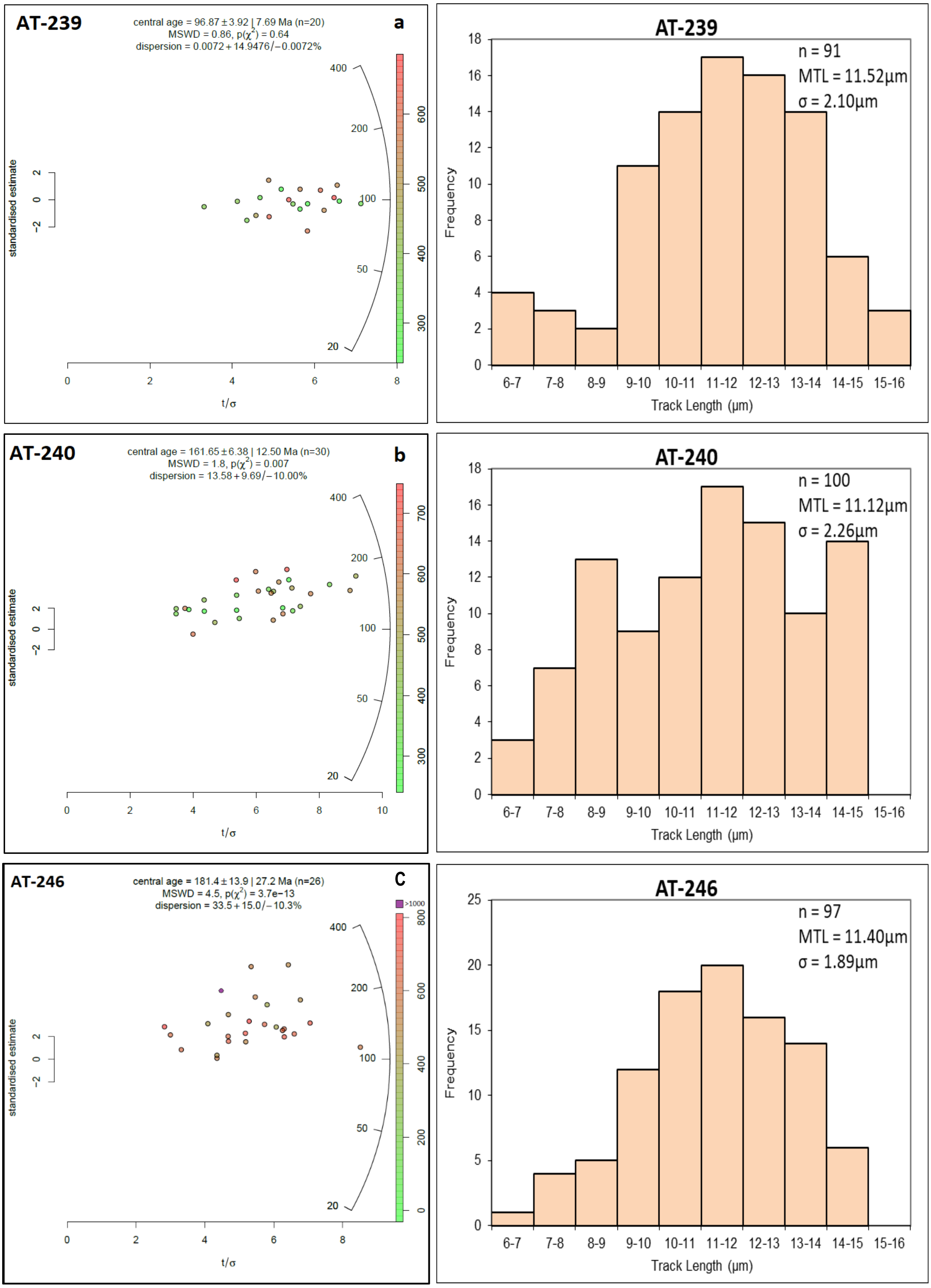
AT-239
central age = 96.87 ± 3.92 | 7.69 Ma (n=20)
MSWD = 0.86, p(χ²) = 0.64
dispersion = 0.0072 + 14.9476/− 0.0072%
a
standardised estimate
t/σ
AT-239
n = 91
MTL = 11.52μm
σ = 2.10μm
Frequency
Track Length (μm)
AT-240
central age = 161.65 ± 6.38 | 12.50 Ma (n=30)
MSWD = 1.8, p(χ²) = 0.007
dispersion = 13.58 + 9.69/− 10.00%
b
standardised estimate
t/σ
AT-240
n = 100
MTL = 11.12μm
σ = 2.26μm
Frequency
Track Length (μm)
AT-246
central age = 181.4 ± 13.9 | 27.2 Ma (n=26)
MSWD = 4.5, p(χ²) = 3.7e−13
dispersion = 33.5 + 15.0/− 10.3%
C
>1000
standardised estimate
t/σ
AT-246
n = 97
MTL = 11.40μm
σ = 1.89μm
Frequency
Track Length (μm)
6-7
7-8
8-9
9-10
10-11
11-12
12-13
13-14
14-15
15-16

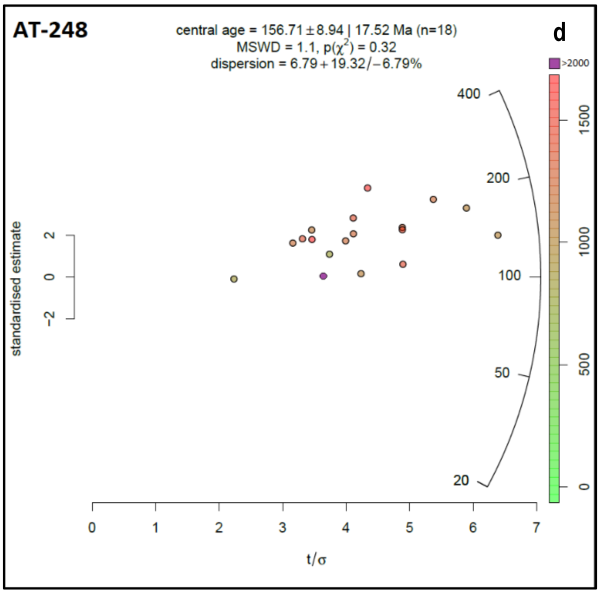
AT-248
central age = 156.71 ± 8.94 | 17.52 Ma (n=18)
MSWD = 1.1, p(χ2) = 0.32
dispersion = 6.79 + 19.32/−6.79%
d
>2000
standardised estimate
t/σ
400
200
100
50
20
1500
1000
500
0

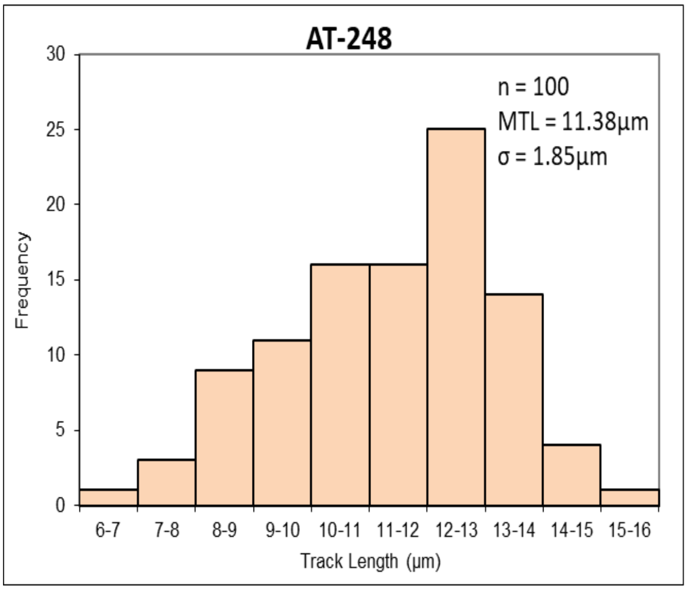
AT-248
n = 100
MTL = 11.38µm
σ = 1.85µm
Frequency
Track Length (µm)
6-7
7-8
8-9
9-10
10-11
11-12
12-13
13-14
14-15
15-16

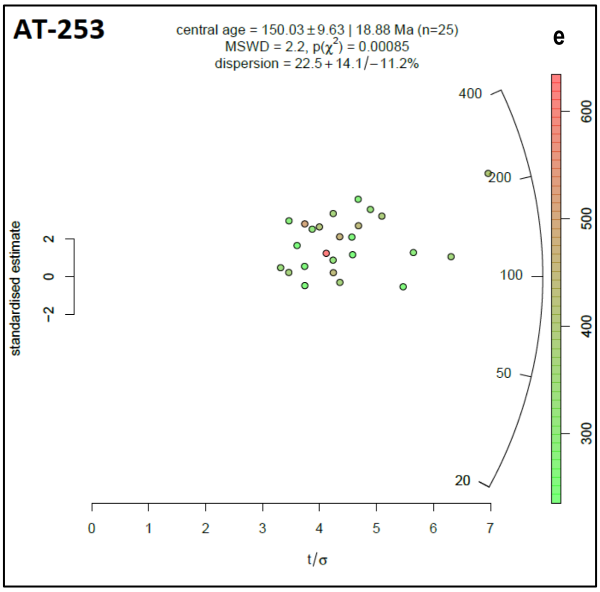
AT-253
central age = 150.03 ± 9.63 | 18.88 Ma (n=25)
MSWD = 2.2, p(χ2) = 0.00085
dispersion = 22.5 + 14.1/−11.2%
e
standardised estimate
t/σ
400
200
100
50
20
600
500
400
300

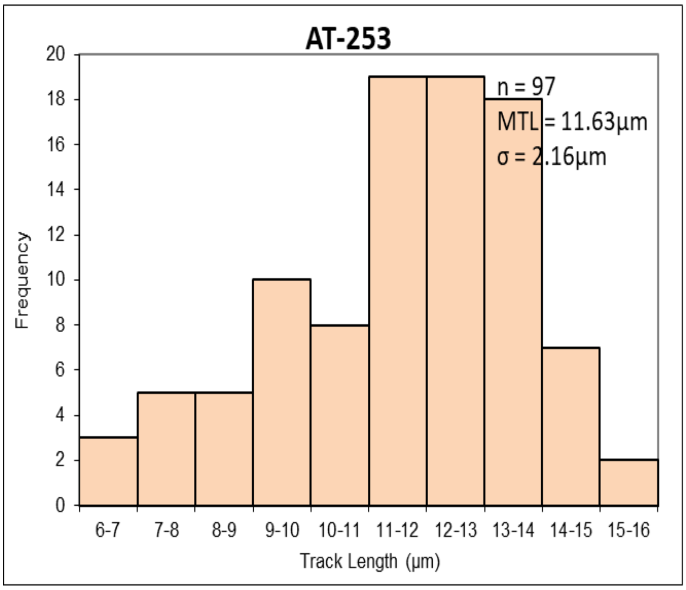
AT-253
n = 97
MTL = 11.63µm
σ = 2.16µm
Frequency
Track Length (µm)
6-7
7-8
8-9
9-10
10-11
11-12
12-13
13-14
14-15
15-16

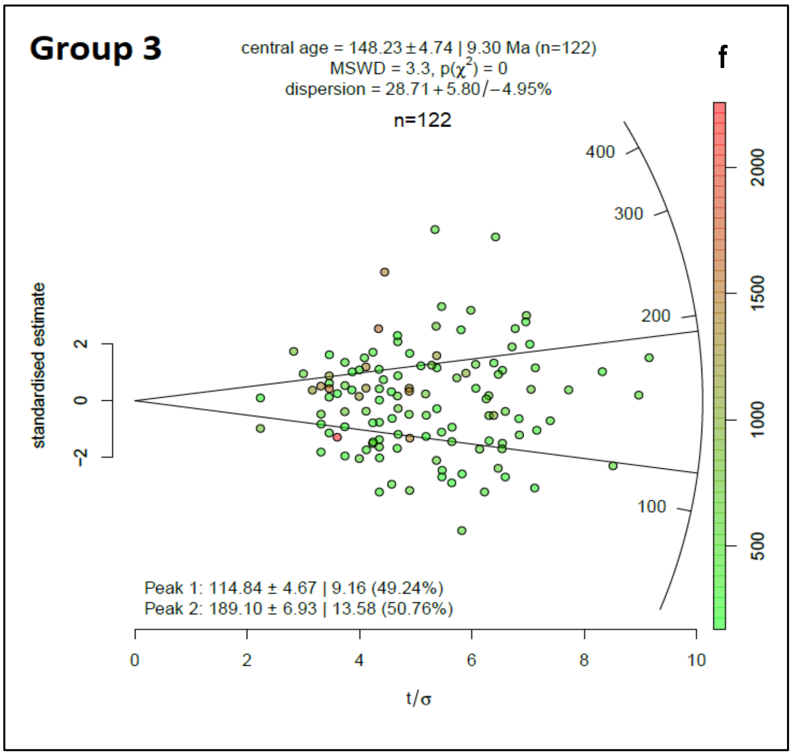

Figure 7 – Radial plots of calculated AFT ages for samples associated with Group 3 (a-e) and a pooled sample radial plot (f) with all analysed grains in Group 3 (caption as in Figure 5).

4.2.4 GROUP 4

Samples AT-242 and AT-244 yield central AFT ages of 223 ± 14 Ma and 179 ± 8 Ma respectively. Sample AT-242 passed the χ^2 test and yielded a single age population dispersion of <25% suggesting this sample records a single-grain age population. Sample AT-244, however, failed the χ^2, suggesting a potential for two age populations. Sufficient number of confined tracks (>75) were measured in both samples, producing mean track lengths of 11.46 ± 2.28 µm and 11.94 ± 2.28 µm respectfully (Table 3, Figure 8). The pooled radial plot for Group 4 yields a central AFT age of 194 ± 8 Ma and yields two statistically defined age peaks, with Peak 1 AFT age of 174 ± 7 Ma and Peak 2 AFT age of 262 ± 25 Ma (Figure 8). No observable Cl trends are seen within the samples of Group 3, suggesting samples have not undergone differential annealing of fission tracks.

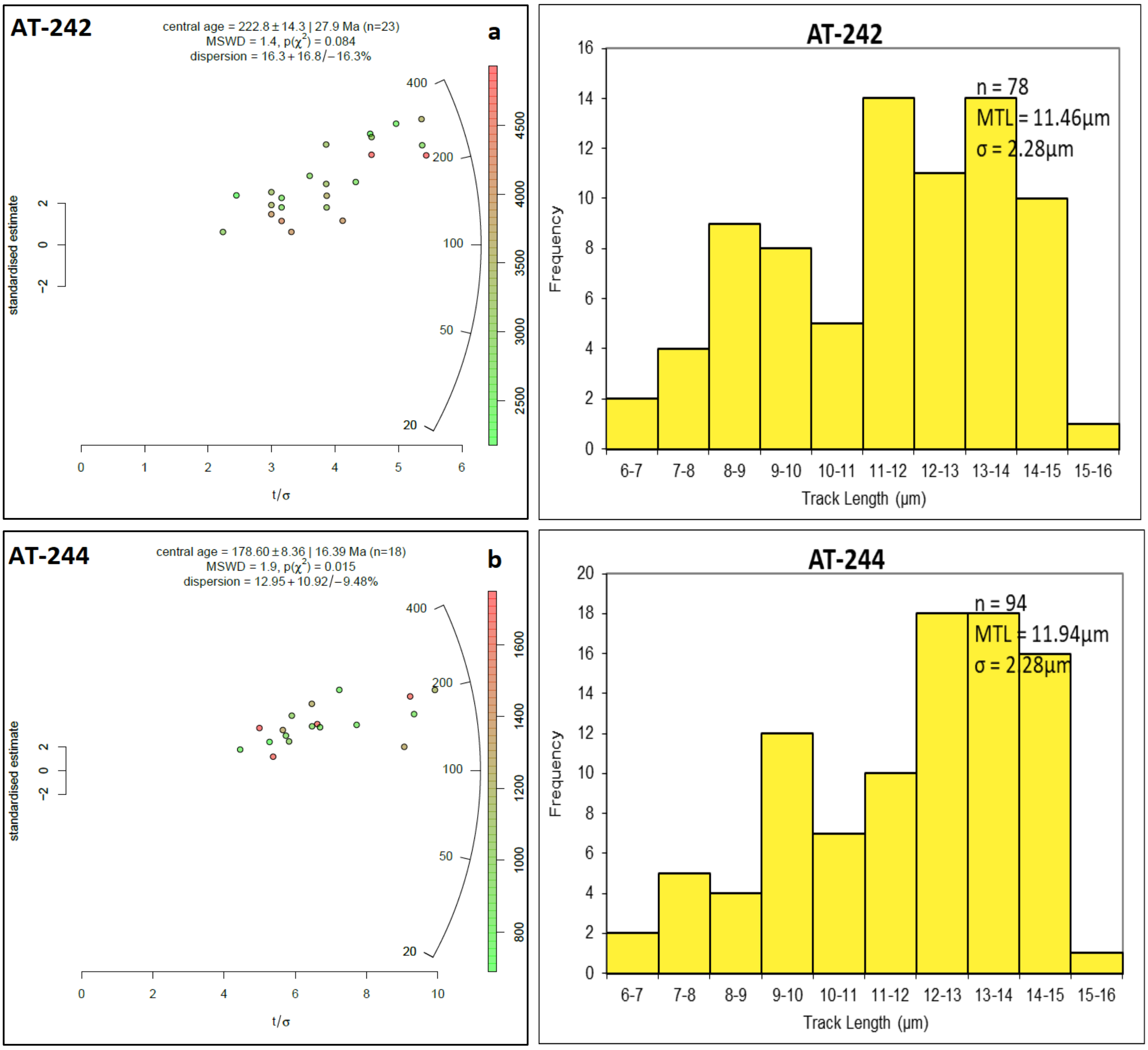
AT-242
central age = 222.8 ± 14.3 | 27.9 Ma (n=23)
MSWD = 1.4, p(χ2) = 0.084
dispersion = 16.3 + 16.8/− 16.3%
a
standardised estimate
t/σ
AT-242
n = 78
MTL = 11.46µm
σ = 2.28µm
Frequency
Track Length (µm)
AT-244
central age = 178.60 ± 8.36 | 16.39 Ma (n=18)
MSWD = 1.9, p(χ2) = 0.015
dispersion = 12.95 + 10.92/−9.48%
b
standardised estimate
t/σ
AT-244
n = 94
MTL = 11.94µm
σ = 2.28µm
Frequency
Track Length (µm)

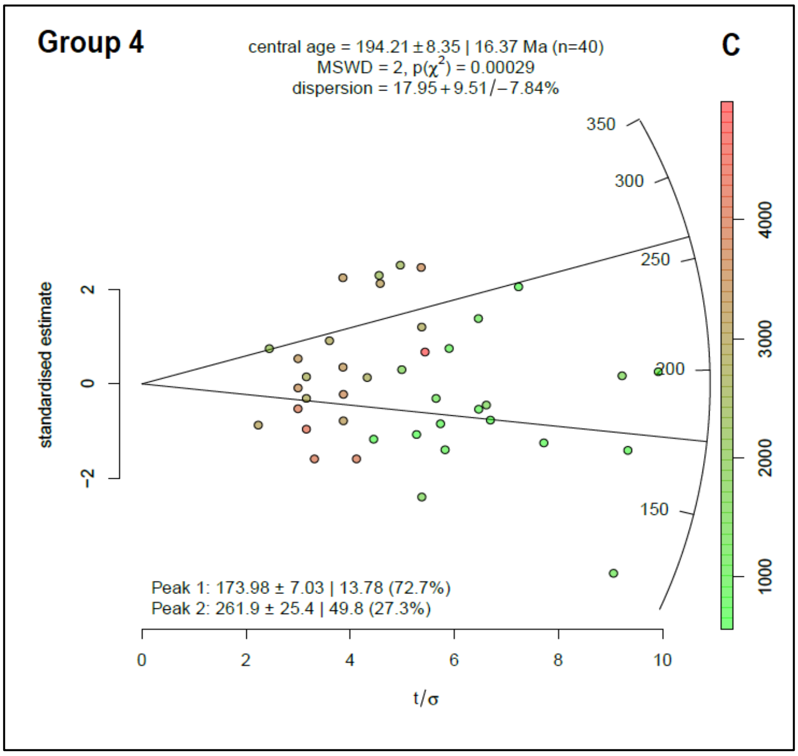

Figure 8 – Radial plots of calculated AFT ages for samples associated with Group 4 (a-b) and a pooled sample radial plot (c) with all analysed grains in Group 4 (caption as in Figure 5).

4.2.4 POOLED STUDY AREA

The pooled radial plot for all samples yields a central AFT age of 141 ± 3 Ma and yields 3 statistically defined age peaks with a Peak 1 AFT age of 84 ± 2 Ma, a Peak 2 AFT age of 141 ± 4 Ma and a Peak 3 AFT age of 226 ± 8 Ma (Figure 9).

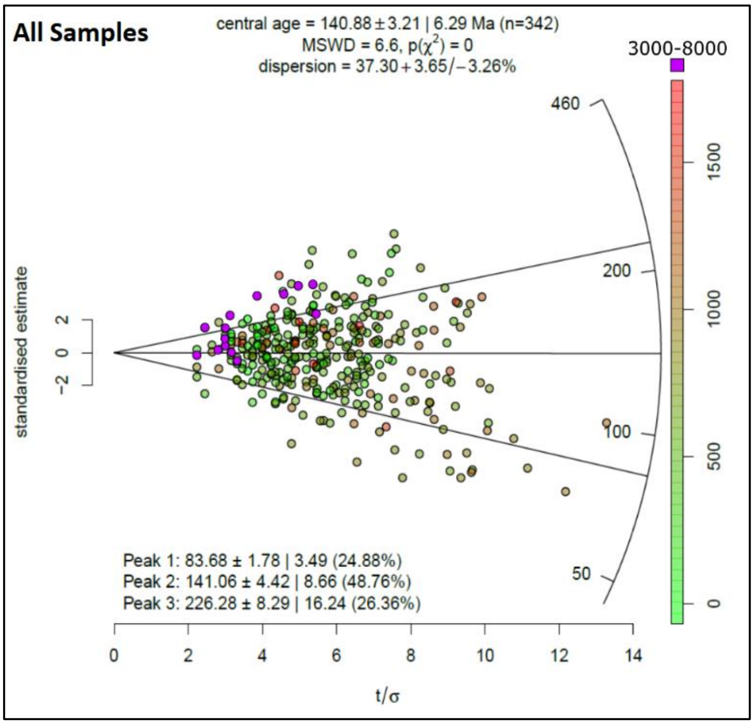

Figure 9 – Calculated AFT ages of all samples in a single pooled radial plot (caption as in Figure 5).

4.3 Apatite U-Pb results

Sixteen samples yield meaningful AU-Pb dates, ranging from Early Ediacrian (585 ± 17 Ma) to the Middle Permian (255 ± 21 Ma) with sample AT-207 yielding a Late Mesoproterozoic age (1021 ± 26 Ma). AU-Pb ages are detailed in Table 4. Alongside Central AFT ages. Grains suffering from analytical problems (such as strong zonation) were treated as outliers and removed from consideration for age calculations.

Table 4 – Summarised AU-Pb table with AFT age for comparison. n represents the number of grains in each sample used in AU-Pb analysis, MSWD represents the mean square weighted deviation of AU-Pb data. The AU-Pb age is obtained from the Terra-Wasserburg Concordia plot by taking the value of the lower intercept with a 2σ uncertainty. The AFT age represents the central AFT age, obtained from RadialPlotter (Vermeesch, 2009) with a 1σ uncertainty.

Sample	Lithology	n	MSWD	AU-Pb Age (Ma)	2σ (Ma)	AFT Age (Ma)	1σ (Ma)
AT-202	Granitoid	29	2	482	14	179	10
AT-203	Gneiss	24	37	585	17	218	16
AT-205	Leucocrate Granite	19	1.2	448	17	144	10
AT-206	Pink Granite	8	1.2	436	29	109	8
AT-207	Gneiss	36	33	1021	26	111	5
AT-238	Deformed Granite	29	2	482	14	126	14
AT-239	Granite	24	1.5	433	25	97	4
AT-240	Red Granite	29	0.41	422	21	162	6
AT-242	Diorite	24	0.94	255	14	223	14
AT-244	Gneiss	21	1.4	320	17	179	8
AT-246	Biotite Granite	32	1.3	411	11	181	14
AT-248	Gneiss	29	1.5	458	11	157	9
AT-252	Pink Granite	40	0.94	445	6	88	6
AT-253	Granodiorite	31	0.83	402	33	150	10
AT-254	Granite	40	1	428	9	95	4
AT-255	Granite	8	1.6	513	21	103	20

4.3.1 ACCURACY OF DATA

Durango and McClure apatite were used to check the accuracy of the U-Pb age of unknown samples. Durango apatite yielded a ^{207}Pb corrected weighted average ^{206}Pb/^{238}U age of 32.6 ± 0.61 Ma and McClure apatite yielded an age of 529.16 ± 3.15 Ma (Figure 9). The values obtained are similar to the published $_{40}$Ar/$_{39}$Ar age for Durango apatite at 31.44 ± 0.18 Ma (McDowell et al. 2005) and the published AU–Pb age of McClure apatite at 524.6 ± 3.2 Ma (Chew et al. 2014). Due to the similarity in ages, the AU-Pb data for the analysed samples can be treated as being reliable.

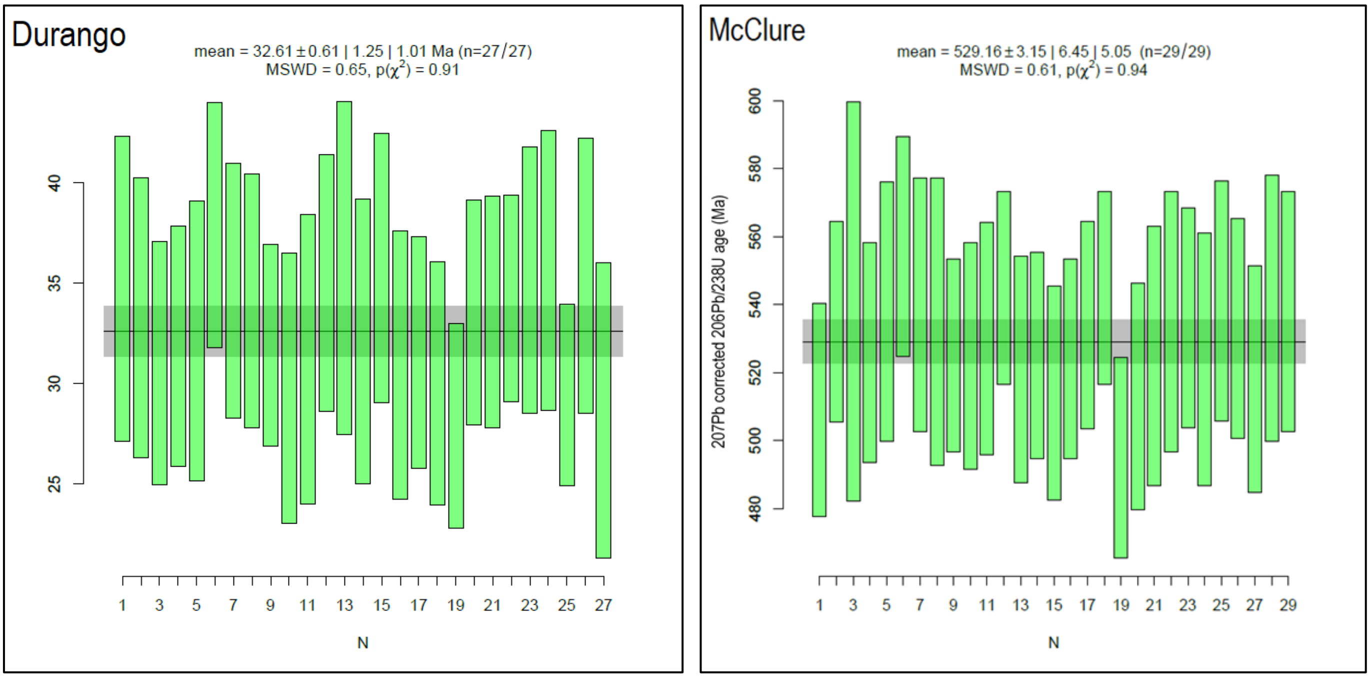

Figure 10 - ^{207}Pb corrected weighted average ^{206}Pb/^{238}U ages for analysed secondary standards: Durango apatite and McClure apatite.

4.3.2 TERA-WASSERBURG CONCORDIA PLOTS

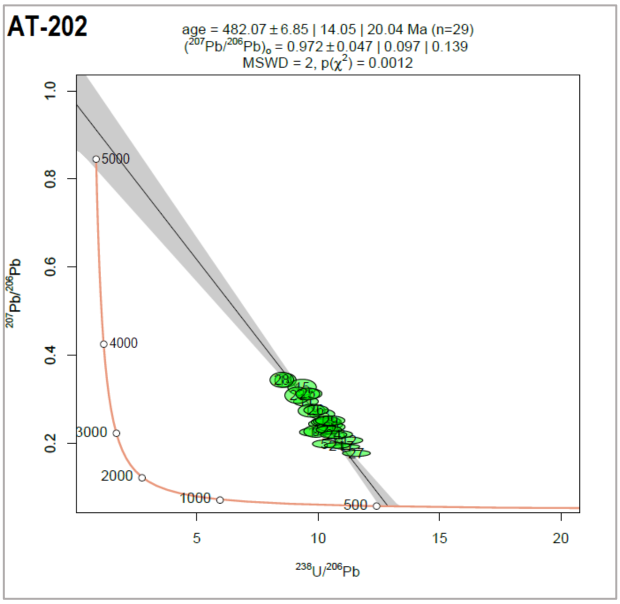

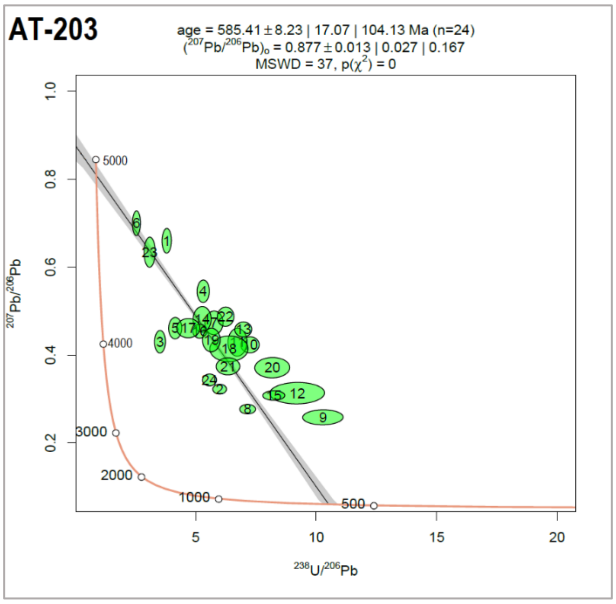

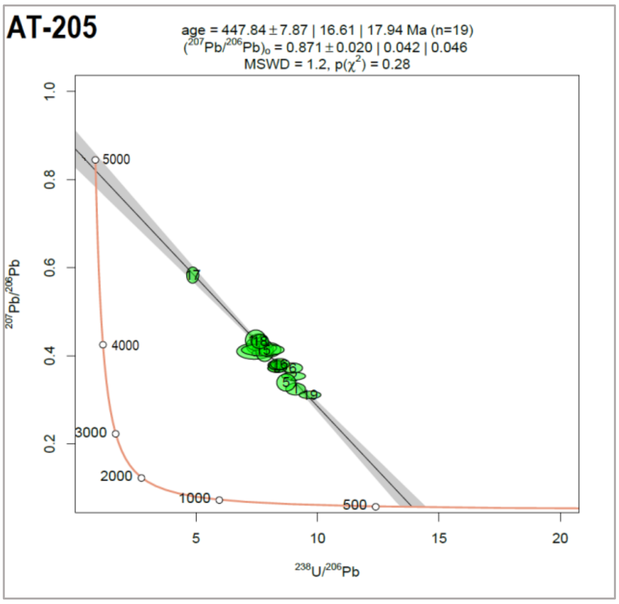

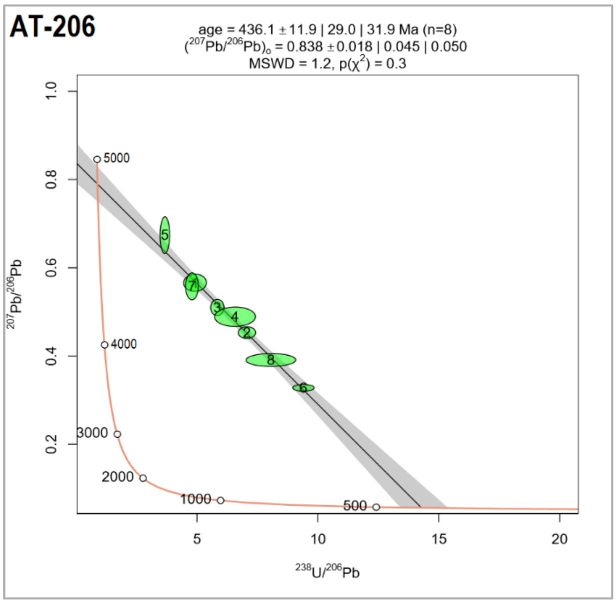

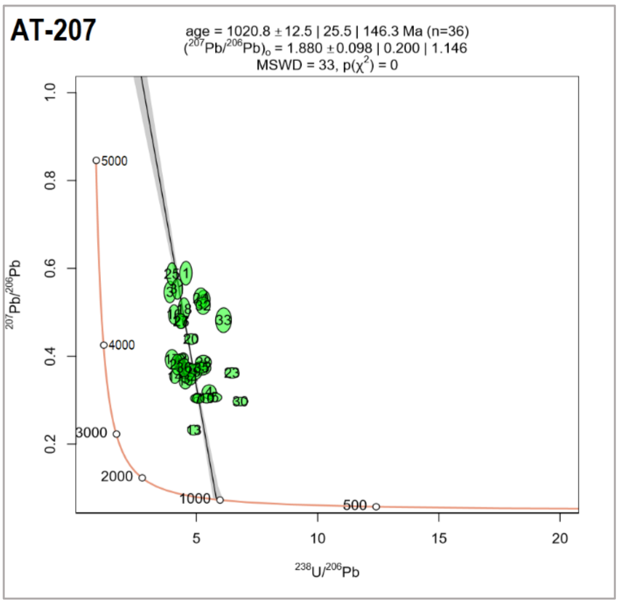

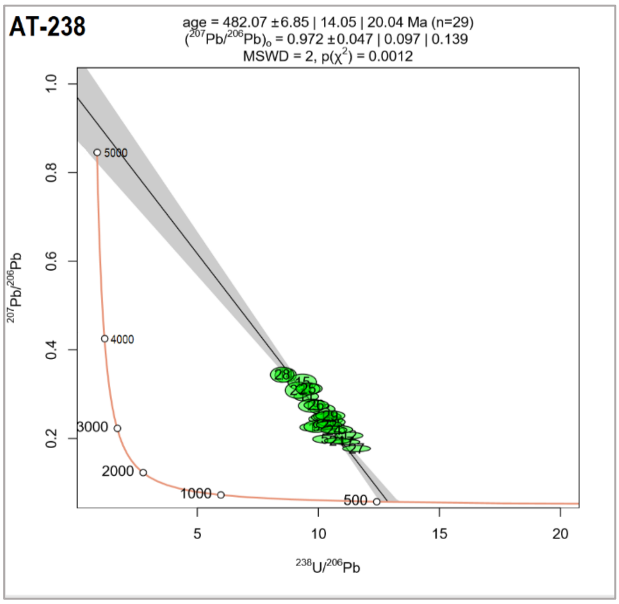

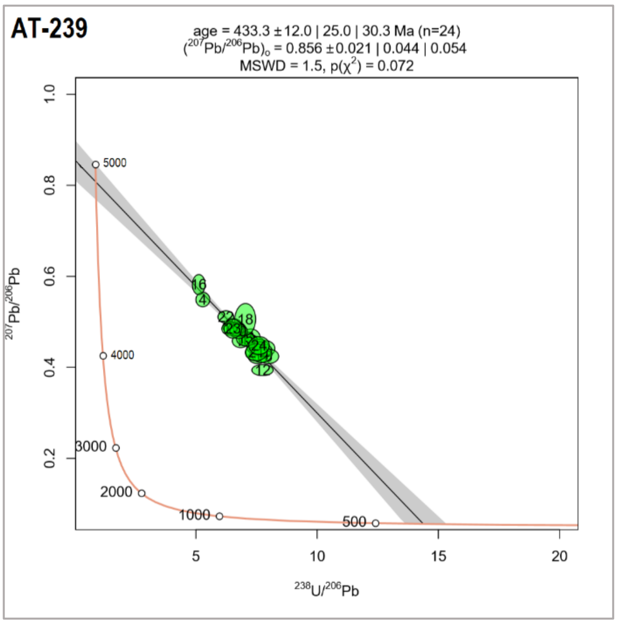
AT-239
age = 433.3 ±12.0 | 25.0 | 30.3 Ma (n=24)
(207Pb/206Pb)o = 0.856 ±0.021 | 0.044 | 0.054
MSWD = 1.5, p(χ2) = 0.072
207Pb/206Pb
238U/206Pb

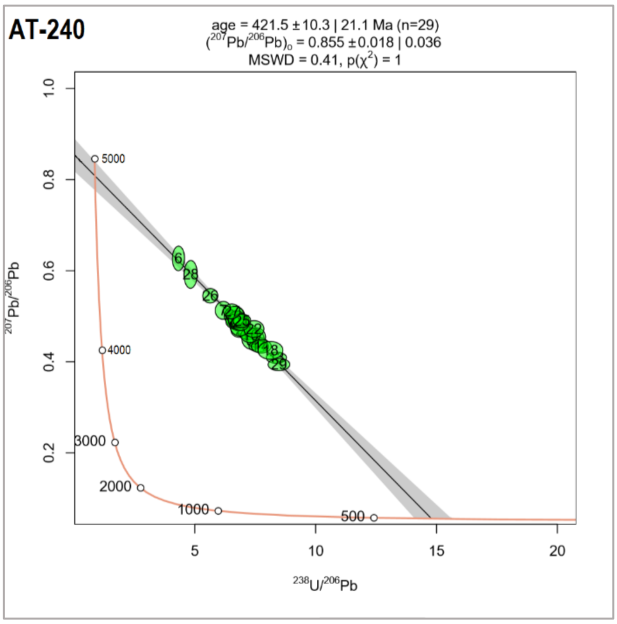
AT-240
age = 421.5 ±10.3 | 21.1 Ma (n=29)
(207Pb/206Pb)o = 0.855 ±0.018 | 0.036
MSWD = 0.41, p(χ2) = 1
207Pb/206Pb
238U/206Pb

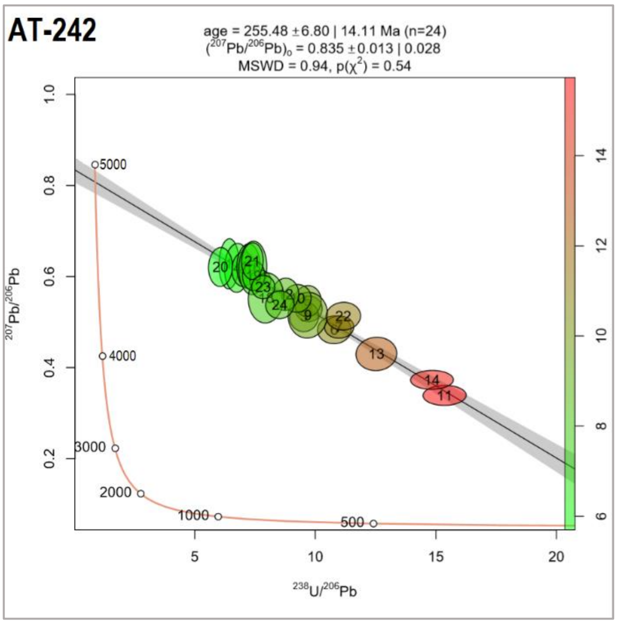
AT-242
age = 255.48 ±6.80 | 14.11 Ma (n=24)
(207Pb/206Pb)o = 0.835 ±0.013 | 0.028
MSWD = 0.94, p(χ2) = 0.54
207Pb/206Pb
238U/206Pb

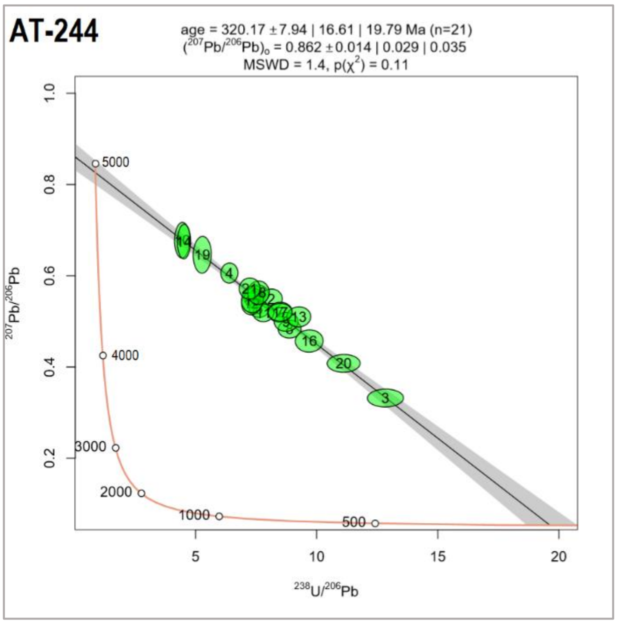
AT-244
age = 320.17 ±7.94 | 16.61 | 19.79 Ma (n=21)
(207Pb/206Pb)o = 0.862 ±0.014 | 0.029 | 0.035
MSWD = 1.4, p(χ2) = 0.11
207Pb/206Pb
238U/206Pb

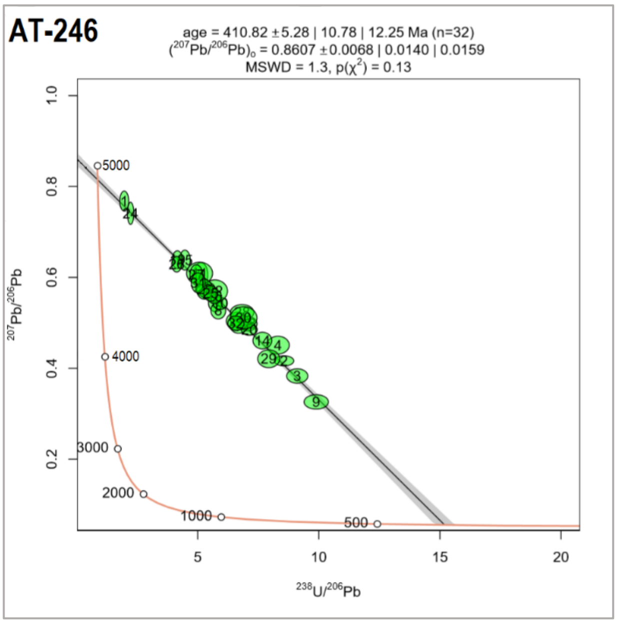
AT-246
age = 410.82 ±5.28 | 10.78 | 12.25 Ma (n=32)
(207Pb/206Pb)o = 0.8607 ±0.0068 | 0.0140 | 0.0159
MSWD = 1.3, p(χ2) = 0.13
207Pb/206Pb
238U/206Pb

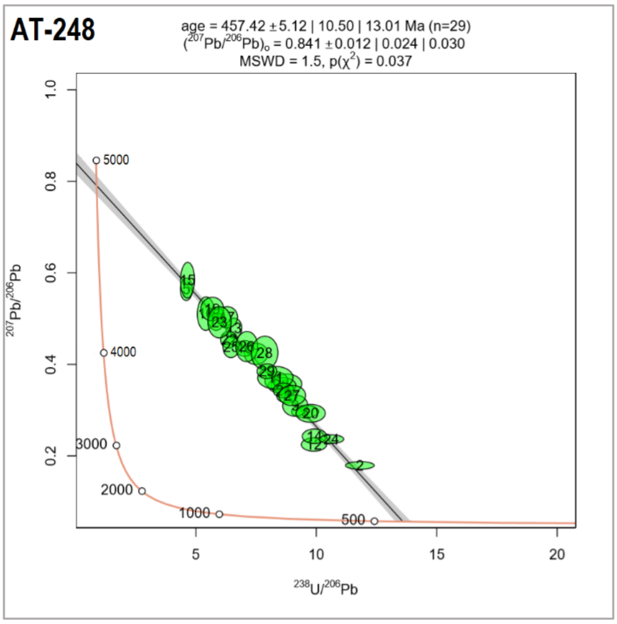
AT-248
age = 457.42 ±5.12 | 10.50 | 13.01 Ma (n=29)
(207Pb/206Pb)o = 0.841 ±0.012 | 0.024 | 0.030
MSWD = 1.5, p(χ2) = 0.037
207Pb/206Pb
238U/206Pb

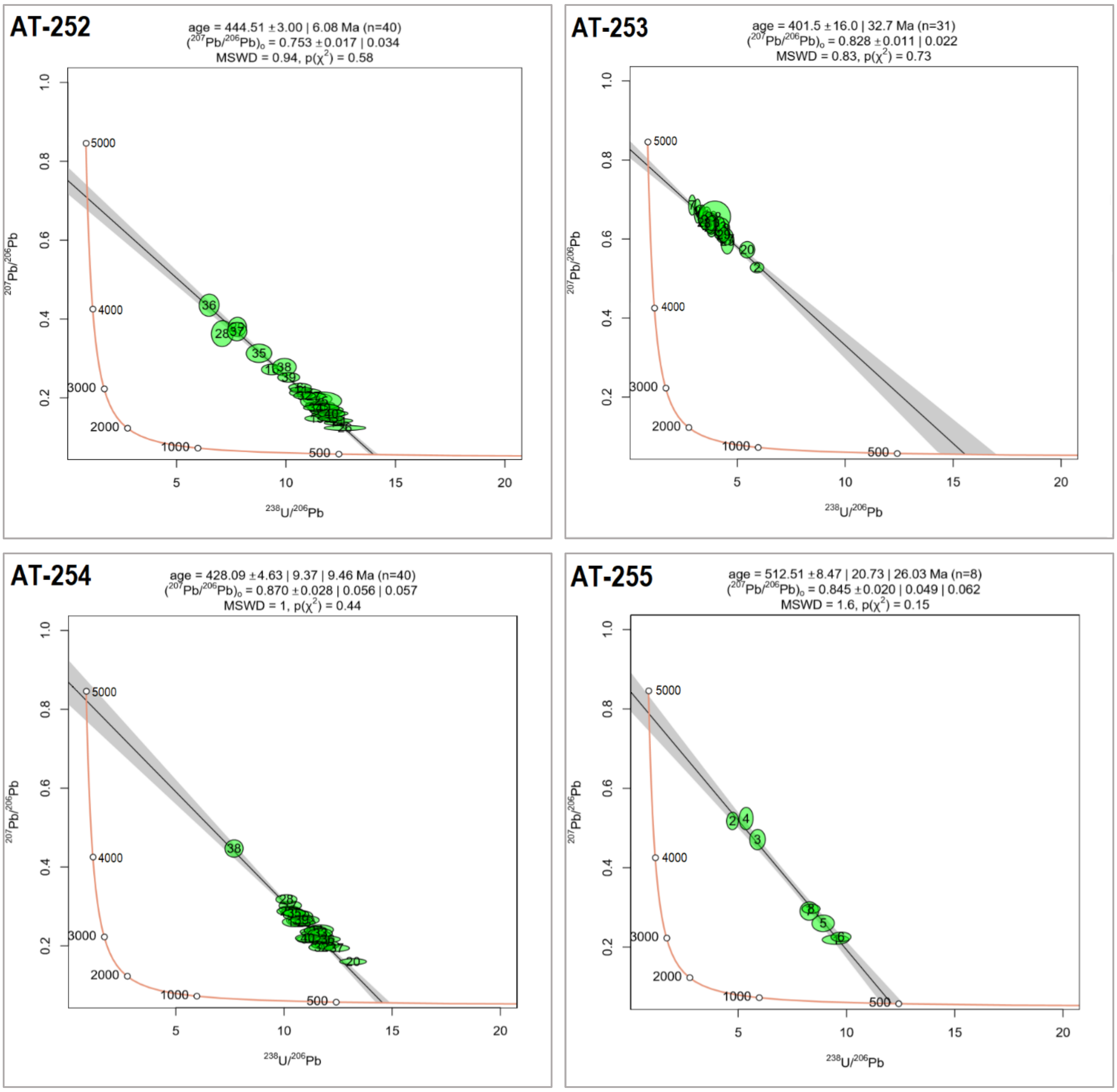

Figure 11 – The Tera-Wasserburg Concordia plots for every sample in the Qilian Shan. Green ellipses indicate grains used to produce the common-Pb line.

4.4 Thermal History Modelling

4.4.1 GROUP 1

Thermal history models for group 1 (Figure 12) record cooling through the APAZ since ~230-220 Ma with AT-203 recording prolonged cooling well before ~300 Ma. A three stage cooling history is observed for samples AT-202, AT-205 and AT-206. Rapid cooling is observed from ~230-210 Ma cooling to ~100-90ºC. Between ~210-25 Ma thermal quiescence before rapid cooling from ~100ºC starting at ~25 Ma to present day. Samples AT-207 and AT-238 enter the APAZ between ~160-140 Ma. AT-207 displays monotonic cooling through the APAZ and AT-238 displays thermal quiescence between ~130-25 Ma, before cooling from ~100ºC starting at ~25 Ma to present day.

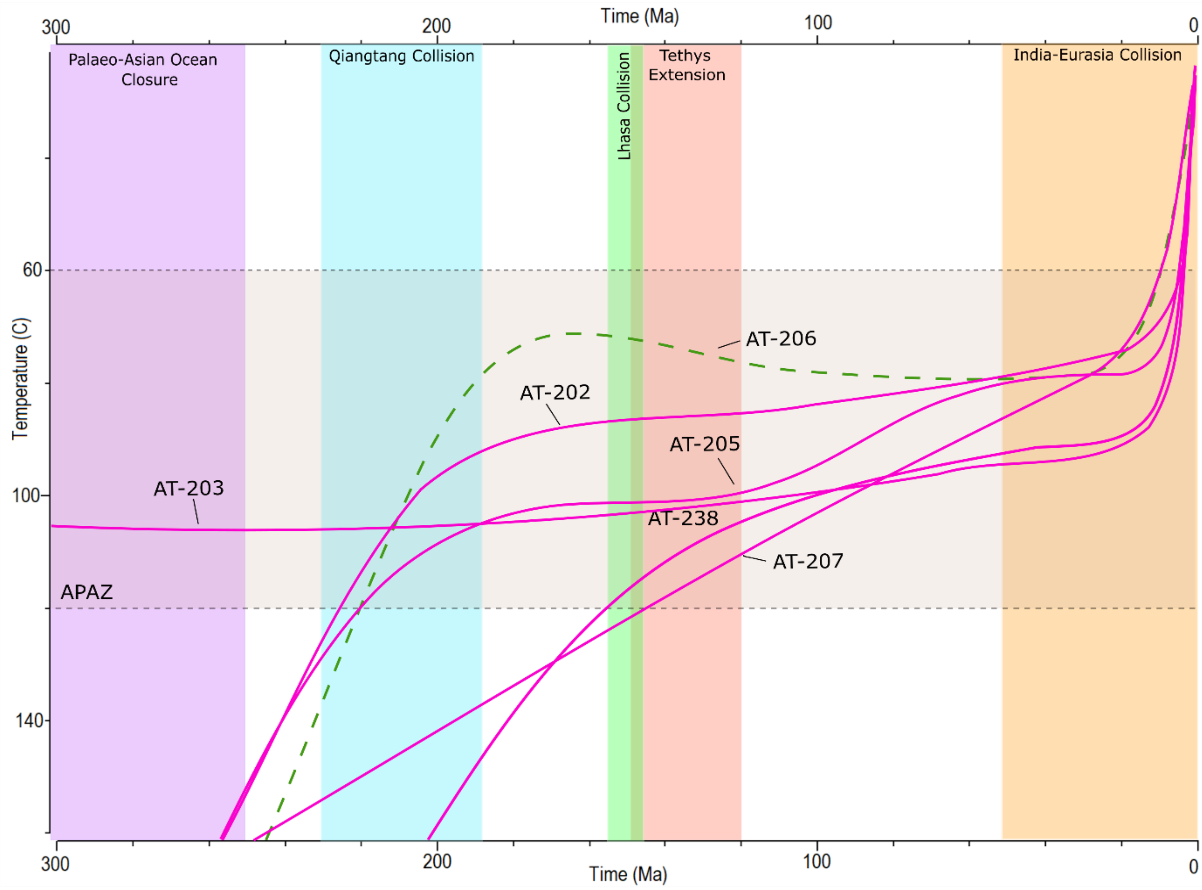

Figure 12 – Combined thermal history model for the samples associated with Group 1. The beige zone represents the apatite partial annealing zone (APAZ) between ~60-120°C (Wagner et al. 1989). Coloured columns represent the timing of regional tectonic events, purple = Palaeo-Asian Ocean Closure, blue zone = Qiangtang Collision, green zone = Lhasa Collision, red zone = Tethys Ocean Extension and orange zone = India-Eurasia Collision. The dashed green line is representative of samples which contained less than 100 confined fission tracks (AT-206 = 86 confined tracks).

4.4.2 GROUP 2

Thermal history models for group 2 (Figure 13) record a three stage cooling history. All samples enter the APAZ between ~135-100 Ma. Sample AT-255 records monotonic cooling through the APAZ. Samples AT-252 and AT-254 record rapid cooling until ~70 Ma where they reach temperatures of ~70ºC and ~100ºC respectively. A period of thermal quiescence is observed within these samples from ~70-15 Ma, before cooling from 15 Ma to present day.

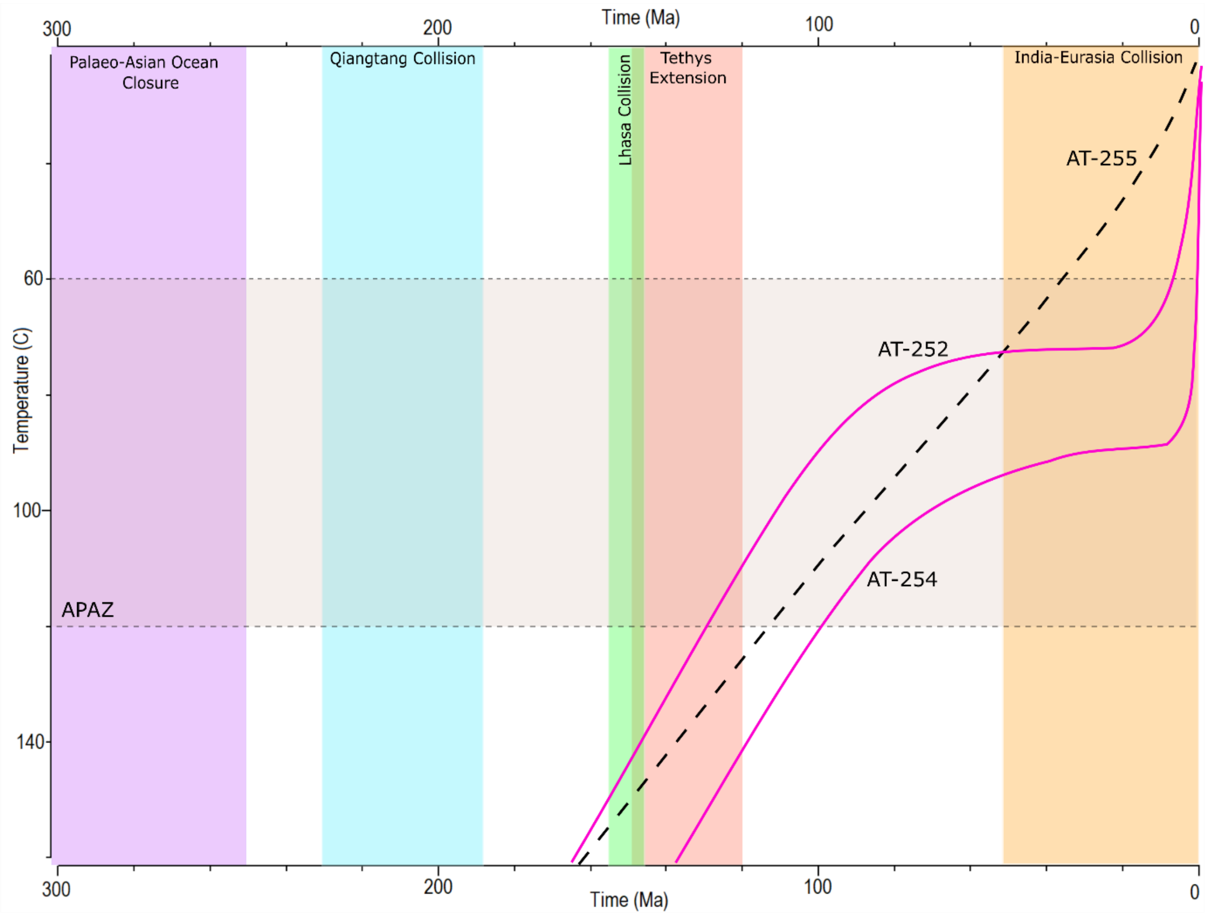

Figure 13 – Combined thermal history model for samples associated with Group 2 (Caption as in Figure 12). Dashed black line represents samples with a total confined fission track count <30.

4.4.3 GROUP 3

Thermal history models for Group 3 (Figure 14) record a three stage cooling history. Sample AT-240 enters the APAZ at ~230 Ma, samples AT-246, AT-248 and AT-253 enter between ~220-200 Ma and sample AT-239 enters at ~160 Ma. Sample AT-240 cools rapidly until it reaches ~60ºC at ~170 Ma, where it enters a phase of reheating until 100 Ma finishing at ~90ºC. It experiences a brief phase of thermal quiescence till ~70 Ma before slowly cooling and leaving the APAZ at ~25 Ma. Samples AT-246, AT-248 and AT-253 record rapid cooling until ~170 Ma finishing at ~100ºC. Following this, a period of thermal quiescence is recorded between ~170-20 Ma, before rapidly cooling from ~100ºC to present day temperatures between ~20 Ma- present day. Sample AT-239 cools rapidly until ~130 Ma at ~100ºC, it then follows the same trend of thermal quiescence between ~170-20 Ma before cooling rapidly from ~20 Ma.

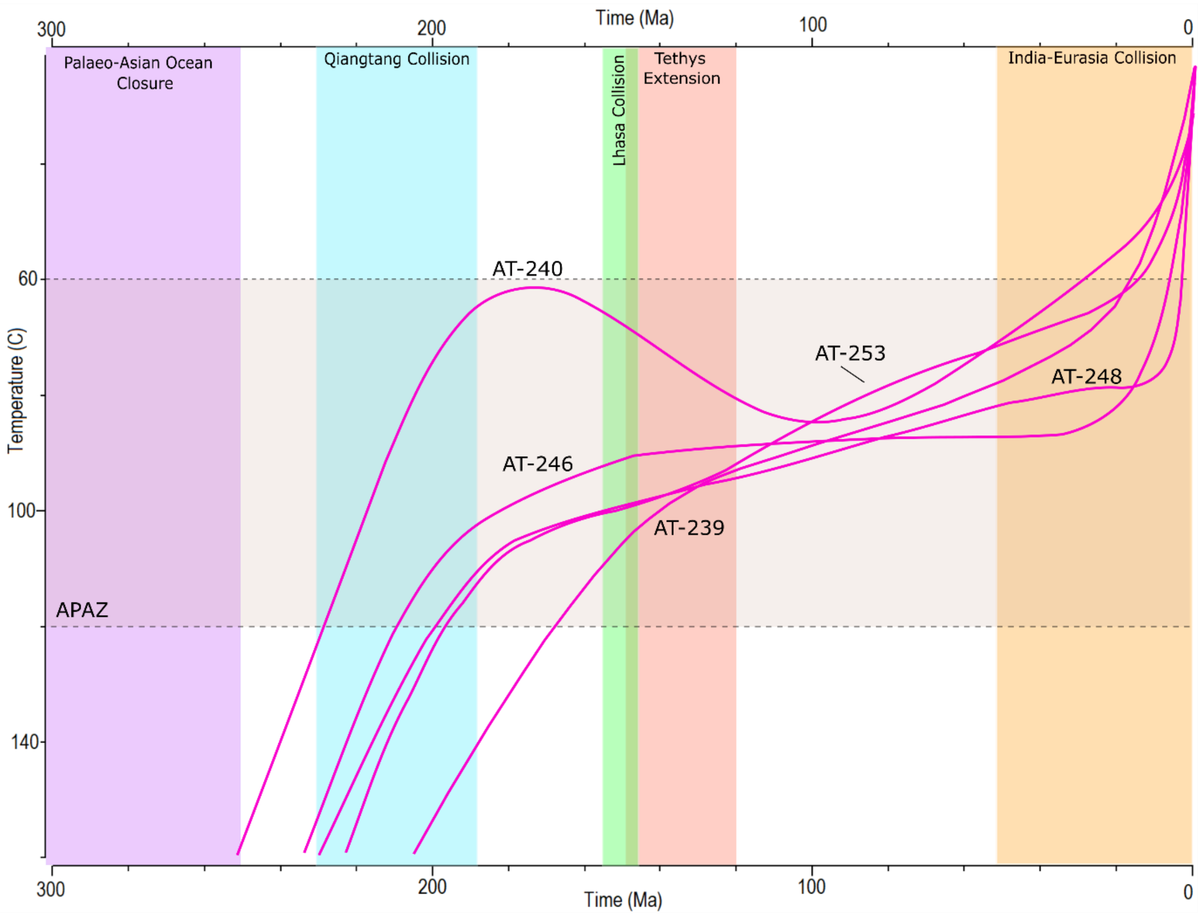

Figure 14 - Combined thermal history model for samples associated with Group 3 (Caption as in figure 12).

4.4.4 GROUP 4

Thermal history models for Group 4 (Figure 15) record a three stage cooling history. The samples enter the APAZ between ~240-230 Ma, where they rapidly cool and exit the APAZ at ~220 Ma. At ~200 Ma, the samples re-enter the APAZ and reheat until ~150 Ma, reaching temperatures of ~90ºC. Both samples then cool uniformly from ~150 Ma – present day, exiting the APAZ at ~60-50 Ma.

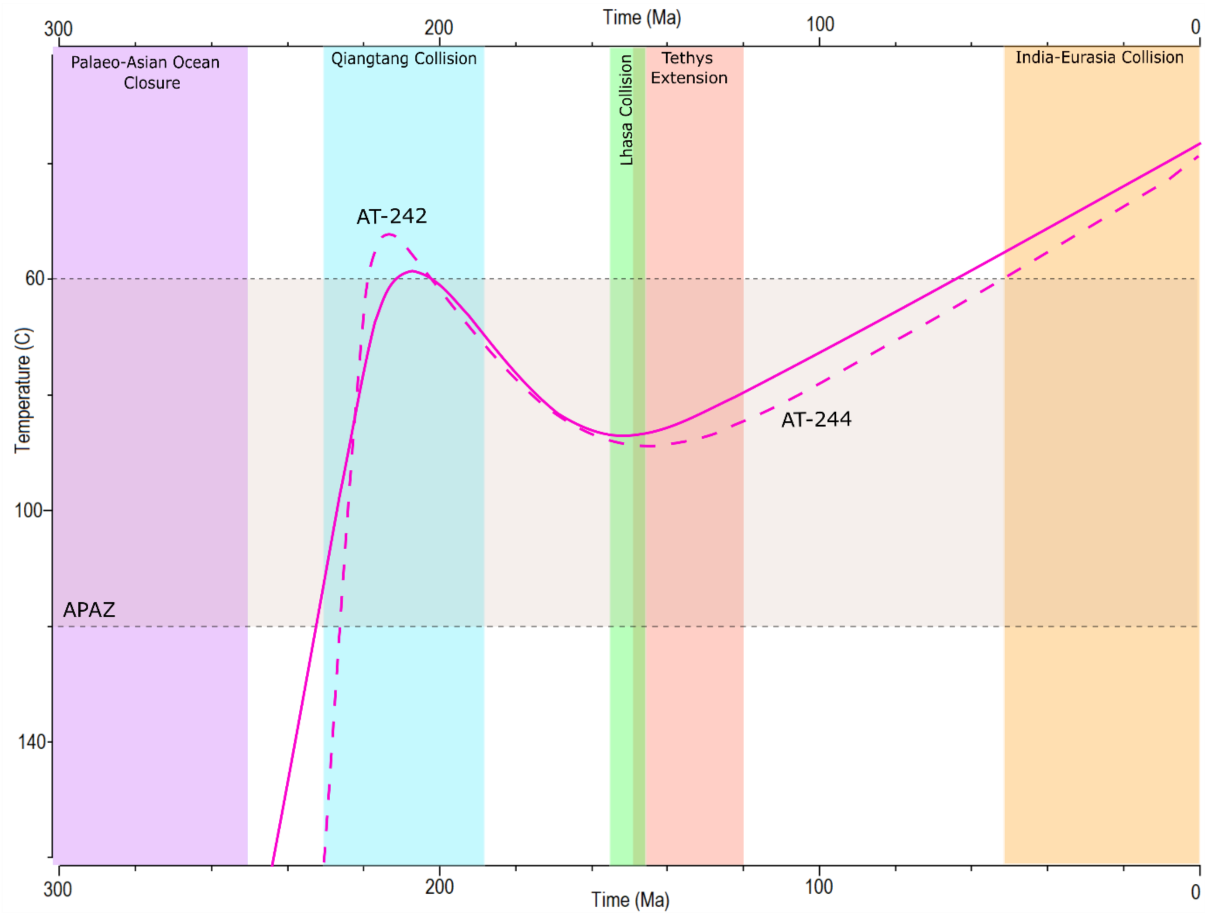

Figure 15 - Combined thermal history model for samples associated with Group 4 (Caption as in figure 12). The dashed line is used to distinguish AT-242 which had less than 100 confined tracks (78).

5. DISCUSSION

5.1 AFT age – Elevation Plot

The age-elevation plot displays the relationship between altitude (m) and AFT age (Ma) for each sample (Figure 16), which can be used to estimate relative cooling rates for different sub-terranes of this study (Fitzgerald et al. 1993). Data for groups 3 and 4 (orange and yellow), from the low-elevation part of the study, reveal a sub-horizontal age-elevation trend, likely representing an early Mesozoic fossil APAZ (Figure 17). This means that the samples record meaningless cooling ages in between two thermal events. Group 1 (green) displays a similar sub-horizontal age-elevation trend but at higher elevations, suggesting that the samples from the elevated plateau preserve the same, but now uplifted fossil APAZ signature. Hence, Group 1 samples were uplifted but do not record significant denudation during the Meso-Cenozoic. If significant denudation (>1.5km) had occurred, the samples would record younger ages (Kuhlemann and Rahn 2013). The age-elevation data for Group 2 (blue) records a near-vertical trend, implying these samples cooled rapidly and record evidence of a thermo-tectonic event at ~100 Ma. Sample AT-239 (Group 3) is an outlier as it was sampled directly in a thrust fault and exhumed rapidly, suggesting the faults in the region played an important role in the ~100 Ma thermal event.

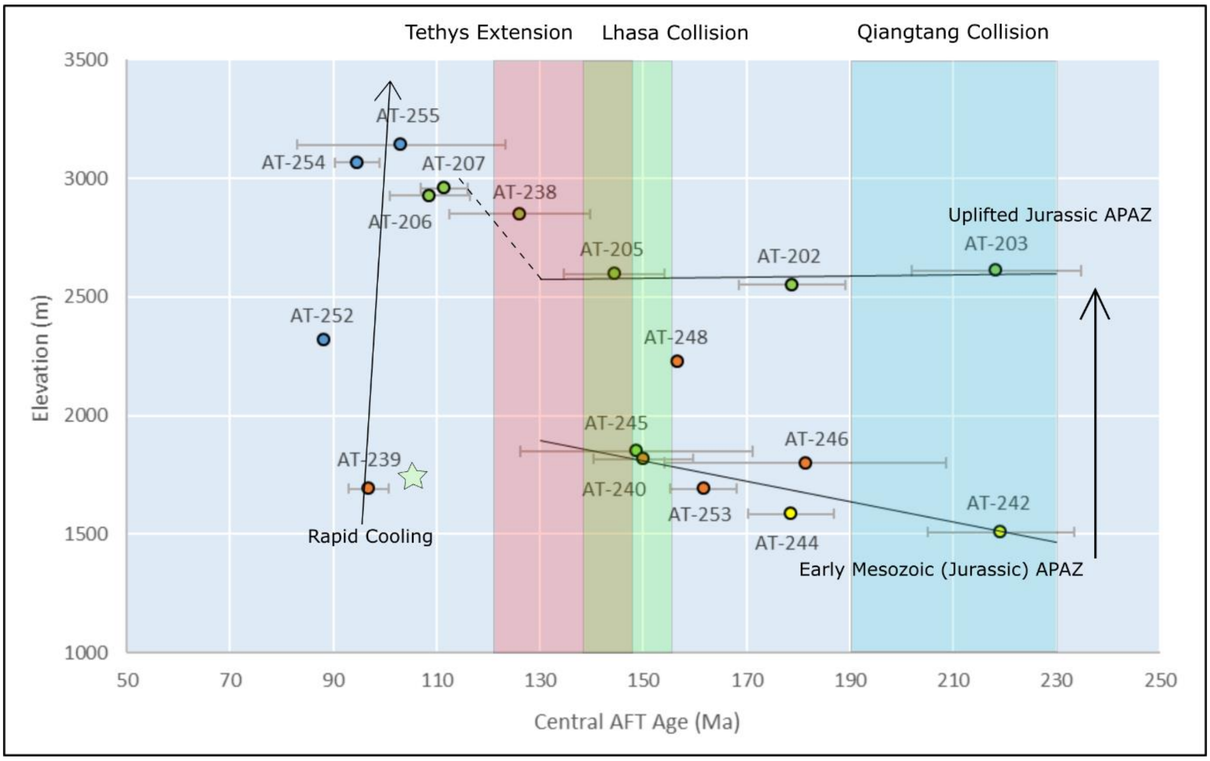

Figure 16 – Elevation plot based on the relationship between Elevation and AFT age. Error bars on the x-axis represent the uncertainty of the AFT age in Ma. Coloured columns represent the timing of regional tectonic events, blue zone = Qiangtang Collision, green zone = Lhasa Collision and the red zone = Tethys Ocean Extension. Sample groups are represented by different colour points, Green = Group 1, Blue = Group 2, Orange = Group 3 and Yellow = Group 4. The lower, horizontal trend-line shows an Early Mesozoic fossil APAZ signature, the higher horizontal trend-line shows an uplifted Jurassic APAZ signature. The right arrow symbolizes the uplift between the lower and upper trend-lines, while the left arrow shows a trend of fast cooling observed within samples of Group 2 (Sample AT-239, signified with the star is part of this trend, however, its rapid uplift is due to faulting).

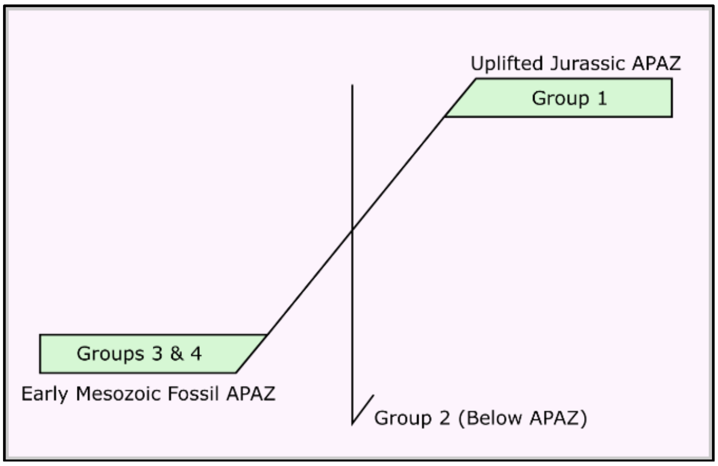

Figure 17 – APAZ location plot displaying where the sample groups are taken within the APAZ. Group 1 records an uplifted fossil APAZ signature, Group 2 records APAZ signatures from below the APAZ (younger AFT ages) and Groups 3 & 4 record early Mesozoic fossil APAZ signatures.

5.2 Mean Track Length – AFT age Boomerang Plot

The ‘boomerang’ plot displays the relationships between Mean Track Length (MTL) and AFT age for each sample (Green et al. 1986), which can be used to identify the timing of thermal events from apparent AFT data. In the boomerang plot for this study (Figure 18), the ‘blades’ of the ‘boomerang trend’ represent incomplete limbs and thus don’t record the timing of discrete thermal events. The limbs, however, still record evidence of faster cooling relative to the central part of the boomerang trend, represented by longer MTLs. The central part of the boomerang trend reveals the timing of slow cooling and/or tectonic quiescence, represented by short MTLs which reflect a prolonged residence in the APAZ. In more detail, the samples of this study constrain two boomerang trends. The main trend (pink zone, Figure 18), records initial faster cooling in the early Jurassic (before ~180 Ma). When the limb is projected back in time, following the same trajectory, MTL values above 12.5 μm would be found at ~210 Ma, coinciding with the timing of the Qiangtang Collision. Thus it is likely that the data contained in this area of the boomerang plot reflects cooling in response to the aftermath of the Qiantang Collision. This event is followed by a decrease in cooling rate and a prolonged residence in the APAZ, indicated by increasingly shorter MTLs during the late Jurassic-early Cretaceous. In the mid-Cretaceous, ~120-90 Ma the cooling rate increases (evidenced by longer MTLs) providing a record for a second cooling event in the region, however, MTL values don’t exceed ~12.5-13 μm, suggesting the thermal event that induced more rapid cooling is likely younger than 80 Ma. Samples AT-248 and AT-253 from Group 3 record a gentle increase in MTL values at ~160-140 Ma which potentially indicates that these samples record a second thermo-tectonic event in the region, evidenced by the second boomerang in Figure 18.

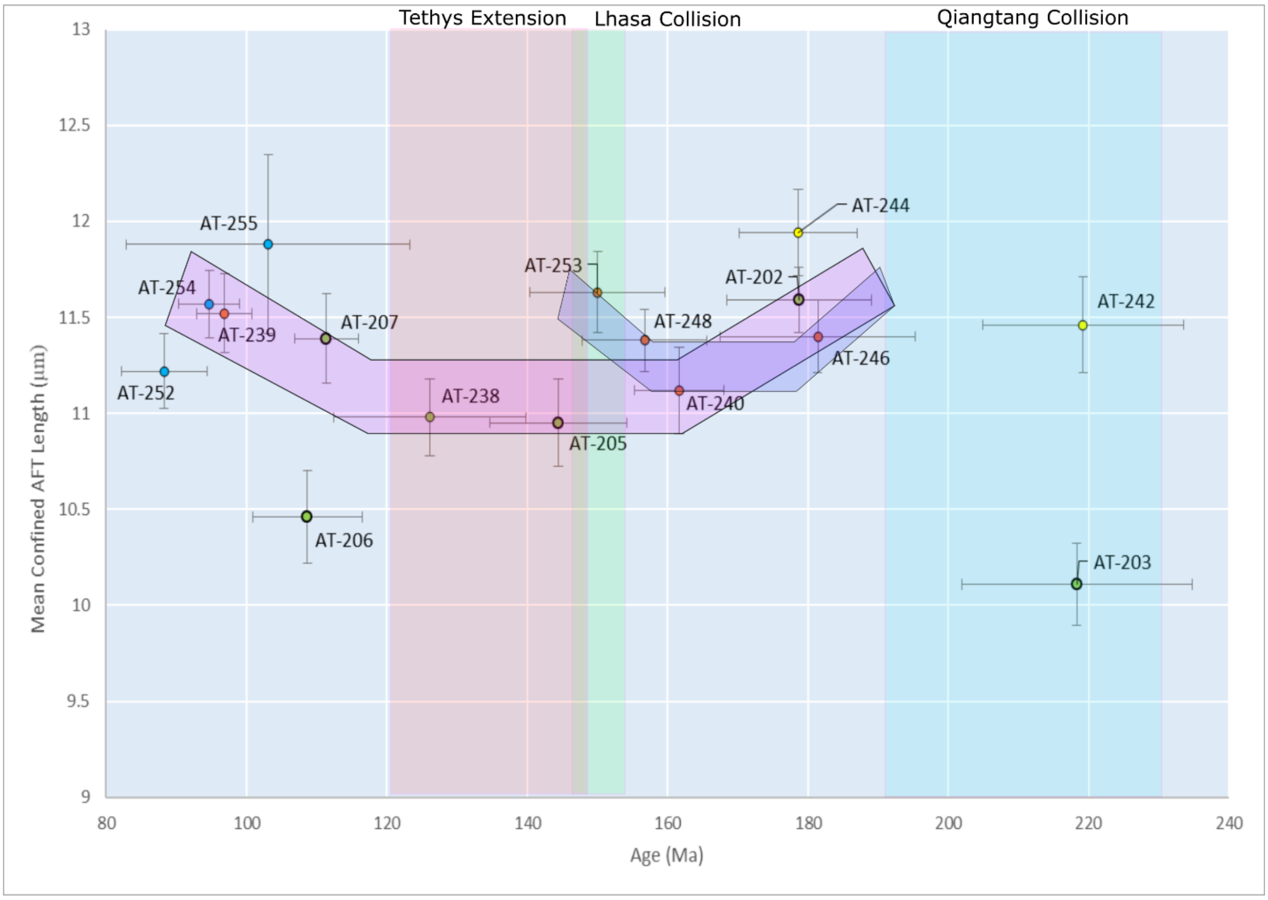

Figure 18 – 'Boomerang plot' based on the relationship between MTL and AFT age. Error bars represent the uncertainty of the MTL in µm on the y-axis and AFT age in Ma on the x-axis. Coloured columns represent the timing of regional tectonic events, blue zone = Qiangtang Collision, green zone = Lhasa Collision and the red zone = Tethys Ocean Extension. Sample groups are represented by different colour points, Green = Group 1, Blue = Group 2, Orange = Group 3 and Yellow = Group 4.

5.3 Geographical distribution of cooling events and cooling mechanisms

The thermal models across the Qilian Shan record a range of thermal histories, preserving periods of fast cooling during (1) the early Triassic-early Jurassic (~240-180 Ma), (2) mid Cretaceous (~130-75 Ma) and (3) the Oligocene-Miocene (~30-10 Ma) (Figures 12-15). Periods of fast cooling can be correlated to thermo-tectonic events that transpired at the distal Eurasian margins throughout the Mesozoic and Cenozoic, further discussed below.

Groups 1 and 3, which are featured on plateaus away from slopes share very similar thermal history models and primarily preserve cooling ages related to (i) the closure of the Palaeo-

Asian Ocean (PAO) or (ii) the Qiangtang Collision at the southern Eurasian margin. The Alxa Region, immediately north of the Qilian Shan is dominated by Jurassic conglomerate and coarse sandstone deposits coinciding with the timing of the closure of the PAO and the Qiangtang Collision (Song et al. 2018 and references therein). These coarse clastic deposits are the erosion products of exhumed bedrock, indicating the region underwent a phase of mountain building at that time. Hence, the rapid cooling pulse in the thermal history models for this study can be linked to rapid exhumation at that time.

In contrast, samples from Group 2, (taken from the highest elevations) record prominent mid-Cretaceous rapid cooling. The mid-Cretaceous rapid cooling phase can be linked to (i) extension in the Tethys Ocean or (ii) the collision and docking of the Lhasa Block with the Eurasian Continent. Within the adjacent Qaidam Basin (Figure 1), conglomerates of the early Cretaceous Quanyagou *Formation* were deposited coinciding with the timing of the Lhasa collision (Jian et al. 2013). These coarse, clastic deposits are also erosional products of exhumed bedrock, indicating the region underwent a second phase of mountain building at that time. Thus, the second pulse of rapid cooling in the thermal history models for this study can be linked to rapid exhumation at that time.

The samples in Group 4 (located in the Alxa domain, Figure 2), record rather complex thermal histories. The thermal history model for sample AT-240 (Group 3) closely matches the models from Group 4. These models, all at similar elevations, display a reheating event succeeding the closure of the Palaeo-Asian Ocean and the Qiangtang Collision. The reheating event is interpreted to be due to burial of the samples by the Jurassic conglomerates and coarse sandstone deposits mentioned above. Song et al. (2018) interpreted the Jurassic deposits are the result of denudation of Permian-Triassic palaeo-relief.

All models record an Oligocene-Miocene phase of rapid cooling for the Qilian Shan in some capacity. This can potentially be due to modelling artefacts forcing the model to present day temperatures, however, given the large temperature difference associated with this cooling phase (up to 100ºC cooling), this is rather unlikely. The Oligocene-Miocene cooling coincides with the 'hard phase' of the India-Eurasia Collision (Douwe et al. 2012). Every studied sample records this thermo-tectonic event, indicating the whole region underwent simultaneous cooling at that time. Sedimentary studies of the surrounding basins, the Qaidam, Juixi and Tarim reveal numerous Cenozoic conglomerate packages, during the Palaeocene, Eocene, Oligocene, Miocene, Pliocene, Pleistocene and the Quaternary (Zheng et al. 2017, Wang et al. 2016, Fang et al. 2007, Chang et al. 2014). The Cenozoic conglomerate packages found within these basins coincide with the timing of the India-Eurasia Collision and indicate regional cooling, mass exhumation and denudation of the Qilian Shan were occurring during this time.

5.4 Geographical AFT age disparities linked to fault reactivation

5.4.1 AT-246 and AT-252

Samples AT-246 (Group 3) and AT-252 (Group 2) on either side of an unnamed thrust fault (Figure 2) record vastly different cooling histories and AFT ages of 181±14 Ma and 88±6 Ma respectively (Figure 19). There is no notable difference in chlorine concentrations in the apatites between the two samples that could influence the annealing rate (Green et al. 1986), suggesting that the mid-Cretaceous cooling pulse can be linked to fault reactivation. AT-246 preserves a record of an older thermo-tectonic event, while AT-252 was exhumed differentially with respect to AT-246 during fault displacement. The mechanism of the Early Cretaceous exhumation and deformation can be attributed to (i) the collision of Lhasa with Eurasia (Dumitru et al. 2001) or (ii) extension in the Tethys Ocean (Zahirovic et al. 2016).

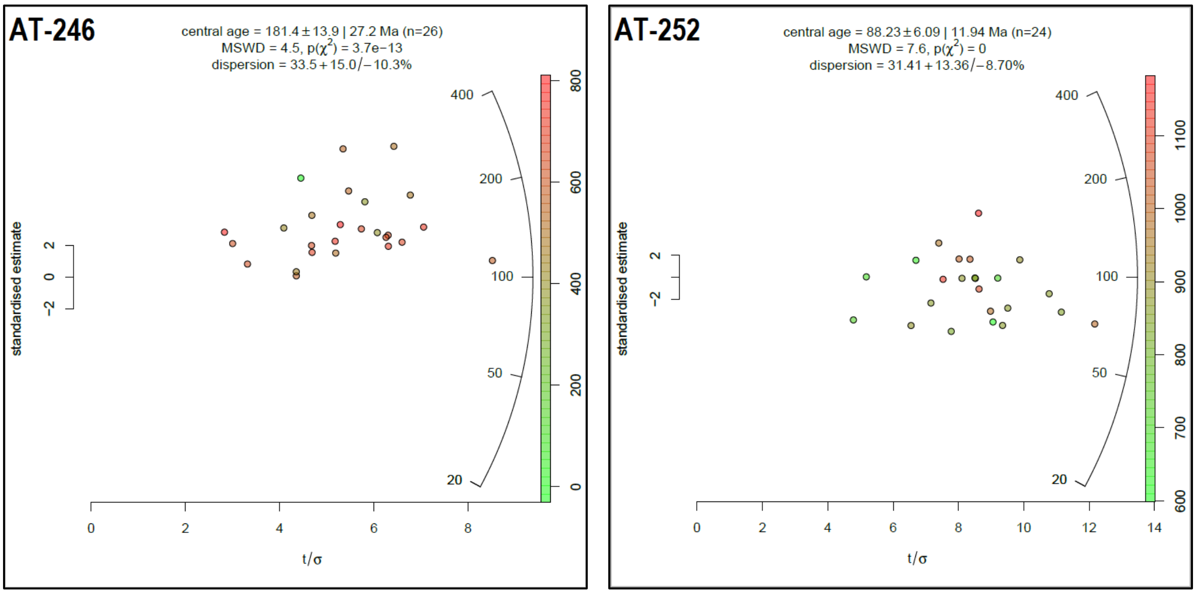

Figure 19 – Radial plots of calculated AFT ages for samples AT-246 and AT-252 using RadialPlotter software (Vermeesch, 2009). The Right y axis represents the 2σ from the calculated central AFT age values, the left y axis represents the age in Ma. The x axis represents the uncertainties of the single grain ages and decreases from left to right. The colour scale represents the ^{35}Cl concentration in ppm within the analysed grains.

5.5 Interpretation and discussion of the thermo-tectonic history of the Qilian Shan

5.5.1 LATE TRIASSIC-EARLY JURASSIC (CLOSURE OF PAO AND THE QIANGTANG COLLISION)

Evidence for Late Triassic-Early Jurassic rapid cooling was preserved in samples from Groups 1, 3 and 4 (Figures 12-15). This cooling is interpreted to be associated with the closure of the Palaeo-Asian Ocean and the accretion of the Qiangtang Block along the southern margin of Eurasia. Cooling in response to the Qiangtang collision is supported by zircon fission track analysis by Jolivet et al. (2010) which yielded ages of ~221 ± 22 Ma. Following the timing of the Qiangtang Collision, a reheating event was observed in samples AT-240, AT-242 and AT-244 interpreted to be due to burial associated with the increase in exhumation and denudation of the Qilian Shan. Late Jurassic conglomerates, present within the Tarim Basin (Chang et al. 2014, Glorie and De Grave 2016) support the interpreted reheating event and coincide with the timing of the closure of the PAO and the accretion of the Qiangtang Block. Models obtained in this study support the recent AFT study by Song et al. (2018) on the Alxa Tectonic Belt, to the north of the Qilian Shan. This study interpreted models displaying a reheating event to be caused in response to the closure of the Palaeo-Asian Ocean with the burial/reheating event interpreted as denudation of Permian-Triassic strata.

5.5.2 CRETACEOUS (LHASA COLLISION AND EXTENSION IN THE TETHYS OCEAN)

The early Cretaceous period was marked by the collision of the Lhasa Block with Eurasia (Jolivet et al. 2001, Qi et al. 2016). The rapid cooling event recorded by several samples in the study area is interpreted to be related with the Lhasa Collision, consistent with previous studies in the area (Baotian et al. 2013, Qi et al. 2016). Similar Cretaceous cooling was observed in the Alxa Tectonic Belt, suggesting both regions experienced simultaneous similar thermo-tectonic events in the Cretaceous (Song et al. 2018).

While previous studies attribute the rapid cooling seen in the Cretaceous solely to the Lhasa Collision (Baotian et al. 2013, Qi et al. 2016), a recent study by Zahirovic et al. (2016) suggested slab-rollback is thought to have initiated back-arc extension in the Tethys Ocean during the early-middle Cretaceous (~145-120 Ma), following the Lhasa Collision. The mid-Cretaceous cooling observed in this study within the thermal models for Group 2, is contemporaneous with the timing of extension in the Tethys Ocean. Jolivet et al. (2001) reported that since ~90 Ma, the tectonic activity in the Da Qaidam area changed from compression to extension, further supporting the theory that Tethys back-arc extension may be responsible for exhumation and cooling observed within the Qilian Shan at this time.

5.5.3 LATE CRETACEOUS – PALAEOGENE: TECTONIC QUIESCENCE

Previous studies (Qi et al. 2016, Baotian et al. 2013) have interpreted slow cooling from the Late Cretaceous-Early Eocene as a period of tectonic quiescence. In this study, samples from Groups 1 and 3 both show long periods of slow cooling between ~140-20 Ma. Prolonged periods of peneplanation have been observed in the entire Central Asian Orogenic Belt to the north (Arzhannikova et al. 2013 and references therein). A period of tectonic quiescence is further supported by a lack of Palaeocene and Eocene sedimentary rock in the Juixi Basin, suggesting a hiatus in sedimentary deposition during that time (Bovet et al. 2009).

5.5.3 MIOCENE (INDIA-EURASIA)

All samples in this study record an Oligocene-Miocene cooling phase. This rapid cooling pulse can be interpreted to be in response to the India-Eurasia Collision at the southern Eurasian margin. Thermal history models from this study suggest the Cenozoic uplift of the Qilian Shan began between ~30-20 Ma. A Magnetostratigraphic analysis of sediments in the

Caogou section of the Juixi Basin revealed that the section formed between ~24.2 Ma and ~2.8 Ma (Wang et al. 2016). A total of 950m of Cenozoic strata was deposited with a sharp sediment accumulation rate at ~13.5 Ma and ~10.5 Ma (Wang et al. 2016). The models for this thesis support a rapid increase in cooling rates between ~20-10 Ma attributed to the exhumation and erosion of the Qilian Shan. Further studies (Song et al. 2001) on the Laojunmiao Section, a 1960 m thick sequence of the Juixi Basin, shows three phases of sedimentary evolution, (i) low sedimentation rates between ~13-8 Ma; (ii) gradually increasing sedimentation rates between ~8 and 5 Ma and (iii) fast sedimentation rates since ~3.7 Ma. Thick packages of Quaternary strata (3200m in some areas) are found within the Qaidam Basin (Gu and Di 1989, Wang et al. 1986), which further support the claim of exhumation and denudation being prevalent in the Qilian Shan during this time period. Previous AFT studies in the Qilian Shan (Sun et al. 2018, Baotian et al. 2013, Zheng et al. 2017 and references therein, George et al. 2001) report AFT ages of ~32-8 Ma, supporting the rapid cooling pulse during the Oligocene-Miocene in the thermal history models for this study. All studies concur the India-Eurasia Collision to be responsible for rapid cooling phase in the Oligocene-Miocene.

6 CONCLUSIONS

AU-Pb and AFT results from the Qilian Shan record post-magmatic cooling in the Late Triassic-Early Jurassic and at least 2 further cooling events during the Middle-Late Cretaceous and the Late Cenozoic.

1) Late Triassic-Early Jurassic cooling and exhumation (~240-180 Ma) can be linked to the closure of the Palaeo-Asian Ocean and the collision of the Qiangtang block with southern Eurasia.

2) A second pulse of rapid cooling during the middle-late Cretaceous (~130-75 Ma) was obtained for samples near major shear zones along the steepest slopes of the Qilian Shan, which can be linked to the accretion of the Lhasa Block and/or extension of the Tethys Ocean.
3) All samples record thermal quiescence between ~140-20 Ma.
4) All thermal history models record rapid cooling during the late Palaeogene – Neogene, which can be attributed to stress-propagation from the far-field India-Eurasia collision and convergence.

7 ACKNOWLEDGEMENTS

Thank you to my supervisor Stijn Glorie and PhD students Jack Gillespie, Angus Nixon and Alex Simpson for their assistance throughout the project. Juraj Farkas and Katie Howard are also thanked for supporting the entire honours cohort throughout the year. I would also like to thank Sarah Gilbert for her assistance with the LA-ICP-MS equipment and optical microscopes provided by Adelaide Microscopy. Thank you to everybody in the honours cohort of 2019 for the continuous laughs and good times over the year. Lastly, I would like to give a massive thank you to all my friends and family for their support over the year.

8 REFERENCES

ARZHANNIKOVA, A. V., JOLIVET, M., ARZHANNIKOV, S. G., VASSALLO, R., & CHAUVET, A. (2013). The time of the formation and destruction of the Meso-Cenozoic peneplanation surface in East Sayan. *Russian Geology and Geophysics, 54*(7), 685-694. doi:10.1016/j.rgg.2013.06.004

BAOTIAN, P., QINGYANG, L., XIAOFEI, H., HAOPENG, G., ZIBIAN, L., SHAOFEI, J., & WANMING, Y. (2013). Cretaceous and Cenozoic cooling history of the eastern Qilian Shan, north-eastern margin of the Tibetan Plateau: evidence from apatite fission-track analysis. *Terra Nova, 25*(6), 431-438. doi:10.1111/ter.12052

BOVET, P. M., RITTS, B. D., GEHRELS, G., ABBINK, A. O., DARBY, B., & HOURIGAN, J. (2009). Evidence of Miocene crustal shortening in the North Qilian Shan from Cenozoic stratigraphy of the western Hexi Corridor, Gansu Province, China. *American Journal of Science, 309*(4), 290-329. doi:10.2475/00.4009.02

CHANG, J., BROWN, R. W., YUAN, W., LI, W., QUE, Y., & QIU, N. (2014). Mesozoic cooling history of the “Bachu Uplift” in the Tarim Basin, China: Constraints from zircon fission-track thermochronology. *Radiation Measurements, 67*, 5-14. doi:10.1016/j.radmeas.2014.05.019

CHENG, F., JOLIVET, M., FU, S., ZHANG, C., ZHANG, Q., & GUO, Z. (2016). Large-scale displacement along the Altyn Tagh Fault (North Tibet) since its Eocene initiation: Insight from detrital zircon U–Pb geochronology and subsurface data. *Tectonophysics, 677-678*(C), 261-279. doi:10.1016/j.tecto.2016.04.023

CHEW, D. M., PETRUS, J. A., & KAMBER, B. S. (2014). U–Pb LA–ICPMS dating using accessory mineral standards with variable common Pb. *Chemical Geology, 363*(C), 185-199. doi:10.1016/j.chemgeo.2013.11.006

COWGILL, E., YIN, A., HARRISON, T. M., & XIAO-FENG, W. (2003). Reconstruction of the Altyn Tagh fault based on U-Pb geochronology: Role of back thrusts, mantle sutures, and heterogeneous crustal strength in forming the Tibetan Plateau. *Journal of Geophysical Research: Solid Earth, 108*(B7), n/a-n/a. doi:10.1029/2002JB002080

DOUWE, J. J. V. H., PETER, C. L., GUILLAUME, D.-N., NADINE, M., PAVEL, V. D., WIM, S., & TROND, H. T. (2012). Greater India Basin hypothesis and a two-stage Cenozoic collision between India and Asia. *Proceedings of the National Academy of Sciences, 109*(20), 7659. doi:10.1073/pnas.1117262109

DUMITRU, T. A., ZHOU, D., CHANG, E. Z., GRAHAM, S. A., HENDRIX, M. S., SOBEL, E. R., & CARROLL, A. R. (2001). Uplift, exhumation, and deformation in the Chinese Tian Shan. *Memoir of the Geological Society of America, 194*, 71-99. doi:10.1130/0-8137-1194-0.71

DUVALL, A., CLARK, M., KIRBY, E., FARLEY, K., CRADDOCK, W., LI, C., & YUAN, D. (2013). Low-temperature thermochronometry along the Kunlun and Haiyuan Faults, NE Tibetan Plateau: Evidence for kinematic change during late-stage orogenesis. *Tectonics, 32*(5), 1190-1211. doi:10.1002/tect.20072

DUVALL, A. R., & CLARK, M. K. (2010). Dissipation of fast strike-slip faulting within and beyond northeastern Tibet.(Author abstract)(Report). *Geology, 38*(3), 223. doi:10.1130/G30711.1

FANG, X., ZHANG, W., MENG, Q., GAO, J., WANG, X., KING, J., MIAO, Y. (2007). High-resolution magnetostratigraphy of the Neogene Huaitoutala section in the eastern Qaidam Basin on the NE Tibetan Plateau, Qinghai Province, China and its implication on tectonic uplift of the NE Tibetan Plateau. *Earth and Planetary Science Letters, 258*(1), 293-306. doi:10.1016/j.epsl.2007.03.042

FITZGERALD, P. G., STUMP, E., & REDFIELD, T. (1993). Late Cenozoic uplift of Denali and its relation to relative plate motion and fault morphology. *Science, 259*(5094), 497-499.

FU, B., & AWATA, Y. (2007). Displacement and timing of left-lateral faulting in the Kunlun Fault Zone, northern Tibet, inferred from geologic and geomorphic features. *Journal of Asian Earth Sciences, 29*(2), 253-265. doi:10.1016/j.jseaes.2006.03.004

GAUDEMER, Y., TAPPONNIER, P., MEYER, B., PELTZER, G., SHUNMIN, G., ZHITAI, C., CIFUENTES, I. (1995). Partitioning of crustal slip between linked, active faults in the eastern Qilian Shan, and evidence for a major seismic gap, the ‘Tianzhu gap', on the western Haiyuan Fault, Gansu (China. *Geophysical Journal International, 120*(3), 599-645. doi:10.1111/j.1365-246X.1995.tb01842.x

GEHRELS, G., YIN, A., & WANG, X. (2003). Detrital-zircon geochronology of the northeastern Tibetan plateau. *Geol. Soc. Am. Bull., 115*(7), 881-896.

GEORGE, A., MARSHALLSEA, S., WYRWOLL, K.-H., & CHEN, J. (2001). Miocene cooling in the northern Qilian Shan, northeastern margin of the Tibetan Plateau, revealed by apatite fission-track and vitrinite-reflectance analysis. *Geology, 29*(10), 939-942. doi:10.1130/0091-7613(2001)029<0939:MCITNQ>2.0.CO2

GILLESPIE, J., GLORIE, S., XIAO, W., ZHANG, Z., COLLINS, A. S., EVANS, N., DE GRAVE, J. (2017). Mesozoic reactivation of the Beishan, southern Central Asian Orogenic Belt: Insights from low-temperature thermochronology. *Gondwana Research, 43*(C), 107-122. doi:10.1016/j.gr.2015.10.004

GLEADOW, A., DUDDY, I., GREEN, P., & LOVERING, J. (1986). Confined fission track lengths in apatite: a diagnostic tool for thermal history analysis. *Contributions to Mineralogy and Petrology, 94*(4), 405-415. doi:10.1007/BF00376334

GLORIE, S., ALEXANDROV, I., NIXON, A., JEPSON, G., GILLESPIE, J., & JAHN, B.-M. (2017). Thermal and exhumation history of Sakhalin Island (Russia) constrained by apatite U-Pb and fission track thermochronology. *Journal of Asian Earth Sciences, 143*, 326-342. doi:10.1016/j.jseaes.2017.05.011

GLORIE, S., & DE GRAVE, J. (2016). Exhuming the Meso–Cenozoic Kyrgyz Tianshan and Siberian Altai-Sayan: A review based on low-temperature thermochronology. *Geoscience Frontiers, 7*(2), 155-170. doi:10.1016/j.gsf.2015.04.003

GREEN, P. F., DUDDY, I. R., GLEADOW, A. J. W., TINGATE, P. R., & LASLETT, G. M. (1986). Thermal annealing of fission tracks in apatite: 1. A qualitative description. *Chemical Geology: Isotope Geoscience Section, 59*(C), 237-253. doi:10.1016/0168-9622(86)90074-6

GU, S., & DI, H. (1989). Mechanism of formation of the Qaidam basin and its control on petroleum. In X. Zhu (Ed.), *Chinese Sedimentary Basins* (pp. 45-51).

GUO, Z., LU, J., & ZHANG, Z. (2009). Cenozoic Exhumation and Thrusting in the Northern Qilian Shan, Northeastern Margin of the Tibetan Plateau: Constraints from Sedimentological and Apatite Fission-Track Data. *Acta Geologica Sinica - English Edition, 83*(3), 562-579. doi:10.1111/j.1755-6724.2009.00045.x

HE, P., SONG, C., WANG, Y., MENG, Q., CHEN, L., YAO, L., CHEN, S. (2018). Cenozoic deformation history of the Qilian Shan (northeastern Tibetan Plateau) constrained by detrital apatite fission-track thermochronology in the northeastern Qaidam Basin. *Tectonophysics, 749*, 1-11. doi:10.1016/j.tecto.2018.10.017

HU, C., CHEN, N., KAPP, P., CHEN, J., XIAO, A., & ZHAO, Y. (2017). Yardang geometries in the Qaidam Basin and their controlling factors. *Geomorphology, 299*, 142-151. doi:10.1016/j.geomorph.2017.09.029

JIAN, X., GUAN, P., ZHANG, W., & FENG, F. (2013). Geochemistry of Mesozoic and Cenozoic sediments in the northern Qaidam basin, northeastern Tibetan Plateau: Implications for provenance and weathering. *Geochemistry of Mesozoic and Cenozoic sediments in the northern Qaidam basin, northeastern Tibetan Plateau: Implications for provenance and weathering, 360*, 74-88.

JOLIVET, M., BRUNEL, M., SEWARD, D., XU, Z., YANG, J., MALAVIEILLE, J., WU, C. (2003). Neogene extension and volcanism in the Kunlun Fault Zone, northern Tibet: New constraints on the age of the Kunlun Fault. *Tectonics, 22*(5), n/a-n/a. doi:10.1029/2002TC001428

JOLIVET, M., BRUNEL, M., SEWARD, D., XU, Z., YANG, J., ROGER, F., WU, C. (2001). Mesozoic and Cenozoic tectonics of the northern edge of the Tibetan plateau: fission-track constraints. *Tectonophysics, 343*(1), 111-134. doi:10.1016/S0040-1951(01)00196-2

JOLIVET, R., LASSERRE, C., DOIN, M. P., GUILLASO, S., PELTZER, G., DAILU, R., XU, X. (2012). Shallow creep on the Haiyuan Fault (Gansu, China) revealed by SAR Interferometry. *Journal of Geophysical Research: Solid Earth, 117*(B6), n/a-n/a. doi:10.1029/2011JB008732

KIDD, W. S. F., & MOLNAR, P. (1988). Quaternary and Active Faulting Observed on the 1985 Academia Sinica--Royal Society Geotraverse of Tibet. *Philosophical Transactions of the Royal Society of London. Series A, Mathematical and Physical Sciences (1934-1990), 327*(1594), 337-363. doi:10.1098/rsta.1988.0133

KUHLEMANN, J., & RAHN, M. (2013). Plio-Pleistocene landscape evolution in Northern Switzerland. *Swiss Journal of Geosciences, 106*(3), 451-467. doi:10.1007/s00015-013-0152-6

LASSERRE, C., GAUDEMER, Y., TAPPONNIER, P., KING, G. C. P., & METIVIER, F. (1999). Postglacial left slip rate and past occurrence of M[ge]8 earthquakes on the western Haiyuan fault, Gansu, China. *Journal of Geophysical Research, 104*(B8). doi:10.1029/1998JB900082

LI, B., CHEN, X., ZUZA, A. V., HU, D., DING, W., HUANG, P., & XU, S. (2019). Cenozoic cooling history of the North Qilian Shan, northern Tibetan Plateau, and the initiation of the Haiyuan fault: Constraints from apatite- and zircon-fission track thermochronology. *Tectonophysics, 751*, 109-124. doi:10.1016/j.tecto.2018.12.005

LI, C., ZHANG, P. Z., YIN, J., & MIN, W. (2009). Late Quaternary left-lateral slip rate of the Haiyuan fault, northeastern margin of the Tibetan Plateau. *Tectonics, 28*(5), n/a-n/a. doi:10.1029/2008TC002302

LIN, X., CHEN, H., WYRWOLL, K.-H., BATT, G. E., LIAO, L., & XIAO, J. (2011). The Uplift History of the Haiyuan-Liupan Shan Region Northeast of the Present Tibetan Plateau: Integrated Constraint from Stratigraphy and Thermochronology. *The Journal of Geology, 119*(4), 372-393. doi:10.1086/660190

MCDOWELL, F. W., MCINTOSH, W. C., & FARLEY, K. A. (2005). A precise 40Ar– 39Ar reference age for the Durango apatite (U–Th)/He and fission-track dating standard. *Chemical Geology, 214*(3-4), 249-263. doi:10.1016/j.chemgeo.2004.10.002

METIVIER, F., GAUDEMER, Y., TAPPONNIER, P., & MEYER, B. (1998). Northeastward growth of the Tibet plateau deduced from balanced reconstruction of two depositional areas: The Qaidam and Hexi Corridor basins, China. *Tectonics, 17*(6), 823-842. doi:10.1029/98TC02764

PAN, B., HU, X., GAO, H., HU, Z., CAO, B., GENG, H., & LI, Q. (2013). Late Quaternary river incision rates and rock uplift pattern of the eastern Qilian Shan Mountain, China. *Geomorphology, 184*, 84-97. doi:10.1016/j.geomorph.2012.11.020

PATON, C., HELLSTROM, J., PAUL, B., WOODHEAD, J., & HERGT, J. (2011). Iolite: Freeware for the visualisation and processing of mass spectrometric data. *J. Anal. At. Spectrom., 26*(12), 2508-2518. doi:10.1039/c1ja10172b

QI, B., HU, D., YANG, X., ZHANG, Y., TAN, C., ZHANG, P., & FENG, C. (2016). Apatite fission track evidence for the Cretaceous–Cenozoic cooling history of the Qilian Shan (NW China) and for stepwise northeastward growth of the northeastern Tibetan Plateau since early Eocene. *Journal of Asian Earth Sciences, 124*, 28-41. doi:10.1016/j.jseaes.2016.04.009

SCHOENE, B., & BOWRING, S. (2006). U–Pb systematics of the McClure Mountain syenite: thermochronological constraints on the age of the 40 Ar/ 39 Ar standard MMhb. *Contributions to Mineralogy and Petrology, 151*(5), 615-630. doi:10.1007/s00410-006-0077-4

SONG, C., FANG, X., LI, J., GAO, J., ZHAO, Z., & FAN, M. (2001). Tectonic uplift and sedimentary evolution of the Jiuxi Basin in the northern margin of the Tibetan Plateau since 13 Ma BP. *Science in China Series D: Earth Sciences, 44*(1), 192-202. doi:10.1007/bf02911987

SONG, D., GLORIE, S., XIAO, W., COLLINS, A. S., GILLESPIE, J., JEPSON, G., & LI, Y. (2018). Tectono-thermal evolution of the southwestern Alxa Tectonic Belt, NW China: Constrained by apatite U-Pb and fission track thermochronology. *Tectonophysics, 722*, 577-594. doi:10.1016/j.tecto.2017.11.029

SUN, G.-Q., LIU, W.-M., GUO, J.-J., & WANG, Y.-T. (2018). Fission-track evidence of tectonic evolution in the northwestern Qaidam Basin, China. *Published by the Indian Academy of Sciences, 127*(1), 1-12. doi:10.1007/s12040-017-0914-z

TADA, R., ZHENG, H., & CLIFT, P. (2016). Evolution and variability of the Asian monsoon and its potential linkage with uplift of the Himalaya and Tibetan Plateau. *Progress in Earth and Planetary Science, 3*(1), 1-26. doi:10.1186/s40645-016-0080-y

TAPPONNIER, P., MEYER, B., AVOUAC, J. P., PELTZER, G., GAUDEMER, Y., GUO SHUNMIN, Y., DAI HUAGANG, Y. (1990). Active thrusting and folding in the Qilian Shan, and decoupling between upper crust and mantle in northeastern Tibet. *Earth and Planetary Science Letters, 97*(3), 382,387-383,403. doi:10.1016/0012-821X(90)90053-Z

TAPPONNIER, P., & MOLNAR, P. (1977). Active faulting and tectonics in China. *Journal of Geophysical Research, 82*(20), 2905-2930. doi:10.1029/JB082i020p02905

TAPPONNIER, P., PELTZER, G., & ARMIJO, R. (1986). On the mechanics of the collision between India and Asia. *Geological Society Special Publication, 19*(1), 113-157. doi:10.1144/GSL.SP.1986.019.01.07

TAPPONNIER, P., ZHIQIN, X., ROGER, F., MEYER, B., ARNAUD, N., WITTINGER, G., & JINGSUI, Y. (2001). Oblique stepwise rise and growth of the tibet plateau. (Review: Geology). *Science, 294*(5547), 1671. doi:10.1126/science.105978

VERMEESCH, P. (2009). RadialPlotter: A Java application for fission track, luminescence and other radial plots. *Radiation Measurements, 44*(4), 409-410. doi:10.1016/j.radmeas.2009.05.003

VERMEESCH, P. (2017). Statistics for LA-ICP-MS based fission track dating. *Chemical Geology, 456*(C), 19-27. doi:10.1016/j.chemgeo.2017.03.002

WAGNER, G., GLEADOW, A., & FITZGERALD, P. G. (1989). The significance of the partial annealing zone in apatite fission-track analysis - projected track length measurements and uplift chronology of the Transantarctic Mountains. *Chem. Geol., 79*(4), 295-305.

WANG, J., WANG, Y. J., LIU, Z. C., LI, J. Q., & XI, P. (1999). Cenozoic environmental evolution of the Qaidam Basin and its implications for the uplift of the Tibetan Plateau and the drying of central Asia. *Palaeogeography, Palaeoclimatology, Palaeoecology, 152*(1-2), 37-47. doi:10.1016/S0031-0182(99)00038-3

WANG, J. T., DERBYSHIRE, E., & SHAW, J. (1986). Preliminary magnetostratigraphy of Dabusun Lake, Qaidam Basin, Central Asia. *Phys. Earth Planet. Inter, 44*, 41-46.

WANG, Q. M., & COWARD, M. P. (1993). The Jiuxi Basin, Hexi Corridor, nw China: foreland structural features and hydrocarbon potential. *Journal of Petroleum Geology, 16*(2), 169-182. doi:10.1111/j.1747-5457.1993.tb00104.x

WANG, W., ZHANG, P., PANG, J., GARZIONE, C., ZHANG, H., LIU, C., YU, J. (2016). The Cenozoic growth of the Qilian Shan in the northeastern Tibetan Plateau: A sedimentary archive from the Jiuxi Basin. *Journal of Geophysical Research: Solid Earth, 121*(4), 2235-2257. doi:10.1002/2015JB012689

XIAOMIN, F., YAN, M., VAN DER VOO, R., REA, D. K., CHUNHUI, S., PARES, J. M., . . . SHUANG, D. (2005). Late Cenozoic deformation and uplift of the NE Tibetan Plateau: evidence from high-resolution magnetostratigraphy of the Guide Basin, Qinghai Province, China.(Author Abstract). *The Geological Society of America Bulletin, 117*(9), 1208. doi:10.1130/B25727.1

YANG, W., FU, L., WU, C., SONG, Y., JIANG, Z., LUO, Q., ZHU, B. (2018). U-Pb ages of detrital zircon from Cenozoic sediments in the southwestern Tarim Basin, NW China: Implications for Eocene–Pliocene source-to-sink relations and new insights into Cretaceous–Paleogene magmatic sources. *Journal of Asian Earth Sciences, 156*, 26-40. doi:10.1016/j.jseaes.2018.01.010

YIN, A., DANG, Y.-Q., WANG, L.-C., JIANG, W.-M., ZHOU, S.-P., CHEN, X.-H., MCRIVETTE, M. W. (2008). Cenozoic tectonic evolution of Qaidam basin and its surrounding regions (Part 1): the southern Qilian Shah-Nan Shah thrust belt and northern Qaidam basin. *The Geological Society of America Bulletin, 120*(7 8), 813. doi:10.1130/B26180.1

YIN, A., DANG, Y. Q., ZHANG, M., CHEN, X. H., & MCRIVETTE, M. W. (2008). Cenozoic tectonic evolution of the Qaidam basin and its surrounding regions (Part 3): Structural geology, sedimentation, and regional tectonic reconstruction. *Geological Society of America Bulletin, 120*(7-8), 847-876. doi:10.1130/b26232.1

YIN, A., & HARRISON, T. M. (2000). Geologic Evolution of the Himalayan-Tibetan Orogen. *Annu. Rev. Earth Planet. Sci., 28*(1), 211-280. doi:10.1146/annurev.earth.28.1.211

YIN, A., RUMELHART, P., BUTLER, R., COWGILL, E., HARRISON, T. M., FOSTER, D., RAZA, A. (2002). Tectonic history of the Altyn Tagh fault system in northern Tibet inferred from Cenozoic sedimentation. In *Geol. Soc. Am. Bull.* (Vol. 114, pp. 1257-1295).

ZAHIROVIC, S., MATTHEWS, K. J., FLAMENT, N., MÜLLER, R. D., HILL, K. C., SETON, M., & GURNIS, M. (2016). Tectonic evolution and deep mantle structure of the eastern Tethys since the latest Jurassic. *Earth-Science Reviews, 162*(C), 293-337. doi:10.1016/j.earscirev.2016.09.005

ZHANG, H., ZHANG, P., PRUSH, V., ZHENG, D., ZHENG, W., WANG, W., REN, Z. (2017). Tectonic geomorphology of the Qilian Shan in the northeastern Tibetan Plateau: Insights into the plateau formation processes. *Tectonophysics, 706-707*, 103-115. doi:10.1016/j.tecto.2017.04.016

ZHANG, J., REN, J., CHEN, C., FU, J., YANG, P., XIONG, R., & HU, C. (2014). The Late Pleistocene activity of the eastern part of east Kunlun fault zone and its tectonic significance. *Science China Earth Sciences, 57*(3), 439-453. doi:10.1007/s11430-013-4759-2

ZHENG, D., WANG, W., WAN, J., YUAN, D., LIU, C. R., ZHENG, W., ZHANG, P. (2017). Progressive northward growth of the northern Qilian Shan-Hexi Corridor (northeastern Tibet) during the Cenozoic. *Lithosphere, 9*(3), 408-416. doi:10.1130/L587.1

9. Appendix A: Extended methods

9.1 Laboratory Processing

Samples were collected in the Qilian Shan by Prof Marc Jolivet and prepared by crushing, sieving and mineral separation using a combination of magnetic and heavy liquid processing at the University of Rennes 1, France. Rasters of approximately 100 individual apatite grains (depending on grain availability) were picked and mounted onto double sided tape under two Olympus SZ61 microscopes with magnifications of x45, with grains positioned in such a way that the c-axis was parallel to the tape surface.

Mounting of the grains was achieved by using EpoxyCure resin with a mixture ratio of 5g resin to 1.15g epoxy hardener. Two thin section slides were laid on the far ends of the taped slide, then resin was poured over the raster of grains. A glass microscope slide was gently placed over the resin to ensure adhesion to the slide. The resin was left to set for 48 hours to ensure proper embedding of the grains before the tape was removed with a razor blade and cleaned with ethanol to remove the tape residue. To expose the grains, the top of the mount was grinded on wet #2000 silicon carbide paper for 20 seconds in figure 8 patterns. Following the grinding process, the samples were analysed under a 10x optical microscope to ensure apatite grain surfaces displayed an abundance of scratches. Samples not showing sufficient scratches underwent the grinding process again. Following grinding, the samples were polished using Struers TegraPol polishing system, first being polished using 3μm diamond suspension fluid combined with a 3μm polishing cloth for 20 minutes. Samples were then subject to further polishing using a 1μm diamond suspension fluid alongside a 1 μm polishing cloth for 6 minutes.

Samples were subject to analysis using a Zeiss AXIO Imager M2m Autoscan System, with samples not displaying a sufficient level of polishing being further polished with the 1μm setup. Once suitably polished, the mounts were etched to reveal fission tracks for counting. Each sample was etched in a solution of 5.5M nitric acid (HNO_3) at 20±0.5°C for 20±0.5 seconds, then immediately washed in deionised water to remove the residual nitric acid and ensure all samples had been etched for a consistent period of time. The mounts were then coated with a 3nm layer of gold to assist in imaging of the grains.

9.2 Apatite Fission Track Counting

Apatite grains were imaged at Adelaide Microscopy with a Zeiss AXIO Imager M2m Autoscan System at a magnification of x1000 using FastTracks software. In each sample, the target was to image 40 individual grains of at least 30 μm in width. Samples containing less than 10 apatite grains with low track densities were excluded from further analysis.

Using TrackWorks software, regions of interests (ROIs) were defined on each imaged grain. The ROI must be defined so that the software can auto-count tracks and perform track density calculations. Once the ROIs were defined, the software attempts to work out what surface features are fission tracks within the ROIs. After adjusting parameters such as area and circularity, the grains were manually reviewed and changes to the number of fission tracks were done as necessary.

For later modelling use, confined tracks (fission tracks that are entirely beneath the grains surface) were measured using the TrackWorks software. The timing of passage through the apatite partial annealing zone (APAZ) that occurs between ~ 120-60°C (Wagner et al. 1989) can be modelled using the confined track lengths. The measuring of confined tracks is not limited to the grains that were used to count fission tracks. Confined fission tracks are defined TINTs when etching acid enters through an intersecting fission track and TINCLEs when acid enters grain cracks/cleavages (Gleadow et al. 1986). All apatite grains in the sample can have their confined tracks measured. 100 track lengths was the target to generate successful thermal history models with 30 tracks being the absolute minimum amount needed to model with.

9.3 LA-ICP-MS analysis

LA-ICP-MS was used to determine elemental concentrations (e.g. U, Pb and Cl) in apatite. A laser beam of 29µm was used (analytical details in Table 1), focused on areas of homogeneous fission track density. Each laser ablation session required a block of standards before every block of 10 ‘unknown’ grains. Standard blocks contained 1x Durango, 1x McClure, 2x Madagascar apatite standards and 2x NIST 610 standards.

9.4 Data Reduction

The process of data reduction was achieved using the Iolite software (Paton et al. 2011) utilising the Madagascar apatite as the primary standard for the U-Pb analysis and NIST 610 for the primary standard in AFT analysis. To test the accuracy of the analysed data, secondary standards of Durango (Chew et al. 2014) and McClure (Schoene and Bowring 2006) apatite were used.

In house Excel spreadsheets were used to calculate the apatite fission track ages by comparing the ^{238}U concentrations obtained from the LA-ICP-MS against the number of spontaneous fission tracks in each grain. This was done by following the methodology outlined in (Gillespie et al. 2017) and (Glorie et al. 2017).

Analysis of the standard Durango apatite and the unknown samples were completed simultaneously. A zeta calibration factor was calculated for unknown samples (using the ^{238}U concentrations and fission track densities of Durango apatites) and applied to the calculated AFT ages (Vermeesch 2017) to minimise the uncertainty of fission track analysis, by comparing unknown data to a known standard, in this case Durango apatite.

9.5 ^{252}Cf Fission Fragments Irradiation

Samples in this study with less than 60 confined tracks were exposed to Californium in order to induce further confined tracks to assist in the generation of more accurate models. Samples requiring californium exposure were cleaned of gold plating, reground and polished. After cooling down, the samples were etched, gold plated once more, imaged and finally, the confined tracks were remeasured.

9.6 Radial Plots

Radial plots were produced using the Java plugin RadialPlotter (Vermeesch, 2009, 2017) in order to determine the central AFT ages and associated uncertainties of samples. Samples that passed the X^2 test (chi^2) with values greater than 0.05 and recorded single grain age dispersions of less than 25% were considered to constrain a single AFT age population. In comparison, samples that failed the X^2 test or recorded single-grain age dispersions greater than 25% were considered to contain multiple age populations (Galbraith & Laslett, 1993). RadialPlotter was used in order to statistically define age populations. Chlorine weight percent (wt %) was input to observe whether trends showing differential annealing of fission tracks were present in the samples. Higher Cl has been correlated with higher closure temperatures in apatite and track which samples are thermally resistant (Green et al. 1986).

9.7 Low Temperature Thermal History Modelling

Thermal history modelling of the samples was completed in the QTQt software (Gallagher, 2012). Inputs used for modelling included single grain AFT age with the uncertainty, number of counted fission tracks, weight percent (wt%) of chlorine within each grain, confined fission track lengths and the angle of the lengths to the C-axis.

The granite samples were constrained beneath the APAZ with U-Pb ages at temperatures of 475 ± 75ºC in order to model the rock evolution through the APAZ. The models were further constrained to a present day temperature range of 25 ± 5ºC.

A Monte-Carlo approach was used during modelling, with the best models being retained based on the fit between model data and measured data. Initially, the models created were conducted by running 10,000 possible models (10,000 Burn-in and 10,000 Post-Burn-in) to determine the plausibility of the thermal history model. Models found to be statistically significant were then further refined by running a second simulation with an extra 200,000 models (200,000 Burn-in and 200,000 Post-Burn-in).

10. APPENDIX B: AFT TABLE

Table 5 – Single grain AFT data used in this study for all samples, where ρs represents the average density of spontaneous fission tracks, Ns represents the number of tracks in each grain, $_{35}$Cl and $_{238}$U represent the average concentration measured in each grain with the 1σ value representing the uncertainty. t represents the age for each individual grain with the 1σ representing the uncertainty on the age value, calculated using in house spreadsheets (e.g. Gillespie et al., 2017b; Glorie et al., 2017)

Grain no.	ρs (x105/cm2)	Ns	Cl (ppm)	Cl 2SE	U (ppm)	U238 2SE	t (Ma)	1σ (Ma)
AT-202_1	4.60E+06	58	800	230	53.3	1.3	158.71	20.93
AT-202_2	4.12E+06	80	590	210	34.1	0.57	220.82	24.76
AT-202_4	4.85E+06	75	1160	270	53.6	1.1	166.23	19.27
AT-202_5	4.18E+06	40	930	320	71.1	1.6	108.47	17.19
AT-202_6	4.36E+06	92	680	270	43.7	1.1	182.84	19.2
AT-202_7	5.86E+06	93	900	100	55.6	1.1	193.18	20.12
AT-202_8	5.77E+06	47	840	150	52.07	0.97	202.89	29.65
AT-202_11	4.76E+06	49	1000	210	56.74	0.95	154.29	22.08
AT-202_12	5.35E+06	69	760	230	36.69	0.92	265.49	32.13
AT-202_15	5.31E+06	67	730	320	59.2	1.3	164.73	20.21
AT-202_16	3.23E+06	46	610	170	45.27	0.72	131.23	19.38
AT-202_17	3.07E+06	28	520	180	24.43	0.45	229.33	43.39
AT-202_18	5.41E+06	52	1090	300	51.2	1.4	193.55	26.97
AT-202_19	2.14E+06	16	600	150	28.17	0.42	140.03	35.02
AT-202_20	3.64E+06	46	Below LOD	0	63	1.8	106.67	15.8
AT-202_21	5.90E+06	68	1080	270	72.6	1.5	149.4	18.18
AT-202_22	4.81E+06	55	510	180	45.38	0.86	194.33	26.27
AT-202_27	4.29E+06	46	480	290	69.1	1.7	114.62	16.96
AT-202_29	4.06E+06	39	590	250	30.49	0.81	243.18	39.07
AT-202_31	5.01E+06	47	370	210	34.26	0.8	266.69	39.03
AT-202_33	4.41E+06	42	460	180	41.14	0.65	196.23	30.32
AT-202_36	4.08E+06	56	Below LOD	0	27.1	0.91	274.31	36.94
Grain no.	ρs (x105/cm2)	Ns	Cl (ppm)	Cl 2SE	U (ppm)	U238 2SE	t (Ma)	1σ (Ma)
AT-203_1	4.38E+05	8	6030	360	5.29	0.14	151.95	53.76
AT-203_2	3.18E+06	23	390	200	24.93	0.47	232.83	48.6
AT-203_5	1.95E+06	23	670	220	10.33	0.32	341.84	71.48
AT-203_6	1.61E+06	23	540	220	10.64	0.24	275.29	57.49
AT-203_7	1.49E+06	26	Below LOD	0	14.04	0.46	195.04	38.38
AT-203_8	3.76E+05	7	570	160	4.08	0.17	169.38	64.12
AT-203_9	1.93E+06	18	320	200	14.59	0.62	241.7	57.2
AT-203_12	2.36E+06	23	450	280	34.09	0.73	127.74	26.67
AT-203_14	3.86E+06	58	480	240	21.77	0.34	326.52	42.95
AT-203_16	2.16E+06	45	Below LOD	0	14.16	0.45	278.18	41.7
AT-203_17	2.11E+06	22	510	290	17.53	0.88	218.63	46.93
AT-203_18	2.43E+06	24	Below LOD	0	27.3	1.6	163.63	33.74
AT-203_19	1.44E+06	24	640	170	16.03	0.36	164.68	33.67
AT-203_21	1.88E+06	36	670	260	13.47	0.5	255.22	42.8
AT-203_22	2.57E+06	31	460	230	37.09	0.67	127.25	22.88

AT-203_23	1.38E+06	17	Below LOD	0	13.76	0.48	184.23	44.8
AT-203_24	1.24E+06	10	590	280	11.78	0.29	193.04	61.09
AT-203_25	8.30E+05	12	640	200	19.02	0.72	80.45	23.27
AT-203_26	3.19E+06	28	600	260	15.08	0.68	396.39	75.44
AT-203_28	2.75E+06	57	Below LOD	0	15.64	0.59	319.52	42.75
AT-203_33	1.92E+06	18	Below LOD	0	17.45	0.78	201.64	47.74
AT-203_34	2.54E+06	32	620	410	15.93	0.52	290	51.48
AT-203_35	1.57E+06	23	Below LOD	0	18.66	0.85	154.15	32.33
AT-203_36	1.30E+06	26	460	160	13.61	0.44	175.31	34.5
AT-203_39	3.77E+06	58	640	330	18.32	0.65	371.58	49.23
Grain no.	**ρs (x105/cm2)**	**Ns**	**Cl (ppm)**	**Cl 2SE**	**U (ppm)**	**U238 2SE**	**t (Ma)**	**1σ (Ma)**
AT-205_2	4.29E+06	36	620	180	58.35	0.82	135.2	22.6
AT-205_3	3.54E+06	33	560	230	49.5	1	131.7	23
AT-205_14	3.13E+06	51	570	320	36.36	0.7	158.1	22.2
AT-205_30	3.90E+06	51	Below LOD	0	46.73	0.86	153.2	21.5
AT-205_31	1.19E+06	17	380	180	13.57	0.35	161	39.1
AT-205_39	1.92E+06	33	410	180	27.67	0.63	127.7	22.3
Grain no.	**ρs (x105/cm2)**	**Ns**	**Cl (ppm)**	**Cl 2SE**	**U (ppm)**	**U238 2SE**	**t (Ma)**	**1σ (Ma)**
AT-206_1	9.57E+05	10	7800	2300	5.92	0.61	207.16	79.02
AT-206_3	2.43E+06	44	Below LOD	0	27.56	0.81	114.41	20.62
AT-206_4	1.64E+06	29	610	240	18.31	0.39	136.33	27.87
AT-206_11	2.92E+06	87	Below LOD	0	27.29	0.61	118	16.42
AT-206_12	1.72E+06	14	450	170	22.47	0.39	91.01	30.35
AT-206_16	2.07E+06	43	Below LOD	0	24.24	0.87	66.31	15.67
AT-206_19	2.06E+06	29	600	270	16.79	0.53	70.35	23.48
AT-206_21	3.01E+06	103	570	230	60.1	1.3	92.41	9.16
AT-206_24	1.36E+06	37	Below LOD	0	23.79	0.6	136.77	26.88
AT-206_26	1.98E+06	33	510	240	25.93	0.78	98.31	20.55
AT-206_27	1.76E+06	23	540	170	14.08	0.3	209.37	45.74
AT-206_28	1.61E+06	30	Below LOD	0	15.72	0.45	132.33	28.94
AT-206_29	1.40E+06	29	340	210	16.39	0.44	140.63	27.64
AT-206_30	2.82E+06	45	Below LOD	0	39.7	1.6	70.09	14.38
AT-206_31	2.70E+06	41	Below LOD	0	21.33	0.97	102.48	24.27
AT-206_36	5.18E+05	11	420	200	7.84	0.24	121.86	36.79
AT-206_37	4.84E+05	6	400	160	17.65	0.49	50.85	20.77
AT-206_38	1.65E+06	33	Below LOD	0	15.61	0.87	88.87	23.08
Grain no.	**ρs (x105/cm2)**	**Ns**	**Cl (ppm)**	**Cl 2SE**	**U (ppm)**	**U238 2SE**	**t (Ma)**	**1σ (Ma)**
AT-207_1	1.03E+06	16	Below LOD	0	11.68	0.42	161.3	40.4
AT-207_2	9.87E+05	31	400	210	13.36	0.22	136	24.5
AT-207_3	6.12E+05	12	Below LOD	0	9.69	0.25	116.5	33.7
AT-207_4	9.01E+05	21	650	390	21.92	0.97	76.1	16.7
AT-207_5	1.52E+06	43	550	170	25.31	0.6	111.1	17
AT-207_6	9.42E+05	35	410	200	19.03	0.39	91.3	15.5
AT-207_7	7.40E+05	26	660	220	20.53	0.42	66.8	13.1
AT-207_8	7.02E+05	14	540	270	8.82	0.43	146	39.2
AT-207_9	8.00E+05	23	Below LOD	0	11.9	0.33	123.7	25.8

AT-207_10	1.08E+06	41	460	290	14.11	0.33	140.4	22
AT-207_11	1.30E+06	36	Below LOD	0	23.58	0.47	101.7	17
AT-207_12	6.50E+05	14	Below LOD	0	19.22	0.72	62.7	16.8
AT-207_14	1.17E+06	30	470	260	17.92	0.59	119.6	21.9
AT-207_15	1.97E+06	**51**	860	320	**20.15**	**0.84**	**177.9**	**25.2**
AT-207_16	6.85E+05	15	Below LOD	0	12.78	0.27	99	25.6
AT-207_17	5.01E+05	5	470	260	12.72	0.35	72.9	32.6
AT-207_19	7.19E+05	10	490	410	10.88	0.29	121.9	38.6
AT-207_20	1.04E+06	16	660	490	12.48	0.44	152.1	38.1
AT-207_21	9.10E+05	17	570	200	12.76	0.45	131.2	31.9
AT-207_22	9.47E+05	25	620	180	12.93	0.3	134.8	27
AT-207_23	8.48E+05	18	Below LOD	0	13.2	0.43	118.6	28
AT-207_24	1.13E+06	16	690	280	19.27	0.54	108.6	27.2
AT-207_25	9.23E+05	24	Below LOD	0	12.98	0.48	131	26.8
AT-207_26	1.42E+06	22	610	240	27.16	0.41	96.5	20.6
AT-207_27	7.20E+05	21	Below LOD	0	13.47	0.46	98.6	21.6
AT-207_28	6.07E+05	10	610	180	8.25	0.27	135.3	42.8
AT-207_29	8.16E+05	17	450	170	11.68	0.29	128.9	31.3
AT-207_30	8.86E+05	13	620	150	12.01	0.26	135.6	37.6
AT-207_31	7.71E+05	16	340	220	18.88	0.35	75.4	18.9
AT-207_32	1.20E+06	53	810	300	19.08	0.66	115.4	16
AT-207_33	1.66E+06	43	510	180	35.15	0.49	87.6	13.4
AT-207_35	6.18E+05	30	600	270	9.23	0.24	123.2	22.6
AT-207_36	7.01E+05	30	550	290	14.5	0.38	89.3	16.3
AT-207_37	7.25E+05	23	580	180	14.21	0.31	94.3	19.7
AT-207_38	1.24E+06	16	620	150	18.14	0.28	126	31.5
AT-207_39	9.94E+05	20	810	360	20.42	0.56	90	20.2
AT-207_40	6.84E+05	20	520	290	11.7	0.29	108	24.2
Grain no.	**ρs (x105/cm2)**	**Ns**	**Cl (ppm)**	**Cl 2SE**	**U (ppm)**	**U238 2SE**	**t (Ma)**	**1σ (Ma)**
AT-238_1	4.61E+06	39	470	170	86	2.1	99.05	15.91
AT-238_4	1.50E+06	14	590	260	21.05	0.73	131.45	35.21
AT-238_6	4.75E+06	38	590	320	112.9	3.3	77.86	12.68
AT-238_7	5.46E+06	70	540	200	47	1.1	212.44	25.51
AT-238_14	3.24E+06	47	440	210	34.46	0.98	168.88	24.75
AT-238_16	1.85E+06	19	820	190	49.5	1.5	69.3	15.93
AT-238_23	2.57E+06	28	410	220	26.75	0.63	176.24	33.37
AT-238_24	3.13E+06	28	440	240	31.36	0.88	182.93	34.67
AT-238_28	2.78E+06	32	720	300	75.9	1.6	67.79	12.01
AT-238_29	5.30E+06	57	Below LOD	0	73.3	2.1	133.2	17.75
AT-238_30	2.62E+06	37	780	200	51.3	0.92	94.34	15.53
AT-238_33	1.93E+06	33	480	230	20.85	0.5	169.95	29.65
AT-238_34	2.16E+06	40	410	300	17.38	0.84	226.68	36.26
AT-238_35	4.41E+06	46	480	170	90	1.7	88.68	13.1
Grain no.	**ρs (x105/cm2)**	**Ns**	**Cl (ppm)**	**Cl 2SE**	**U (ppm)**	**U238 2SE**	**t (Ma)**	**1σ (Ma)**
AT-239_1	1.43E+06	43	530	130	22.3	0.44	117.8	18
AT-239_3	1.39E+06	21	480	230	32.99	0.96	77.8	17

AT-239_6	8.34E+05	11	380	260	17.98	0.46	85.8	25.9
AT-239_8	1.26E+06	22	320	200	22.53	0.89	103.5	22.2
AT-239_10	8.62E+05	34	580	170	23.64	0.47	67.5	11.6
AT-239_11	9.70E+05	19	360	290	25.38	0.68	70.7	16.2
AT-239_16	1.23E+06	42	670	280	22.21	0.43	102.5	15.8
AT-239_17	1.47E+06	27	Below LOD	0	23.29	0.6	116.2	22.4
AT-239_20	1.14E+06	51	330	170	21.92	0.49	96.1	13.5
AT-239_22	1.22E+06	32	Below LOD	0	25.48	0.68	88.7	15.7
AT-239_23	1.26E+06	17	390	150	23.82	0.41	97.3	23.6
AT-239_24	1.02E+06	39	530	240	21.37	0.54	88.4	14.2
AT-239_27	1.23E+06	**24**	530	330	**19.38**	**0.68**	**134.2**	**27.5**
AT-239_29	9.29E+05	30	360	210	18.13	0.31	94.6	17.3
AT-239_30	1.34E+06	44	Below LOD	0	25.15	0.82	98.5	14.9
AT-239_32	1.16E+06	34	Below LOD	0	22.55	0.33	95.1	16.3
AT-239_33	1.06E+06	24	620	220	25.22	0.57	77.6	15.9
AT-239_34	1.37E+06	38	600	290	22.57	0.69	112.1	18.3
AT-239_38	1.22E+06	32	540	230	19.64	0.49	114.7	20.3
AT-239_41	1.12E+06	29	650	280	20.56	0.59	100.1	18.6
Grain no.	**ρs (x105/cm2)**	**Ns**	**Cl (ppm)**	**Cl 2SE**	**U (ppm)**	**U238 2SE**	**t (Ma)**	**1σ (Ma)**
AT-240_1	1.84E+06	81	550	230	22.36	0.39	151.3	16.9
AT-240_3	2.24E+06	29	360	180	22.28	0.46	184.3	34.3
AT-240_4	2.22E+06	12	360	290	26.6	0.97	153.6	44.4
AT-240_5	1.79E+06	43	570	270	28.91	0.69	114.3	17.5
AT-240_6	1.94E+06	29	Below LOD	0	25.49	0.53	140.1	26.1
AT-240_7	1.44E+06	29	730	240	10.91	0.36	241.2	45
AT-240_8	1.01E+06	19	420	170	9.65	0.33	191.5	44
AT-240_9	1.66E+06	12	400	250	17.25	0.5	177	51.2
AT-240_10	1.46E+06	47	600	170	21.66	0.34	124	18.1
AT-240_11	2.19E+06	50	Below LOD	0	20.45	0.61	196.7	28
AT-240_15	2.13E+06	14	610	150	22.83	0.44	170.9	45.7
AT-240_16	2.26E+06	41	350	200	22.79	0.43	181.9	28.5
AT-240_17	2.25E+06	22	470	210	36.11	0.63	115	24.5
AT-240_18	1.35E+06	16	630	260	27.94	0.72	89	22.3
AT-240_19	1.07E+06	15	Below LOD	0	12.06	0.44	163.4	42.3
AT-240_20	1.79E+06	37	590	220	17.93	0.43	183.1	30.2
AT-240_22	2.14E+06	49	710	160	17.17	0.45	228	32.7
AT-240_23	2.52E+06	46	560	230	23.45	0.98	196.8	29.3
AT-240_24	1.64E+06	55	440	190	22.46	0.45	134.5	18.2
AT-240_25	2.04E+06	43	440	130	21.45	0.42	174.8	26.7
AT-240_28	1.41E+06	30	370	170	21.57	0.61	120.8	22.1
AT-240_29	2.45E+06	86	480	240	25.74	0.89	174.8	19.1
AT-240_30	1.59E+06	47	Below LOD	0	21.58	0.45	135.2	19.8
AT-240_32	1.50E+06	19	Below LOD	0	18.49	0.46	149	34.2
AT-240_33	1.94E+06	60	590	170	22.87	0.45	155.8	20.2
AT-240_34	1.55E+06	42	580	200	16.59	0.27	171	26.4
AT-240_35	1.82E+06	51	510	150	19.19	0.31	174.1	24.4

AT-240_36	1.62E+06	36	610	170	11.73	0.31	251.9	42.1
AT-240_37	2.42E+06	52	340	230	34.8	1.2	128	17.9
AT-240_38	1.57E+06	70	360	170	17.25	0.42	167.3	20.1
Grain no.	**ρs (x105/cm2)**	**Ns**	**Cl (ppm)**	**Cl 2SE**	**U (ppm)**	**U238 2SE**	**t (Ma)**	**1σ (Ma)**
AT-242_1	9.31E+05	15	3260	320	4.84	0.21	348.3	90.3
AT-242_2	7.18E+05	11	3980	440	10.98	0.34	120.5	36.4
AT-242_3	1.14E+06	9	3460	210	11.04	0.31	189.1	63.1
AT-242_4	9.33E+05	25	2490	280	5.24	0.26	323	65.1
AT-242_5	1.10E+06	13	2870	270	8.02	0.22	250.9	69.7
AT-242_6	1.84E+06	29	3550	560	10.81	0.37	308.2	57.5
AT-242_7	8.85E+05	17	3950	270	12.3	0.22	132.4	32.1
AT-242_8	4.47E+05	5	3030	440	6.24	0.24	131.8	59
AT-242_9	8.51E+05	15	3280	400	7.3	0.3	213.3	55.2
AT-242_10	1.31E+06	21	2380	240	7.37	0.36	322.3	70.8
AT-242_11	2.28E+06	29	2830	310	17.12	0.42	243.5	45.3
AT-242_13	8.39E+05	9	3290	370	6.59	0.19	232.6	77.6
AT-242_14	8.86E+05	10	2820	410	9.21	0.31	176.6	55.9
AT-242_15	2.96E+06	30	4830	510	24.6	1.1	220.4	40.5
AT-242_16	1.14E+06	21	3130	220	6.69	0.16	309.7	67.7
AT-242_19	5.71E+05	15	3150	220	6.6	0.18	159	41.1
AT-242_22	5.93E+05	10	4170	490	7.59	0.25	143.7	45.5
AT-242_23	8.56E+05	19	2740	510	7.81	0.44	200.8	46.4
AT-242_27	5.87E+05	9	3940	400	6.6	0.22	163.3	54.5
AT-242_28	5.69E+05	6	2280	270	3.93	0.17	264	107.9
AT-242_31	7.32E+05	10	2720	250	6.57	0.21	204	64.6
AT-242_38	1.20E+06	15	3590	300	12.01	0.28	183.9	47.5
AT-242_39	1.61E+06	21	4760	400	11.42	0.29	257.4	56.3
Grain no.	**ρs (x105/cm2)**	**Ns**	**Cl (ppm)**	**Cl 2SE**	**U (ppm)**	**U238 2SE**	**t (Ma)**	**1σ (Ma)**
AT-244_1	1.23E+06	60	860	220	13.43	0.29	165.6	21.5
AT-244_3	1.49E+06	42	950	180	15.24	0.3	179.2	27.7
AT-244_5	1.14E+06	100	1180	220	10.43	0.27	199.8	20.1
AT-244_8	8.84E+05	20	810	290	10.87	0.49	149.7	33.6
AT-244_10	2.01E+06	29	1660	220	16.41	0.37	124.7	23.2
AT-244_12	1.88E+06	25	1710	220	16.63	0.41	206.8	41.4
AT-244_13	1.46E+06	34	1010	180	17.51	0.33	153.2	26.3
AT-244_14	1.69E+06	32	1290	230	16.79	0.33	184.4	32.6
AT-244_22	1.50E+06	83	1280	190	16.78	0.4	125.1	13.8
AT-244_23	1.42E+06	44	1660	170	14.26	0.32	181.9	27.5
AT-244_25	1.56E+06	88	880	180	17.07	0.37	167.4	17.9
AT-244_26	6.38E+05	42	1250	260	5.84	0.14	241.1	37.3
AT-244_27	1.52E+06	35	1010	380	12.59	0.32	221.1	37.5
AT-244_31	1.52E+06	45	900	180	16.1	0.33	173.6	25.9
AT-244_34	1.61E+06	86	1650	230	14.89	0.34	198.3	21.5
AT-244_36	1.01E+06	53	830	190	7.65	0.24	258.6	35.8
AT-244_38	1.83E+06	28	730	170	21.22	0.65	158.9	30.1
AT-244_39	1.17E+06	33	930	160	12.78	0.27	168	29.3

Grain no.	ρs (x105/cm2)	Ns	Cl (ppm)	Cl 2SE	U (ppm)	U238 2SE	t (Ma)	1σ (Ma)
AT-245_1	1.07E+06	19	400	190	15.9	0.44	124.3	28.6
AT-245_2	1.74E+06	20	440	220	18.2	1.2	175.1	39.6
AT-245_4	2.17E+05	5	Below LOD	0	2.58	0.1	154.7	69.2
Grain no.	**ρs (x105/cm2)**	**Ns**	**Cl (ppm)**	**Cl 2SE**	**U (ppm)**	**U238 2SE**	**t (Ma)**	**1σ (Ma)**
AT-246_1	7.65E+05	20	1430	250	3.36	0.16	410	92.2
AT-246_2	2.59E+06	73	570	210	35.15	0.69	113.1	13.3
AT-246_3	1.10E+06	42	500	200	8.81	0.37	363.5	56.6
AT-246_5	1.77E+06	44	650	160	23.3	0.75	139.9	21.2
AT-246_6	1.20E+06	37	390	160	13.91	0.29	159.1	26.2
AT-246_7	8.35E+05	22	630	200	10	0.35	153.4	32.8
AT-246_13	1.85E+06	46	480	160	15.71	0.27	215.5	31.8
AT-246_14	1.25E+06	17	420	210	10.7	0.7	214.2	52.4
AT-246_15	1.62E+06	34	370	290	13.04	0.41	227.6	39.2
AT-246_16	1.18E+06	29	540	170	5.82	0.27	457.6	85.6
AT-246_17	1.58E+06	30	540	180	10.57	0.29	271.7	49.7
AT-246_18	1.73E+06	19	570	170	25.03	0.68	101.8	23.4
AT-246_19	1.20E+06	22	480	140	9.53	0.26	230.8	49.3
AT-246_20	1.40E+06	33	650	180	15.03	0.35	170.4	29.7
AT-246_21	1.81E+06	40	700	200	24.49	0.61	136.3	21.6
AT-246_22	1.68E+06	40	630	250	20.22	0.57	152.4	24.2
AT-246_23	9.80E+05	27	720	260	11.62	0.4	155.1	30
AT-246_25	1.84E+06	50	710	190	21.55	0.43	156.7	22.2
AT-246_27	8.71E+05	27	510	110	11.96	0.27	134.1	25.9
AT-246_30	6.69E+05	8	770	170	4.45	0.13	273.8	96.9
AT-246_31	1.10E+06	22	670	220	14.48	0.28	139.7	29.8
AT-246_32	9.89E+05	9	610	170	8.91	0.16	203.3	67.8
AT-246_34	7.85E+05	11	620	230	11.26	0.26	128.4	38.7
AT-246_36	1.33E+06	40	630	160	16.33	0.77	149.6	23.9
AT-246_39	8.70E+05	28	780	200	8.5	0.16	187.6	35.5
AT-246_40	2.18E+06	19	450	230	15.93	0.46	108.1	24.8
Grain no.	**ρs (x105/cm2)**	**Ns**	**Cl (ppm)**	**Cl 2SE**	**U (ppm)**	**U238 2SE**	**t (Ma)**	**1σ (Ma)**
AT-248_3	3.29E+06	41	1010	250	44.4	0.94	136.5	21.4
AT-248_4	1.41E+06	24	1230	320	15.98	0.5	162	33.2
AT-248_5	1.18E+06	14	800	270	16.22	0.44	133.6	35.7
AT-248_8	1.33E+06	35	1030	240	14.03	0.41	174.6	29.6
AT-248_10	1.21E+06	24	1410	220	19.73	0.36	113.1	23.1
AT-248_13	1.07E+06	24	1410	310	12.35	0.38	158.4	32.4
AT-248_16	8.21E+05	10	1180	180	9.05	0.21	166.6	52.7
AT-248_21	8.96E+05	19	1600	310	6.14	0.28	265.8	61.3
AT-248_22	8.47E+05	11	1380	240	8.99	0.3	172.9	52.2
AT-248_23	8.79E+05	17	1380	280	8.14	0.3	197.8	48.1
AT-248_24	6.88E+05	12	1620	240	7.55	0.15	167.4	48.3
AT-248_25	1.05E+06	18	1050	190	18.78	0.57	103.6	24.5
AT-248_26	9.79E+05	13	2180	350	17.43	0.4	103.7	28.8
AT-248_29	6.44E+05	17	1230	210	7.18	0.23	164.8	40.1

AT-248_33	9.05E+05	12	1100	260	8.69	0.3	190.9	55.2
AT-248_35	4.54E+05	5	850	200	8.77	0.34	95.6	42.8
AT-248_39	7.75E+05	16	1200	260	9.26	0.31	153.8	38.5
AT-248_40	1.47E+06	29	1200	190	13.49	0.34	199	37
Grain no.	**ρs (x105/cm2)**	**Ns**	**Cl (ppm)**	**Cl 2SE**	**U (ppm)**	**U238 2SE**	**t (Ma)**	**1σ (Ma)**
AT-252_2	1.99E+06	83	620	190	57.8	1.4	63.6	7.02
AT-252_7	1.93E+06	81	980	260	50.59	0.76	70.71	7.87
AT-252_8	2.05E+06	73	890	240	38.38	0.73	98.65	11.58
AT-252_9	2.46E+06	117	870	210	52.28	0.85	86.89	8.06
AT-252_10	2.51E+06	27	700	230	45.9	1.5	100.55	19.42
AT-252_11	3.05E+06	45	660	180	44.5	0.77	125.89	18.8
AT-252_12	1.54E+06	88	870	180	45.75	0.81	62.37	6.67
AT-252_13	2.57E+06	70	1020	150	38.99	0.57	121.65	14.57
AT-252_16	1.58E+06	23	730	270	66.6	2	44.16	9.23
AT-252_17	2.37E+06	57	1120	300	44.84	0.92	97.4	12.94
AT-252_18	2.41E+06	76	1160	270	22.43	0.8	197.09	22.88
AT-252_19	2.13E+06	128	850	270	52.3	1.6	75.08	6.73
AT-252_20	1.95E+06	65	1010	270	29.25	0.77	122.98	15.34
AT-252_21	2.03E+06	52	870	330	52.3	1.8	71.86	10.04
AT-252_22	1.57E+06	61	830	200	55.1	1.3	52.87	6.8
AT-252_23	2.93E+06	66	880	200	54.89	0.88	98.67	12.17
AT-252_24	2.90E+06	75	1070	140	60.7	1.2	88.15	10.22
AT-252_26	1.31E+06	43	890	160	47.73	0.81	50.9	7.77
AT-252_29	1.61E+06	91	870	180	39.99	0.68	74.24	7.81
AT-252_32	2.05E+06	73	830	250	38.19	0.87	99.13	11.66
AT-252_33	2.38E+06	86	710	330	44.4	1.2	99.06	10.77
AT-252_34	1.96E+06	149	990	150	51.43	0.65	70.35	5.78
AT-252_35	2.86E+06	99	900	220	44.8	1.1	117.41	11.89
AT-252_41	1.39E+06	56	960	300	16.76	0.69	152.44	20.61
Grain no.	**ρs (x105/cm2)**	**Ns**	**Cl (ppm)**	**Cl 2SE**	**U (ppm)**	**U238 2SE**	**t (Ma)**	**1σ (Ma)**
AT-253_1	6.64E+05	40	360	160	10.34	0.24	118.4	18.8
AT-253_2	1.42E+06	12	370	130	24.56	0.78	106.7	30.8
AT-253_3	1.01E+06	17	620	200	13.76	0.39	135.3	32.9
AT-253_5	7.80E+05	18	440	130	13.69	0.21	105.1	24.8
AT-253_6	1.45E+06	16	410	150	13.66	0.29	194.3	48.6
AT-253_7	8.49E+05	21	Below LOD	0	9.83	0.37	158.8	34.8
AT-253_8	1.21E+06	26	390	140	11.75	0.23	188.5	37
AT-253_10	1.18E+06	14	500	150	10.19	0.22	212.5	56.8
AT-253_11	1.18E+06	18	370	150	9.75	0.22	221.5	52.3
AT-253_13	1.04E+06	22	440	130	10.68	0.27	178.7	38.2
AT-253_14	6.69E+05	11	340	150	10.68	0.21	115.5	34.8
AT-253_16	8.97E+05	13	250	150	10.39	0.19	158.7	44
AT-253_18	8.28E+05	32	300	120	12.15	0.26	125.6	22.2
AT-253_20	8.36E+05	21	250	150	11.92	0.2	129.2	28.2
AT-253_21	1.18E+06	15	310	150	11.26	0.23	192.6	49.8
AT-253_23	1.29E+06	12	290	140	9.99	0.2	236.3	68.3

AT-253_26	1.70E+06	49	400	140	14.04	0.43	220.7	31.7
AT-253_29	5.58E+05	30	Below LOD	0	11.37	0.26	90.6	16.6
AT-253_30	7.68E+05	14	Below LOD	0	12.22	0.35	115.9	31
AT-253_31	1.35E+06	24	330	110	11.85	0.26	208.2	42.6
AT-253_33	1.09E+06	19	460	170	12.24	0.32	163.1	37.5
AT-253_35	1.00E+06	18	320	160	15	0.4	123.2	29.1
AT-253_36	6.15E+05	19	370	150	12.19	0.23	93.2	21.4
AT-253_39	5.58E+05	14	Below LOD	0	11.71	0.21	88	23.5
AT-253_40	1.60E+06	22	280	150	12.05	0.4	241.9	51.7

Grain no.	ρs (x105/cm2)	Ns	Cl (ppm)	Cl 2SE	U (ppm)	U238 2SE	t (Ma)	1σ (Ma)
AT-254_2	2.17E+06	62	660	150	30.52	0.76	176.27	22.49
AT-254_3	2.79E+06	45	920	160	63.1	1.1	81.64	12.19
AT-254_4	2.74E+06	181	1110	240	49.3	1.2	102.41	7.71
AT-254_5	2.53E+06	103	720	190	40.94	0.62	113.91	11.26
AT-254_7	2.69E+06	68	660	170	66.7	0.99	66.66	8.1
AT-254_8	2.63E+06	42	1130	180	67.3	1.3	72.25	11.17
AT-254_9	2.93E+06	35	870	180	54.66	0.98	99.01	16.76
AT-254_10	2.25E+06	23	740	140	40.44	0.81	102.72	21.44
AT-254_11	2.56E+06	64	660	170	48.57	0.89	97.25	12.19
AT-254_12	2.27E+06	29	1010	270	40.02	0.87	104.48	19.43
AT-254_13	3.10E+06	102	1100	210	65.1	1.1	88.06	8.75
AT-254_14	2.91E+06	44	1210	280	34.34	0.75	155.77	23.54
AT-254_15	2.72E+06	27	920	240	53.03	0.91	94.82	18.27
AT-254_17	2.11E+06	48	1090	210	39.65	0.8	98.34	14.23
AT-254_18	3.37E+06	48	600	210	51.8	1.1	119.78	17.34
AT-254_19	1.71E+06	31	760	220	47.33	0.84	66.94	12.04
AT-254_21	2.08E+06	72	820	170	41.47	0.75	92.48	10.93
AT-254_23	1.73E+06	23	1060	190	45.67	0.87	70.07	14.63
AT-254_24	2.09E+06	58	650	250	43.5	1.1	87.16	11.5
AT-254_25	2.50E+06	83	650	140	39.74	0.62	116.03	12.77
AT-254_26	2.00E+06	94	640	200	55	1	67.33	6.97
AT-254_27	3.28E+06	82	720	220	51.2	1.6	118.15	13.18
AT-254_28	1.59E+06	79	710	180	35.19	0.42	83.4	9.4
AT-254_29	2.77E+06	54	1400	170	67.2	1.1	76.22	10.39
AT-254_30	2.75E+06	94	1110	300	76.8	1.8	66.19	6.87
AT-254_31	2.40E+06	62	630	200	41.1	0.92	107.75	13.74
AT-254_35	2.42E+06	76	710	160	37.04	0.9	120.45	13.89
AT-254_36	2.76E+06	39	760	270	53.4	1.4	95.46	15.34
AT-254_37	2.69E+06	59	840	280	77.3	3.5	64.46	8.52
AT-254_38	1.28E+06	20	1600	190	15.83	0.29	148.39	33.21
AT-254_39	2.33E+06	51	670	180	48.24	0.96	89.4	12.55

Grain no.	ρs (x105/cm2)	Ns	Cl (ppm)	Cl 2SE	U (ppm)	U238 2SE	t (Ma)	1σ (Ma)
AT-255_4	7.79E+05	7	930	190	4.19	0.15	144.44	54.65
AT-255_5	3.32E+05	8	1100	220	6.12	0.22	100.09	35.43
AT-255_7	2.53E+05	11	1320	170	5.51	0.16	84.92	25.64

11. APPENDIX C: AU-PB DATA TABLE

Table 6 – Single AU-Pb data from individual grains analysed in this study, calculated using the Iolite software (Paton et al. 2011). Final 238/206 and 207/206 represent the ratios with 2σ representing the standard error. The error correlation represents the correlation of standard error between the two ratio sets. Final 207 age represents the common-Pb corrected Au-Pb ages with 2σ as the standard error.

Grain no.	Final 238/206	2σ	Final 207/206	2σ	Error Correlation 238/206 vs 207/206	Final 207 Age (Ma)	2σ (Ma)
AT-202 - 1.d	9.727626459	0.406895	0.2253	0.0073	0.40002	499	31
AT-202 - 2.d	9.643201543	0.418461	0.3125	0.0098	0.37984	436	29
AT-202 - 3.d	10.13171226	0.431137	0.244	0.0075	-0.27416	467.1	21
AT-202 - 4.d	10.22494888	0.418198	0.2481	0.0082	0.22889	460.1	29
AT-202 - 5.d	10.26694045	0.411099	0.1987	0.0071	0.40846	495.5	32
AT-202 - 6.d	10.47120419	0.42762	0.2419	0.0078	0.4152	454	29
AT-202 - 7.d	10.42752868	0.42406	0.2493	0.0076	0.58134	449	33
AT-202 - 8.d	10.26694045	0.42164	0.2282	0.0074	0.29141	473	28
AT-202 - 9.d	9.910802775	0.412541	0.227	0.011	-0.0031015	490	27
AT-202 - 10.d	10.44932079	0.425834	0.2304	0.0056	0.33441	463.6	26
AT-202 - 11.d	9.496676163	0.41486	0.2948	0.0085	0.19371	456	27
AT-202 - 12.d	11.26126126	0.469219	0.2066	0.0064	-0.030823	446.7	20
AT-202 - 13.d	10.16260163	0.423442	0.2661	0.0092	0.37716	449	30
AT-202 - 14.d	8.650519031	0.359191	0.343	0.013	0.49433	460	38
AT-202 - 16.d	9.337068161	0.479495	0.327	0.015	0.31884	438	32
AT-202 - 17.d	10.79913607	0.501472	0.2203	0.0072	0.12799	456	23
AT-202 - 18.d	11.16071429	0.448422	0.1922	0.0049	0.16252	460.9	23
AT-202 - 19.d	10.35196687	0.450086	0.2497	0.009	0.31283	453	27
AT-202 - 22.d	9.727626459	0.454208	0.274	0.012	-0.079507	462	27
AT-202 - 25.d	10.5374078	0.466355	0.2371	0.0083	0.34747	455	27
AT-202 - 27.d	10.77586207	0.429641	0.195	0.0051	0.43318	475.1	26

AT-202 - 28.d	10.43841336	0.424946	0.2306	0.0072	0.42864	464	28
AT-202 - 29.d	9.149130833	0.426904	0.309	0.015	0.23332	461	35
AT-202 - 30.d	10.63829787	0.441376	0.2193	0.007	0.14812	463.5	24
AT-202 - 31.d	9.56937799	0.402921	0.312	0.011	0.16781	439	30
AT-202 - 32.d	9.910802775	0.412541	0.2755	0.0087	0.40477	451	32
AT-202 - 33.d	11.57407407	0.468857	0.1773	0.0057	0.27506	454.8	25
AT-202 - 34.d	8.503401361	0.397693	0.344	0.014	0.45644	464	36
AT-202 - 35.d	10.49317943	0.495481	0.2514	0.0088	0.27651	443	27
Grain	Final 238/206	2σ	Final 207/206	2σ	Error Correlation 238/206 vs 207/206	Final 207 Age (Ma)	2σ (Ma)
AT-203 - 1.d	3.795066414	0.158428	0.66	0.022	0.62598	283	85
AT-203 - 2.d	5.991611744	0.233346	0.3221	0.0089	0.37804	647	39
AT-203 - 3.d	3.514938489	0.185322	0.43	0.015	0.27072	845	89
AT-203 - 4.d	5.310674456	0.208704	0.545	0.016	0.60988	383	65
AT-203 - 5.d	4.145936982	0.223454	0.461	0.015	0.19389	656	75
AT-203 - 6.d	2.538071066	0.135278	0.7	0.021	0.42126	249	120
AT-203 - 7.d	5.753739931	0.311192	0.473	0.019	-0.013989	458	56
AT-203 - 8.d	7.153075823	0.271182	0.2765	0.0078	0.39358	601	40
AT-203 - 9.d	10.27749229	0.686575	0.258	0.023	0.062843	437	28
AT-203 - 10.d	7.251631617	0.310258	0.423	0.015	0.62246	425	51
AT-203 - 12.d	6.729475101	0.321529	0.429	0.014	0.4977	450	56
AT-203 - 13.d	9.208103131	0.932681	0.313	0.026	-0.31076	434	27
AT-203 - 14.d	6.973500697	0.286915	0.458	0.014	0.17707	397	37
AT-203 - 15.d	5.263157895	0.304709	0.481	0.019	0.33654	469	46
AT-203 - 16.d	8.23723229	0.373186	0.3076	0.01	0.063844	489	27
AT-203 - 17.d	5.162622612	0.231878	0.454	0.011	0.34112	541	46

AT-203 - 18.d	4.69043152	0.396003	0.461	0.014	0.25836	581	57
AT-203 - 19.d	6.37755102	0.650771	0.414	0.014	0.48307	494	58
AT-203 - 20.d	5.646527386	0.299703	0.434	0.012	0.14423	525	56
AT-203 - 21.d	8.176614881	0.595028	0.371	0.018	0.074282	430	38
AT-203 - 25.d	6.337135615	0.401593	0.374	0.013	0.32356	537	36
AT-203 - 27.d	6.238303182	0.28409	0.487	0.017	0.44255	406	46
AT-203 - 28.d	3.086419753	0.19052	0.634	0.023	0.50413	418	110
AT-203 - 29.d	5.571030641	0.23898	0.343	0.0095	-0.037848	660	29

Grain	Final 238/206	2σ	Final 207/206	2σ	Error Correlation 238/206 vs 207/206	Final 207 Age (Ma)	2σ (Ma)
AT_205 - 1.d	9.099181074	0.33118	0.324	0.0079	0.44304	455	29
AT_205 - 2.d	9.017132552	0.398413	0.3534	0.0076	0.25811	432	26
AT_205 - 3.d	8.347245409	0.313544	0.3726	0.0083	0.015839	451	25
AT_205 - 4.d	8.34028357	0.313022	0.3782	0.011	0.29693	449	32
AT_205 - 5.d	8.710801394	0.318688	0.339	0.0098	0.33369	463	39
AT_205 - 6.d	8.976660682	0.33038	0.3718	0.007	0.49349	421	31
AT_205 - 7.d	7.457121551	0.316969	0.423	0.0094	0.45538	453	39
AT_205 - 8.d	7.412898443	0.604462	0.41	0.019	0.33773	469	40
AT_205 - 9.d	8.34028357	0.319978	0.3713	0.008	0.39863	453	27
AT_205 - 10.d	7.593014427	0.294035	0.436	0.0097	0.469	432	33
AT_205 - 11.d	7.824726135	0.300009	0.411	0.011	0.61386	444	47
AT_205 - 12.d	8.038585209	0.368328	0.413	0.013	0.50117	431	33
AT_205 - 13.d	8.389261745	0.316709	0.3777	0.0082	0.44511	444	28
AT_205 - 14.d	7.451564829	0.34426	0.435	0.013	0.40511	441	42
AT_205 - 15.d	7.745933385	0.719994	0.413	0.013	-0.032175	445	25
AT_205 - 16.d	8.453085376	0.321546	0.381	0.01	0.096459	437	25

AT_205 - 17.d	4.859086492	0.203052	0.583	0.014	0.49565	441	50
AT_205 - 18.d	7.627765065	0.290914	0.432	0.012	0.37406	432	40
AT_205 - 19.d	9.689922481	0.366189	0.3107	0.007	0.35124	438	24
Grain	Final 238/206	2σ	Final 207/206	2σ	Error Correlation 238/206 vs 207/206	Final 207 Age (Ma)	2σ (Ma)
AT-206 - 3.d	4.914004914	0.386359	0.566	0.024	0.64148	438	57
AT-206 - 4.d	7.062146893	0.294256	0.453	0.011	-0.090418	432	29
AT-206 - 5.d	5.834305718	0.224658	0.51	0.014	0.66533	447	51
AT-206 - 8.d	6.570302234	0.690702	0.489	0.016	-0.11161	420	34
AT-206 - 10.d	3.663003663	0.161011	0.674	0.025	0.47316	355	110
AT-206 - 11.d	9.398496241	0.36216	0.3279	0.0062	0.0082464	429.7	20
AT-206 - 15.d	4.789272031	0.215609	0.558	0.014	0.38364	462	72
AT-206 - 17.d	8.051529791	0.842753	0.391	0.016	-0.2103	434	18
Grain	Final 238/206	2σ	Final 207/206	2σ	Error Correlation 238/206 vs 207/206	Final 207 Age (Ma)	2σ (Ma)
AT-207 - 1.d	4.56412597	0.204146	0.589	0.016	0.01635	604	57
AT-207 - 2.d	4.450378282	0.178253	0.394	0.011	0.30146	884	53
AT-207 - 3.d	3.909304144	0.198675	0.546	0.019	0.41254	773	66
AT-207 - 4.d	5.521811154	0.237825	0.319	0.014	0.061191	805	44
AT-207 - 5.d	5.763688761	0.225897	0.306	0.0078	0.35949	791	42
AT-207 - 6.d	5.002501251	0.2002	0.3041	0.0081	0.31972	904	44
AT-207 - 7.d	5.073566717	0.211077	0.3036	0.0082	0.18273	892	42
AT-207 - 9.d	5.293806247	0.21859	0.529	0.016	0.4667	595	50
AT-207 - 10.d	4.512635379	0.193457	0.359	0.011	-0.16818	923	48
AT-207 - 11.d	5.420054201	0.208577	0.3041	0.0087	0.37246	837	43
AT-207 - 12.d	4.301075269	0.184993	0.387	0.015	-0.30876	925	42
AT-207 - 13.d	4.705882353	0.221453	0.369	0.01	0.17683	874	50

AT-207 - 14.d	4.8828125	0.200272	0.2319	0.01	0.076546	1014	48
AT-207 - 15.d	4.108463435	0.168795	0.354	0.011	0.53697	1021	67
AT-207 - 16.d	4.338394794	0.178806	0.382	0.011	0.40567	929	54
AT-207 - 17.d	4.07000407	0.182214	0.495	0.014	0.42588	818	67
AT-207 - 19.d	3.984063745	0.222219	0.393	0.017	0.36164	991	73
AT-207 - 20.d	4.486316734	0.197245	0.507	0.015	0.25856	729	59
AT-207 - 21.d	4.543389368	0.206424	0.344	0.013	0.2145	939	58
AT-207 - 22.d	4.775549188	0.212095	0.4389	0.0097	0.11982	773	40
AT-207 - 23.d	5.224660397	0.300268	0.373	0.015	-0.28479	785	40
AT-207 - 24.d	4.205214466	0.194522	0.381	0.015	0.22703	957	65
AT-207 - 25.d	6.464124111	0.238174	0.3619	0.0097	0.32161	651	38
AT-207 - 26.d	5.175983437	0.235759	0.532	0.02	0.52233	606	53
AT-207 - 27.d	3.985651654	0.17474	0.587	0.015	0.48299	693	69
AT-207 - 28.d	4.382120947	0.176668	0.479	0.013	0.31502	784	53
AT-207 - 29.d	4.353504571	0.178158	0.48	0.014	0.48931	788	56
AT-207 - 30.d	5.28262018	0.267898	0.386	0.011	0.038551	762	40
AT-207 - 31.d	4.854368932	0.306344	0.364	0.012	0.24673	856	59
AT-207 - 32.d	6.811989101	0.250577	0.297	0.0076	0.25796	677	34
AT-207 - 33.d	4.214075011	0.177584	0.553	0.018	0.39539	707	63
AT-207 - 34.d	5.277044855	0.233917	0.515	0.016	0.29936	613	46
AT-207 - 35.d	6.116207951	0.265597	0.482	0.017	0.052579	564	44
AT-207 - 36.d	4.748338082	0.184883	0.348	0.0094	0.43978	895	52
AT-207 - 37.d	5.205622072	0.203239	0.3735	0.0094	0.58225	789	48
AT-207 - 38.d	4.490345757	0.189534	0.374	0.014	0.37908	908	61
Grain	Final 238/206	2σ	Final 207/206	2σ	Error Correlation 238/206 vs 207/206	Final 207 Age (Ma)	2σ (Ma)

AT-238 - 1.d	6.285355123	0.252836	0.1616	0.0036	0.44031	782	45
AT-238 - 2.d	4.935834156	0.219262	0.301	0.01	0.19651	660	63
AT-238 - 3.d	7.390983001	0.305909	0.1407	0.0045	0.15572	699	37
AT-238 - 4.d	5.763688761	0.239185	0.2057	0.0049	0.46423	761	50
AT-238 - 6.d	6.501950585	0.279017	0.2661	0.0088	0.091356	565	44
AT-238 - 7.d	5.621135469	0.233819	0.2172	0.0075	0.0096294	755	51
AT-238 - 8.d	3.916960439	0.184111	0.394	0.017	0.22158	548	97
AT-238 - 9.d	5.636978579	0.231961	0.2418	0.0065	0.15222	702	51
AT-238 - 10.d	7.867820614	0.321894	0.1299	0.0029	-0.29475	676	30
AT-238 - 12.d	6.858710562	0.315181	0.341	0.013	0.30628	407	49
AT-238 - 13.d	8.984725966	0.387481	0.346	0.011	0.14444	304	36
AT-238 - 14.d	7.342143906	0.312661	0.1715	0.0054	0.35881	655	40
AT-238 - 15.d	8.992805755	0.363918	0.2053	0.0046	0.16404	491.2	29
AT-238 - 16.d	5.675368899	0.235132	0.2099	0.0044	0.37399	760	50
AT-238 - 17.d	6.176652254	0.259427	0.1902	0.0077	0.42267	746	42
AT-238 - 18.d	4.587155963	0.21042	0.31	0.017	0.094717	684	84
AT-238 - 20.d	7.4019245	0.306816	0.156	0.0038	0.29614	674	36

Grain	Final 238/206	2σ	Final 207/206	2σ	Error Correlation 238/206 vs 207/206	Final 207 Age (Ma)	2σ (Ma)
AT-239 - 1.d	7.818608288	0.360671	0.441	0.015	0.30414	409	37
AT-239 - 2.d	6.523157208	0.331902	0.489	0.015	-0.027514	431	36
AT-239 - 3.d	7.256894049	0.315975	0.466	0.015	0.3012	416	46
AT-239 - 4.d	5.285412262	0.234659	0.549	0.013	0.32498	439	51
AT-239 - 5.d	7.704160247	0.350189	0.438	0.011	0.43258	418	34
AT-239 - 6.d	7.552870091	0.319457	0.423	0.012	0.34968	444	42
AT-239 - 7.d	6.849315068	0.28617	0.458	0.012	0.18857	447	43

AT-239 - 8.d	7.993605116	0.345048	0.424	0.013	0.466	414	36
AT-239 - 9.d	7.412898443	0.318716	0.456	0.01	0.44678	416	34
AT-239 - 10.d	7.457121551	0.316969	0.434	0.016	0.51451	439	50
AT-239 - 11.d	6.430868167	0.297764	0.485	0.012	0.31947	442	37
AT-239 - 12.d	7.745933385	0.359997	0.394	0.01	0.29517	455	28
AT-239 - 13.d	7.158196135	0.307439	0.46	0.011	0.20272	426	36
AT-239 - 14.d	7.710100231	0.344785	0.429	0.015	0.41669	428	40
AT-239 - 15.d	7.037297678	0.297141	0.463	0.013	0.52504	429	45
AT-239 - 16.d	5.115089514	0.214546	0.582	0.018	0.43263	410	76
AT-239 - 17.d	7.552870091	0.370798	0.445	0.014	0.74826	420	38
AT-239 - 18.d	7.032348805	0.351123	0.505	0.029	0.17662	383	58
AT-239 - 19.d	6.693440428	0.286734	0.485	0.012	0.18196	421	42
AT-239 - 20.d	6.76132522	0.292579	0.479	0.013	0.36092	429	43
AT-239 - 21.d	7.48502994	0.369769	0.433	0.015	0.40054	435	39
AT-239 - 22.d	6.234413965	0.268189	0.511	0.011	-0.03464	423	35
AT-239 - 23.d	6.527415144	0.29825	0.485	0.017	0.57308	437	52
AT-239 - 24.d	7.604562738	0.346976	0.448	0.016	0.47077	414	42
Grain	**Final 238/206**	**2σ**	**Final 207/206**	**2σ**	**Error Correlation 238/206 vs 207/206**	**Final 207 Age (Ma)**	**2σ (Ma)**
AT-240 - 1.d	7.178750897	0.2989	0.463	0.011	0.38693	431	40
AT-240 - 3.d	6.844626968	0.290463	0.471	0.014	0.13715	440	42
AT-240 - 4.d	7.407407407	0.373114	0.45	0.019	-0.027774	430	37
AT-240 - 5.d	7.587253414	0.339642	0.4424	0.0092	0.55821	429	32
AT-240 - 6.d	7.183908046	0.325134	0.466	0.014	0.30778	428	39
AT-240 - 7.d	4.323389537	0.205609	0.627	0.022	0.31013	424	72
AT-240 - 9.d	6.176652254	0.270872	0.513	0.016	0.52768	440	52

AT-240 - 10.d	7.513148009	0.338684	0.454	0.017	0.60899	426	51
AT-240 - 11.d	6.640106242	0.34391	0.501	0.017	0.70422	417	50
AT-240 - 12.d	7.304601899	0.330815	0.458	0.013	0.36337	429	36
AT-240 - 13.d	7.651109411	0.333675	0.434	0.0099	0.15237	432	29
AT-240 - 14.d	6.802721088	0.296173	0.483	0.012	0.43034	429	43
AT-240 - 15.d	8.37520938	0.343706	0.409	0.01	0.22312	419	34
AT-240 - 16.d	7.751937984	0.336518	0.434	0.012	0.36557	428	36
AT-240 - 18.d	6.653359947	0.29659	0.494	0.015	0.33781	429	43
AT-240 - 19.d	6.802721088	0.305428	0.487	0.015	0.24183	431	42
AT-240 - 20.d	6.872852234	0.3401	0.48	0.019	0.66801	433	49
AT-240 - 21.d	8.130081301	0.423029	0.425	0.016	-0.028849	416	30
AT-240 - 22.d	6.640106242	0.29541	0.49	0.014	0.52288	436	44
AT-240 - 23.d	6.734006734	0.272081	0.489	0.014	0.28492	430	54
AT-240 - 25.d	6.644518272	0.304632	0.504	0.015	0.24647	419	41
AT-240 - 26.d	7.446016381	0.338203	0.472	0.015	0.26345	407	37
AT-240 - 27.d	6.738544474	0.290611	0.493	0.015	0.49456	425	49
AT-240 - 28.d	6.896551724	0.3044	0.487	0.015	0.49348	423	45
AT-240 - 29.d	6.954102921	0.294993	0.49	0.012	0.32606	415	40
AT-240 - 30.d	5.640157924	0.254491	0.545	0.013	0.3263	433	46
AT-240 - 31.d	6.527415144	0.281207	0.511	0.013	0.55502	418	45
AT-240 - 32.d	4.828585225	0.223826	0.592	0.025	0.37249	435	78
AT-240 - 33.d	8.481764207	0.366896	0.394	0.011	0.35955	428	33

Grain	Final 238/206	2σ	Final 207/206	2σ	Error Correlation 238/206 vs 207/206	Final 207 Age (Ma)	2σ (Ma)
AT-242 - 1.d	6.418485237	0.337815	0.628	0.045	0.43251	264	86
AT-242 - 2.d	9.727626459	0.454208	0.529	0.023	0.15497	257	38

AT-242 - 3.d	9.532888465	0.49073	0.512	0.027	0.41627	277	41
AT-242 - 4.d	6.756756757	0.429145	0.619	0.044	0.27866	261	73
AT-242 - 5.d	9.68054211	0.459193	0.546	0.028	0.42433	245	45
AT-242 - 6.d	10.78748652	0.570212	0.483	0.025	0.43836	267	36
AT-242 - 7.d	10.98901099	0.495109	0.489	0.02	0.38207	258	35
AT-242 - 8.d	7.027406887	0.400014	0.616	0.031	0.35434	240	55
AT-242 - 9.d	9.689922481	0.666652	0.515	0.041	0.26662	269	47
AT-242 - 10.d	9.250693802	0.470664	0.552	0.025	0.44892	250	39
AT-242 - 11.d	15.3609831	0.731475	0.339	0.018	0.23167	261	22
AT-242 - 12.d	8.756567426	0.452397	0.561	0.029	0.42638	257	45
AT-242 - 13.d	12.53132832	0.69095	0.43	0.03	0.24699	263	34
AT-242 - 14.d	14.83679525	0.726431	0.373	0.017	-0.10528	252	18
AT-242 - 15.d	7.220216606	0.390987	0.623	0.04	0.52976	247	71
AT-242 - 16.d	7.407407407	0.471879	0.619	0.048	0.63367	247	73
AT-242 - 17.d	7.716049383	0.357225	0.591	0.019	0.31846	249	40
AT-242 - 18.d	7.955449483	0.601247	0.553	0.045	0.3178	291	60
AT-242 - 19.d	7.44047619	0.376453	0.602	0.027	0.63715	250	54
AT-242 - 20.d	6.064281383	0.404531	0.621	0.035	0.37942	293	63
AT-242 - 21.d	7.390983001	0.365998	0.634	0.033	0.38085	217	57
AT-242 - 23.d	11.16071429	0.585439	0.513	0.025	0.27563	236	32
AT-242 - 24.d	7.836990596	0.393078	0.577	0.021	0.34954	270	42
AT-242 - 25.d	8.52514919	0.479676	0.538	0.025	0.22564	284	39

Grain	Final 238/206	2σ	Final 207/206	2σ	Error Correlation 238/206 vs 207/206	Final 207 Age (Ma)	2σ (Ma)
AT-244 - 1.d	7.575757576	0.350092	0.559	0.017	0.40489	311	39
AT-244 - 2.d	8.130081301	0.36354	0.549	0.018	0.40208	300	39

AT-244 - 3.d	12.83697047	0.609715	0.332	0.016	0.031639	317	21
AT-244 - 4.d	6.393861893	0.28617	0.606	0.018	-0.049602	309	44
AT-244 - 5.d	7.412898443	0.335202	0.554	0.02	0.15413	324	46
AT-244 - 6.d	7.62195122	0.331137	0.527	0.015	0.26841	340	38
AT-244 - 7.d	8.488964346	0.410756	0.52	0.018	0.48599	308	34
AT-244 - 8.d	8.880994671	0.386473	0.483	0.016	0.40674	331	37
AT-244 - 9.d	8.741258741	0.404971	0.499	0.017	0.44977	323	35
AT-244 - 11.d	4.444444444	0.25679	0.678	0.032	-0.079974	316	72
AT-244 - 12.d	7.800312012	0.3529	0.519	0.016	0.29286	343	38
AT-244 - 13.d	7.293946025	0.32453	0.539	0.02	0.40288	344	49
AT-244 - 14.d	9.259259259	0.402949	0.51	0.018	0.51393	296	39
AT-244 - 15.d	4.518752824	0.22461	0.675	0.031	0.49662	329	87
AT-244 - 16.d	7.336757153	0.36603	0.546	0.022	0.17797	327	39
AT-244 - 17.d	9.689922481	0.469473	0.457	0.02	0.029789	324	32
AT-244 - 18.d	8.488964346	0.40355	0.52	0.016	0.43962	313	33
AT-244 - 19.d	7.593014427	0.363219	0.563	0.021	0.38538	307	42
AT-244 - 20.d	5.274261603	0.305996	0.646	0.033	0.089322	316	68
AT-244 - 21.d	11.11111111	0.555556	0.408	0.016	0.259	317	25
AT-244 - 22.d	7.23065799	0.350292	0.572	0.019	0.60926	313	43
Grain	Final 238/206	2σ	Final 207/206	2σ	Error Correlation 238/206 vs 207/206	Final 207 Age (Ma)	2σ (Ma)
AT-245 - 1.d	4.454342984	0.190475	0.595	0.015	0.15884	338	70
AT-245 - 2.d	5.899705015	0.348065	0.54	0.032	0.31715	340	68
AT-245 - 3.d	4.524886878	0.327594	0.605	0.036	0.4765	311	85
Grain	Final 238/206	2σ	Final 207/206	2σ	Error Correlation 238/206 vs 207/206	Final 207 Age (Ma)	2σ (Ma)
AT-246 - 1.d	1.964636542	0.150532	0.768	0.018	0.42598	350	160

AT-246 - 2.d	8.561643836	0.329858	0.4164	0.0091	0.57588	400	31
AT-246 - 4.d	9.107468124	0.356668	0.383	0.013	0.16018	404	27
AT-246 - 5.d	8.312551953	0.380042	0.451	0.016	0.50634	380	35
AT-246 - 6.d	5.737234653	0.240286	0.544	0.016	0.59244	423	46
AT-246 - 7.d	5.128205128	0.234057	0.606	0.022	0.049863	370	50
AT-246 - 8.d	6.697923644	0.291604	0.493	0.013	-0.030662	421	34
AT-246 - 9.d	5.847953216	0.24965	0.527	0.015	0.44423	438	66
AT-246 - 10.d	9.891196835	0.41091	0.326	0.013	-0.31342	416	22
AT-246 - 11.d	5.927682276	0.238934	0.543	0.011	0.33867	410	38
AT-246 - 12.d	5.076142132	0.438043	0.609	0.02	0.0756	378	65
AT-246 - 13.d	5.711022273	0.424005	0.57	0.02	0.34972	392	64
AT-246 - 15.d	5.399568035	0.276976	0.571	0.015	0.32011	411	46
AT-246 - 16.d	7.668711656	0.317569	0.461	0.015	0.22601	401	38
AT-246 - 17.d	4.468275246	0.181686	0.638	0.018	0.12306	383	70
AT-246 - 18.d	5.691519636	0.226754	0.558	0.013	0.040136	409	43
AT-246 - 19.d	6.910850035	0.277007	0.498	0.01	0.12271	403	29
AT-246 - 20.d	7.072135785	0.305092	0.498	0.013	0.34358	395	41
AT-246 - 21.d	4.159733777	0.173034	0.639	0.016	0.51577	407	68
AT-246 - 22.d	7.127583749	0.269253	0.485	0.01	0.42811	405	37
AT-246 - 24.d	5.167958656	0.213662	0.58	0.017	0.30906	416	55
AT-246 - 25.d	6.635700066	0.374276	0.504	0.016	-0.17642	412	26
AT-246 - 26.d	5.277044855	0.267333	0.574	0.018	0.2153	416	54
AT-246 - 27.d	2.227171492	0.109126	0.741	0.02	0.38749	402	120
AT-246 - 28.d	5.530973451	0.229438	0.565	0.014	0.45344	411	47
AT-246 - 29.d	4.130524577	0.168906	0.629	0.014	0.2558	427	59

AT-246 - 30.d	4.938271605	0.212163	0.606	0.018	0.3275	394	76
AT-246 - 31.d	6.830601093	0.396585	0.523	0.014	0.40844	380	41
AT-246 - 32.d	7.930214116	0.371041	0.421	0.016	0.21774	427	35
AT-246 - 33.d	6.891798759	0.451221	0.511	0.02	0.088507	389	44
AT-246 - 34.d	5.017561465	0.231619	0.588	0.018	0.41665	418	58
AT-246 - 35.d	6.574621959	0.272322	0.499	0.013	0.14469	422	34

Grain	Final 238/206	2σ	Final 207/206	2σ	Error Correlation 238/206 vs 207/206	Final 207 Age (Ma)	2σ (Ma)
AT-248 - 2.d	8.756567426	0.521407	0.357	0.016	0.3898	439	39
AT-248 - 3.d	11.80637544	0.487867	0.1792	0.0063	0.33389	443	23
AT-248 - 4.d	9.532888465	0.463467	0.297	0.013	0.10828	452	26
AT-248 - 5.d	8.576329331	0.470742	0.354	0.017	0.1956	450	32
AT-248 - 7.d	4.604051565	0.205614	0.564	0.019	0.15233	475	60
AT-248 - 8.d	8.34028357	0.389538	0.364	0.015	-0.13731	452	29
AT-248 - 9.d	7.496251874	0.398976	0.423	0.016	0.52189	443	44
AT-248 - 10.d	8.779631255	0.346869	0.331	0.012	0.39707	460	35
AT-248 - 11.d	9.124087591	0.42457	0.31	0.019	-0.61956	457	20
AT-248 - 12.d	7.027406887	0.301245	0.435	0.014	-0.09839	459	33
AT-248 - 13.d	8.298755187	0.599163	0.371	0.021	0.51353	450	43
AT-248 - 14.d	9.900990099	0.43133	0.225	0.011	0.02276	492	27
AT-248 - 15.d	6.578947368	0.268352	0.479	0.018	0.22013	436	51
AT-248 - 17.d	9.920634921	0.41336	0.243	0.012	-0.073682	477	26
AT-248 - 18.d	4.651162791	0.237967	0.584	0.026	0.022613	437	76
AT-248 - 19.d	5.414185165	0.293134	0.511	0.026	0.04706	481	67
AT-248 - 20.d	6.293266205	0.356447	0.503	0.018	0.078089	417	34
AT-248 - 21.d	5.844535359	0.283516	0.5	0.02	0.11757	462	50

AT-248 - 22.d	5.675368899	0.386518	0.521	0.026	0.46932	449	54
AT-248 - 23.d	9.765625	0.495911	0.293	0.015	0.25329	445	32
AT-248 - 24.d	8.643042351	0.3511	0.343	0.013	0.1613	456	32
AT-248 - 25.d	6.369426752	0.283987	0.454	0.015	0.028785	479	38
AT-248 - 26.d	5.980861244	0.393478	0.492	0.021	-0.10294	459	51
AT-248 - 27.d	10.62699256	0.417852	0.2367	0.0077	0.019089	451.4	21
AT-248 - 28.d	6.45994832	0.275424	0.438	0.016	0.071105	492	44
AT-248 - 29.d	7.112375533	0.369277	0.439	0.021	0.35282	449	57
AT-248 - 30.d	9.00090009	0.453691	0.332	0.016	-0.068743	447	30
AT-248 - 31.d	7.855459544	0.45047	0.425	0.02	0.41265	422	51
AT-248 - 32.d	7.949125596	0.3349	0.385	0.013	0.36669	455	35
Grain	Final 238/206	2σ	Final 207/206	2σ	Error Correlation 238/206 vs 207/206	Final 207 Age (Ma)	2σ (Ma)
AT-252 - 2.d	12.03369434	0.477872	0.1473	0.0047	0.14293	449.6	20
AT-252 - 3.d	11.4416476	0.536736	0.197	0.012	-0.42156	434	20
AT-252 - 4.d	11.04972376	0.476176	0.211	0.011	-0.23326	438	21
AT-252 - 5.d	10.67235859	0.421427	0.2131	0.0077	0.064741	452	24
AT-252 - 6.d	11.4416476	0.445098	0.1829	0.0064	0.18512	445.1	22
AT-252 - 7.d	10.63829787	0.418742	0.2269	0.0069	0.14857	442	25
AT-252 - 8.d	12.23990208	0.479409	0.1604	0.0055	0.40495	433.2	22
AT-252 - 9.d	12.01923077	0.447832	0.1641	0.0059	0.092173	438	21
AT-252 - 10.d	11.65501166	0.461854	0.1829	0.0056	0.23772	437.2	21
AT-252 - 11.d	11.48105626	0.434988	0.1804	0.0058	0.17546	445.8	22
AT-252 - 12.d	10.68376068	0.410914	0.2205	0.0054	0.012684	445.3	20
AT-252 - 13.d	11.84834123	0.477303	0.1616	0.0066	0.0071512	446	21
AT-252 - 14.d	11.40250855	0.442059	0.1478	0.0046	-0.01592	473.3	21

AT-252 - 15.d	12.300123	0.453879	0.1366	0.0045	0.18355	447.6	20
AT-252 - 16.d	11.40250855	0.429057	0.1807	0.005	0.118	448.6	23
AT-252 - 17.d	9.345794393	0.384313	0.272	0.0095	0.16905	460	29
AT-252 - 18.d	11.61440186	0.458641	0.1787	0.006	0.020165	440.1	20
AT-252 - 19.d	11.58748552	0.469944	0.1764	0.0077	0.013113	441.3	19
AT-252 - 20.d	12.00480192	0.461169	0.1656	0.0062	0.29678	437.2	22
AT-252 - 21.d	12.06272618	0.451079	0.1694	0.0087	0.2287	433.1	21
AT-252 - 22.d	12.45330012	0.480763	0.1419	0.0046	0.39423	438.4	21
AT-252 - 23.d	11.7370892	0.454606	0.158	0.0053	0.27096	453	22
AT-252 - 24.d	11.79245283	0.500623	0.1744	0.0073	0.080669	438.1	21
AT-252 - 25.d	11.66861144	0.449316	0.1653	0.006	0.18966	449.2	20
AT-252 - 26.d	11.60092807	0.767115	0.192	0.019	0.22493	433	32
AT-252 - 27.d	12.69035533	0.773017	0.1237	0.01	-0.090886	441.4	19
AT-252 - 28.d	11.26126126	0.443856	0.2043	0.0067	0.49951	436	25
AT-252 - 29.d	7.087172218	0.406847	0.363	0.025	0.079767	492	53
AT-252 - 30.d	7.776049767	0.338615	0.38	0.015	-0.31686	428	37
AT-252 - 31.d	11.70960187	0.589594	0.174	0.012	0.1886	442	26
AT-252 - 32.d	11.89060642	0.466576	0.1547	0.0058	0.45071	449.7	23
AT-252 - 33.d	10.84598698	0.411724	0.2055	0.0071	0.068112	450.8	23
AT-252 - 34.d	12.06272618	0.46563	0.148	0.0063	-0.046975	447.7	20
AT-252 - 35.d	11.3507378	0.450937	0.175	0.0058	0.12071	455	21
AT-252 - 36.d	8.764241893	0.476234	0.313	0.015	0.047132	450	39
AT-252 - 37.d	6.485084306	0.370096	0.435	0.024	0.1344	443	54
AT-252 - 38.d	7.757951901	0.367134	0.368	0.018	0.35721	444	41
AT-252 - 39.d	9.920634921	0.442886	0.278	0.014	0.11269	428	33

AT-252 - 40.d	10.12145749	0.409776	0.252	0.01	-0.21164	442	23
AT-252 - 41.d	12.07729469	0.495928	0.16	0.0081	-0.1833	438.4	19
Grain	**Final 238/206**	**2σ**	**Final 207/206**	**2σ**	**Error Correlation 238/206 vs 207/206**	**Final 207 Age (Ma)**	**2σ (Ma)**
AT-253 - 1.d	3.5932447	0.154937	0.663	0.015	0.42446	372	65
AT-253 - 2.d	5.920663114	0.255896	0.528	0.0091	0.11586	408	31
AT-253 - 3.d	4.266211604	0.200206	0.616	0.017	0.53894	402	80
AT-253 - 4.d	3.894080997	0.151639	0.653	0.013	0.46111	363	75
AT-253 - 5.d	4.323389537	0.173833	0.612	0.014	0.57029	405	63
AT-253 - 6.d	4.321521175	0.177418	0.615	0.017	0.55052	398	76
AT-253 - 7.d	2.914602157	0.135919	0.686	0.015	0.055661	390	94
AT-253 - 8.d	3.812428517	0.174415	0.625	0.015	0.56238	430	76
AT-253 - 10.d	3.164556962	0.130188	0.671	0.018	0.35838	400	100
AT-253 - 11.d	3.385240352	0.148978	0.651	0.015	0.28193	421	73
AT-253 - 12.d	3.249918752	0.137306	0.67	0.012	0.45194	393	60
AT-253 - 13.d	3.337783712	0.13369	0.659	0.013	0.33185	408	69
AT-253 - 15.d	3.382949932	0.137332	0.658	0.018	0.62486	410	100
AT-253 - 17.d	4.133939644	0.170895	0.62	0.016	0.61464	410	67
AT-253 - 19.d	3.841721091	0.162347	0.642	0.016	0.44918	392	94
AT-253 - 20.d	3.623188406	0.15753	0.649	0.011	0.43425	399	56
AT-253 - 21.d	3.567606136	0.152734	0.652	0.015	0.35893	399	67
AT-253 - 22.d	3.94788788	0.607847	0.656	0.023	0.36174	352	98
AT-253 - 23.d	4.306632214	0.278206	0.627	0.016	0.74288	363	84
AT-253 - 24.d	5.46149645	0.289331	0.573	0.014	0.42222	368	58
AT-253 - 25.d	4.376367615	0.191526	0.609	0.015	0.38414	397	57
AT-253 - 26.d	3.681885125	0.149119	0.649	0.014	-0.017681	390	68

AT-253 - 27.d	4.191114837	0.19322	0.632	0.015	0.24346	377	66
AT-253 - 28.d	3.799392097	0.158789	0.63	0.015	0.36401	422	67
AT-253 - 29.d	4.545454545	0.247934	0.594	0.022	-0.48609	407	49
AT-253 - 30.d	3.716090673	0.151903	0.633	0.015	0.20397	423	65
AT-253 - 32.d	4.545454545	0.200413	0.6	0.012	0.39048	405	44
AT-253 - 33.d	3.474635163	0.132804	0.642	0.015	0.32002	431	86
AT-253 - 34.d	4.376367615	0.183865	0.611	0.015	0.22839	400	53
AT-253 - 35.d	3.865481252	0.14942	0.64	0.016	0.30055	391	76
AT-253 - 36.d	3.785011355	0.157589	0.64	0.015	0.32717	396	73

Grain	Final 238/206	2σ	Final 207/206	2σ	Error Correlation 238/206 vs 207/206	Final 207 Age (Ma)	2σ (Ma)
AT-254 - 1.d	11.66861144	0.503779	0.241	0.0088	0.084308	408	24
AT-254 - 2.d	10.81081081	0.420745	0.276	0.011	0.3328	413	29
AT-254 - 3.d	11.45475372	0.432998	0.221	0.0074	0.037871	429	22
AT-254 - 4.d	11.09877913	0.43114	0.2655	0.0088	0.19834	411	23
AT-254 - 5.d	11.27395716	0.432147	0.2355	0.0076	0.29342	425.8	22
AT-254 - 6.d	10.75268817	0.520291	0.265	0.013	-0.67768	422	15
AT-254 - 7.d	11.80637544	0.432111	0.2168	0.0052	0.57645	419.4	23
AT-254 - 8.d	11.45475372	0.432998	0.2397	0.0055	-0.026136	414.6	20
AT-254 - 9.d	11.60092807	0.444119	0.2301	0.0071	0.024635	417.4	20
AT-254 - 10.d	10.31991744	0.394053	0.286	0.0072	0.19171	426	24
AT-254 - 11.d	10.70663812	0.401212	0.2627	0.0081	0.39989	428.2	26
AT-254 - 12.d	10.24590164	0.398918	0.2921	0.0072	0.26327	425	24
AT-254 - 13.d	11.52073733	0.438	0.2219	0.0058	0.47235	426.2	23
AT-254 - 14.d	10.46025105	0.437667	0.2609	0.0099	-0.29404	433.4	17
AT-254 - 15.d	11.69590643	0.451421	0.215	0.0058	0.29868	424.5	21

AT-254 - 16.d	11.87648456	0.465468	0.2004	0.0069	-0.31911	427.3	16
AT-254 - 17.d	10.28806584	0.423377	0.3023	0.0099	0.56435	417	32
AT-254 - 18.d	11.62790698	0.459708	0.2257	0.0087	-0.030922	419.3	21
AT-254 - 19.d	10.46025105	0.393901	0.276	0.0073	0.41699	426.9	27
AT-254 - 20.d	13.19261214	0.504731	0.1601	0.0056	-0.17658	409.4	18
AT-254 - 21.d	10.3950104	0.399808	0.287	0.0084	0.25704	422	24
AT-254 - 22.d	11.99040767	0.460064	0.2025	0.0084	-0.049566	422.2	20
AT-254 - 23.d	10.92896175	0.418048	0.2592	0.0061	0.49632	422	23
AT-254 - 24.d	10.63829787	0.418742	0.2803	0.0079	0.32571	418	24
AT-254 - 25.d	10.15228426	0.391662	0.288	0.0082	0.46695	432	28
AT-254 - 26.d	11.33786848	0.437061	0.2316	0.0053	0.26363	425	20
AT-254 - 27.d	11.46788991	0.433991	0.239	0.0087	0.079803	414.7	25
AT-254 - 28.d	10.11122346	0.398724	0.3181	0.0096	0.44827	410	27
AT-254 - 29.d	11.70960187	0.452479	0.2115	0.0051	0.6066	426.3	22
AT-254 - 30.d	11.79245283	0.444998	0.2024	0.0068	0.023187	429.1	20
AT-254 - 31.d	10.49317943	0.407395	0.2835	0.0077	0.18386	421	23
AT-254 - 32.d	11.72332943	0.467284	0.1964	0.0082	-0.32987	435.5	18
AT-254 - 33.d	11.68224299	0.450367	0.232	0.0085	-0.20664	412.8	20
AT-254 - 34.d	11.11111111	0.432099	0.2167	0.0066	-0.21606	444.7	18
AT-254 - 35.d	10.47120419	0.416655	0.2831	0.0079	0.26084	422	24
AT-254 - 36.d	12.01923077	0.476724	0.2169	0.0065	0.18878	412.1	20
AT-254 - 37.d	12.43781095	0.479567	0.1943	0.0067	0.040631	412.2	19
AT-254 - 38.d	7.692307692	0.343195	0.447	0.014	0.1967	406	41
AT-254 - 39.d	10.81081081	0.420745	0.2659	0.0078	0.20823	420	24
AT-254 - 40.d	11.09877913	0.468095	0.2198	0.0093	-0.079915	443	21

Grain	Final 238/206	2σ	Final 207/206	2σ	Error Correlation 238/206 vs 207/206	Final 207 Age (Ma)	2σ (Ma)
AT-255 - 1.d	9.496676163	0.505046	0.2188	0.019	0.62836	520	31
AT-255 - 2.d	4.734848485	0.224188	0.518	0.02	0.30896	548	59
AT-255 - 3.d	5.889281508	0.294811	0.471	0.021	0.47507	505	54
AT-255 - 4.d	5.361930295	0.264503	0.524	0.023	0.39426	479	59
AT-255 - 5.d	8.920606601	0.421759	0.26	0.015	0.035431	516	33
AT-255 - 6.d	9.746588694	0.379984	0.2258	0.0099	0.44397	501	32
AT-255 - 7.d	8.278145695	0.349491	0.291	0.013	0.19455	527	39
AT-255 - 8.d	8.361204013	0.342558	0.2965	0.0095	0.28238	517	29

12. APPENDIX D: THERMAL HISTORY MODELS

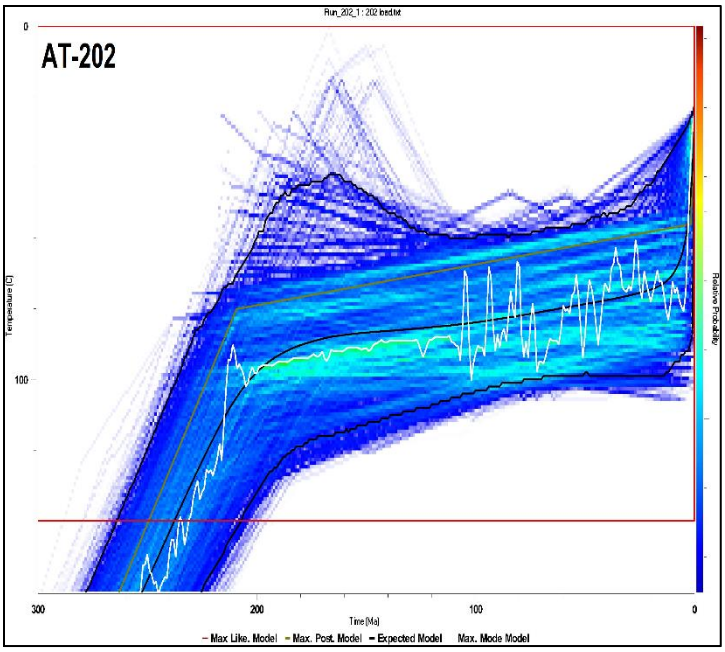

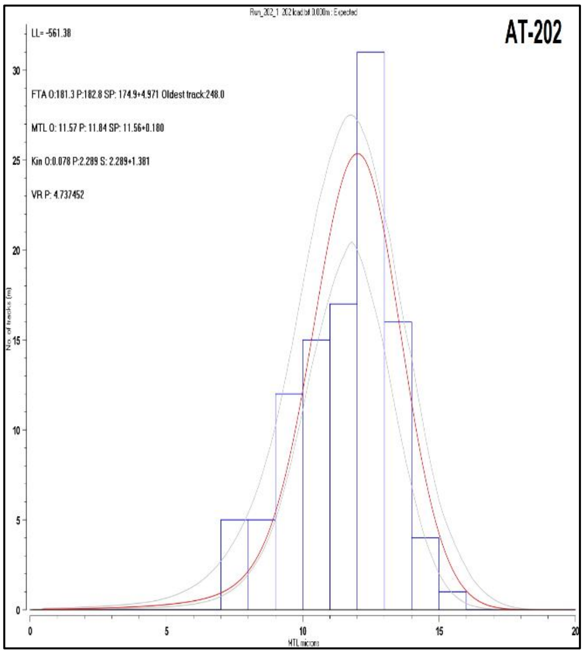

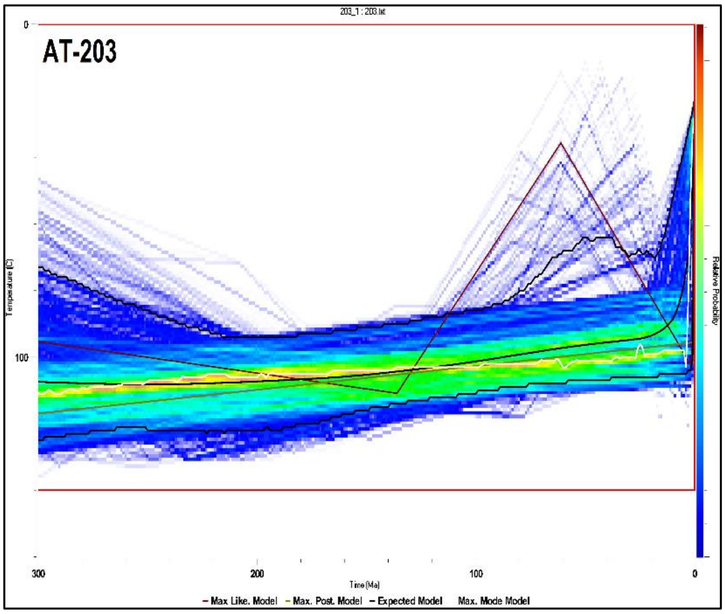
AT-203
Temperature (C)
Relative Probability
Time (Ma)
Max Like. Model
Max. Post. Model
Expected Model
Max. Mode Model

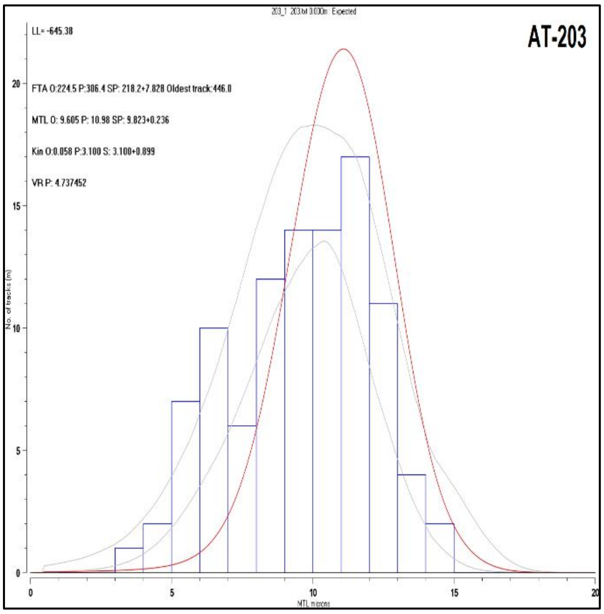
AT-203
LL= -645.38
FTA O:224.5 P:306.4 SP: 218.2+7.828 Oldest track:446.0
MTL O: 9.605 P: 10.98 SP: 9.823+0.236
Kin O:0.058 P:3.100 S: 3.100+0.899
VR P: 4.737452
MTL microns

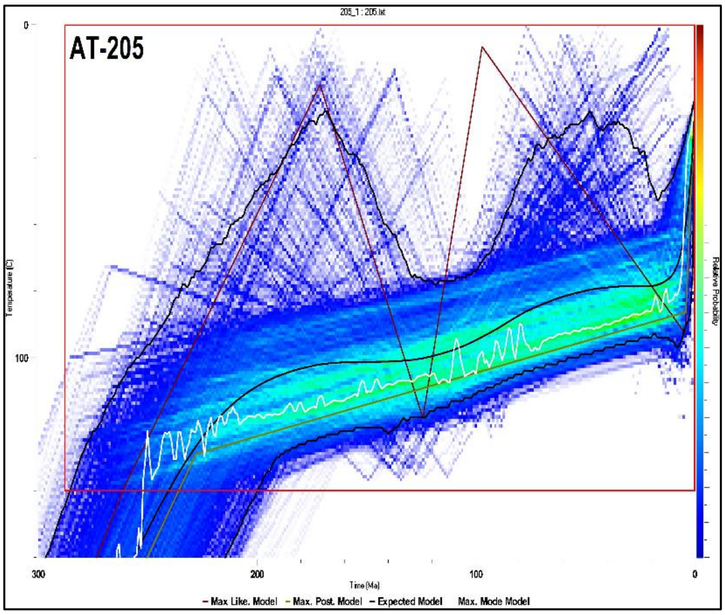
AT-205
Temperature (C)
Relative Probability
Time (Ma)
Max Like. Model
Max. Post. Model
Expected Model
Max. Mode Model

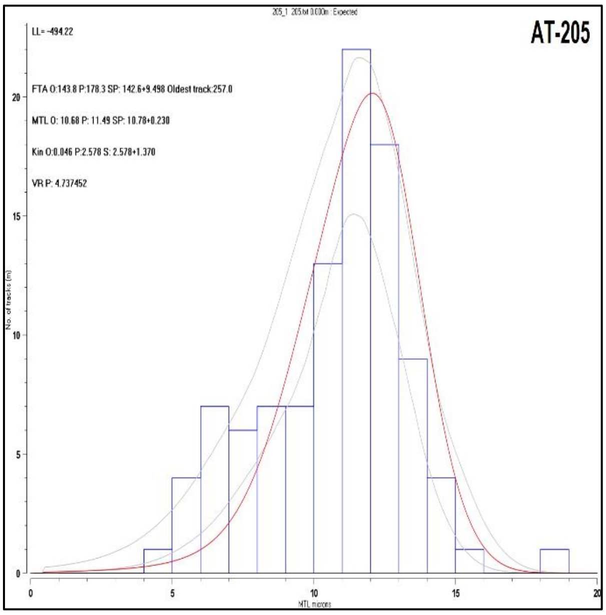
AT-205
LL= -494.22
FTA O:143.8 P:178.3 SP: 142.6+9.498 Oldest track:257.0
MTL O: 10.68 P: 11.49 SP: 10.78+0.230
Kin O:0.046 P:2.578 S: 2.578+1.370
VR P: 4.737452
MTL microns

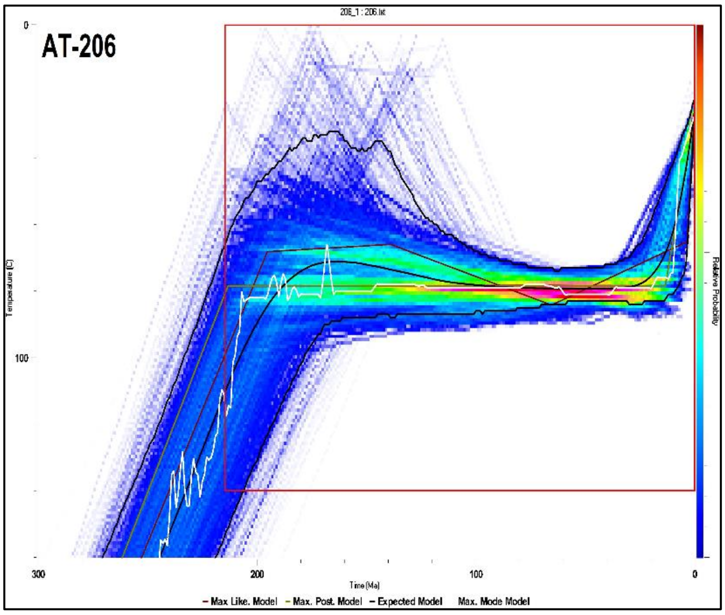
AT-206
Temperature (C)
Relative Probability
Time (Ma)
Max Like. Model
Max. Post. Model
Expected Model
Max. Mode Model

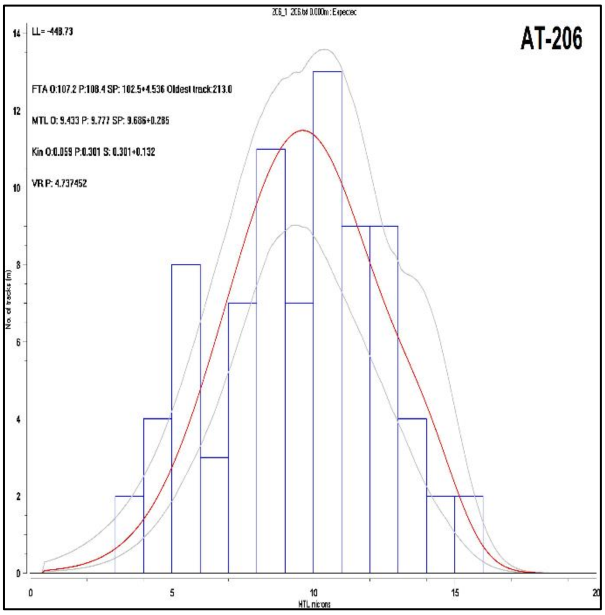
AT-206
LL= -448.73
FTA O:107.2 P:108.4 SP: 102.5+4.536 Oldest track:213.0
MTL O: 9.433 P: 9.777 SP: 9.686+0.285
Kin O:0.059 P:0.301 S: 0.301+0.132
VR P: 4.737452
MTL microns

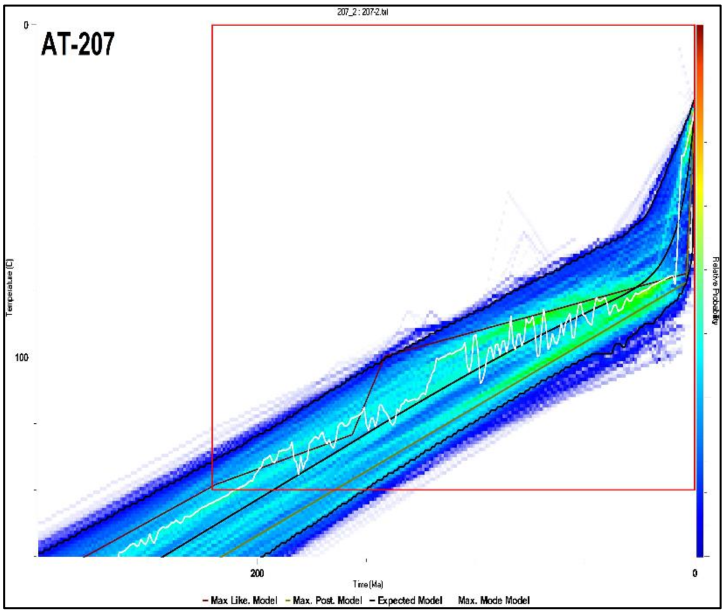
AT-207
Temperature (C)
Time (Ma)
Relative Probability
- Max Like. Model - Max. Post. Model - Expected Model Max. Mode Model

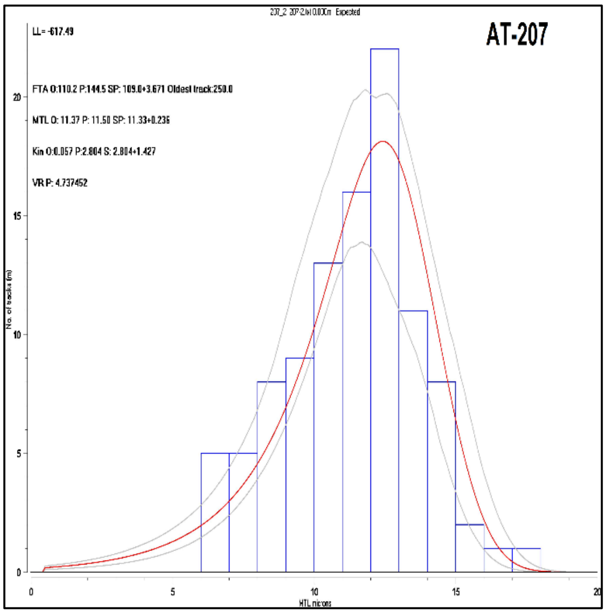
AT-207
No. of tracks (m)
HTL microns

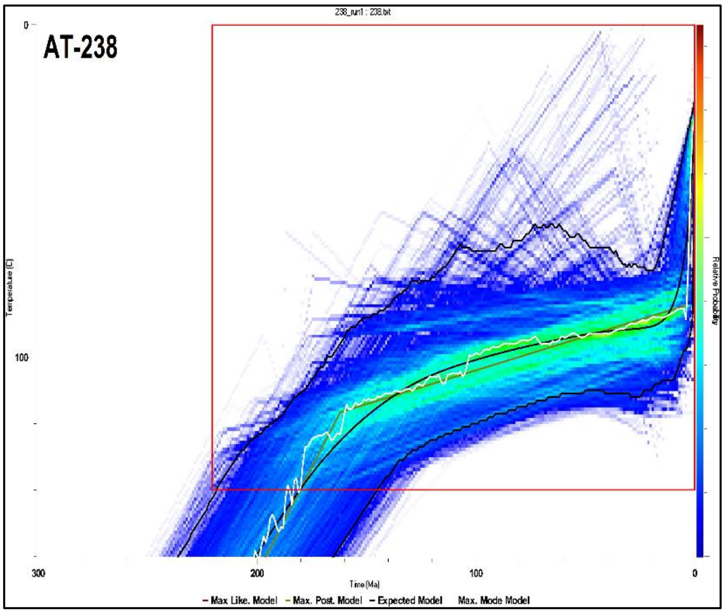
AT-238
Temperature (C)
Time (Ma)
Relative Probability
- Max Like. Model - Max. Post. Model - Expected Model Max. Mode Model

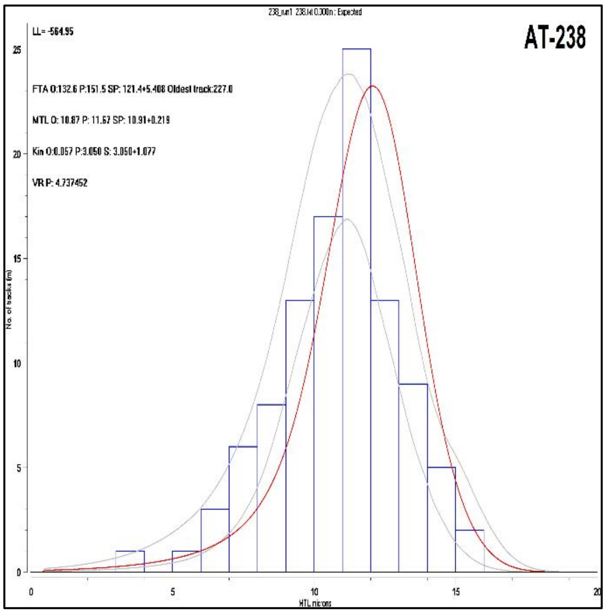
AT-238
No. of tracks (m)
HTL microns

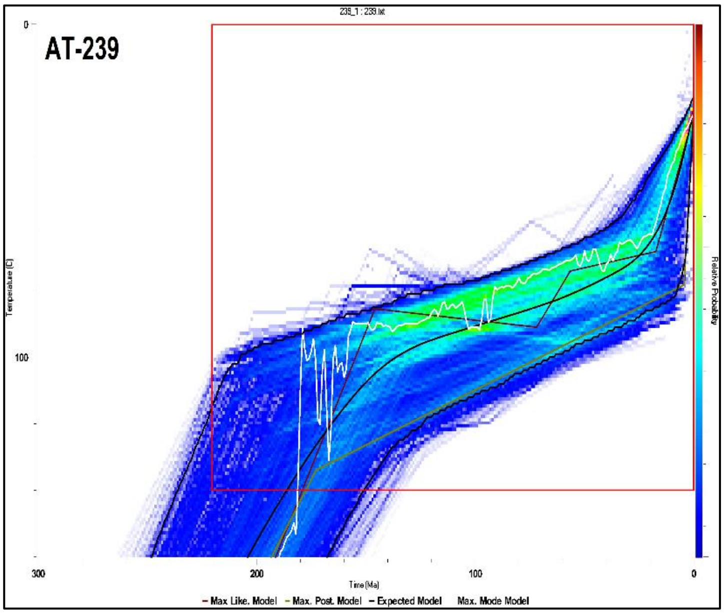
AT-239
Temperature (C)
Time (Ma)
Relative Probability
- Max Like. Model - Max. Post. Model - Expected Model Max. Mode Model

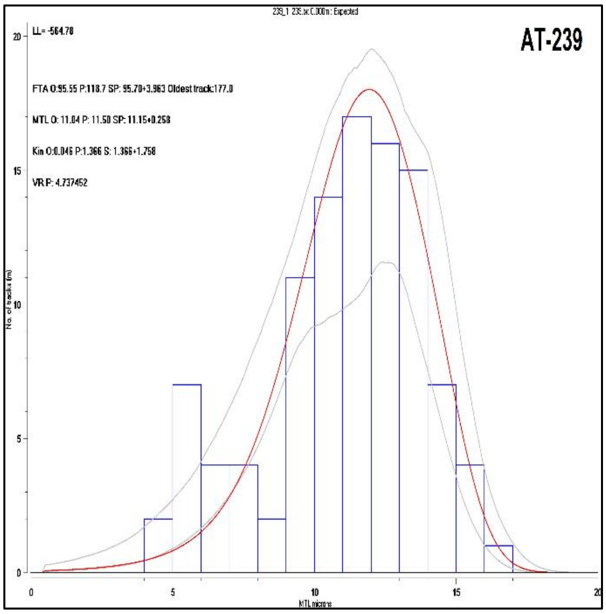
AT-239
No. of tracks (m)
HTL microns

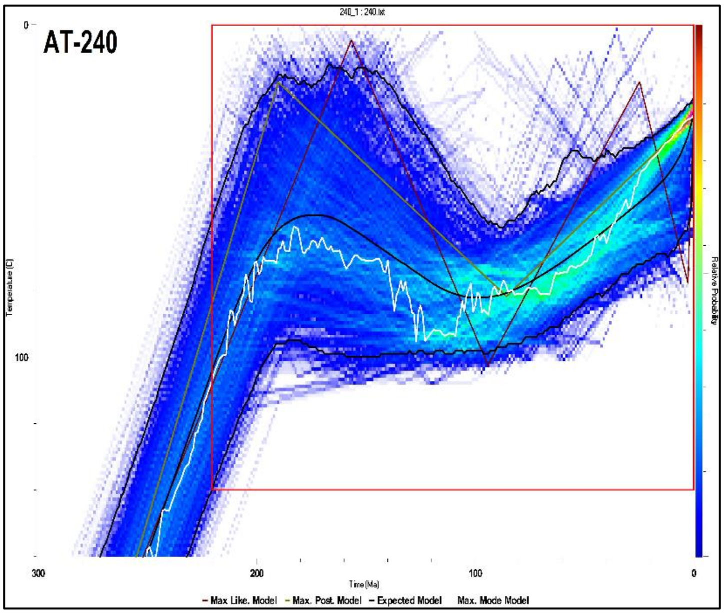
AT-240
Temperature (C)
Time (Ma)
Relative Probability
Max Like. Model
Max. Post. Model
Expected Model
Max. Mode Model

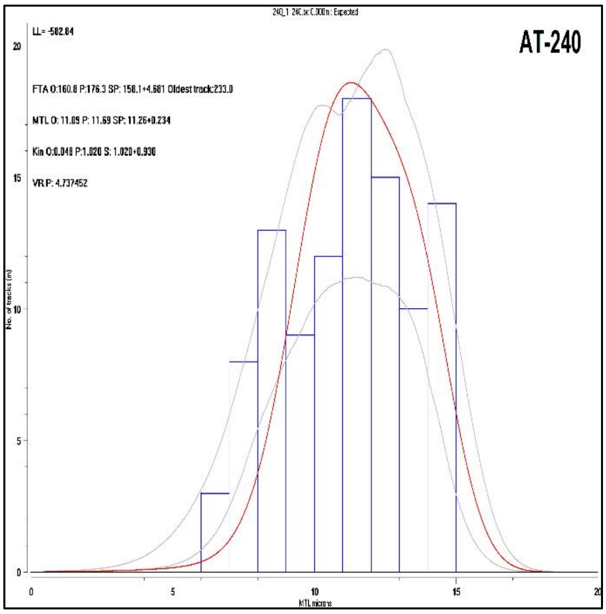
LL= -582.84
AT-240
FTA O:160.8 P:176.3 SP: 158.1+4.681 Oldest track:233.0
MTL O: 11.09 P: 11.69 SP: 11.26+0.234
Kin O:0.048 P:1.020 S: 1.020+0.930
VR P: 4.737452
No. of tracks (m)
MTL microns

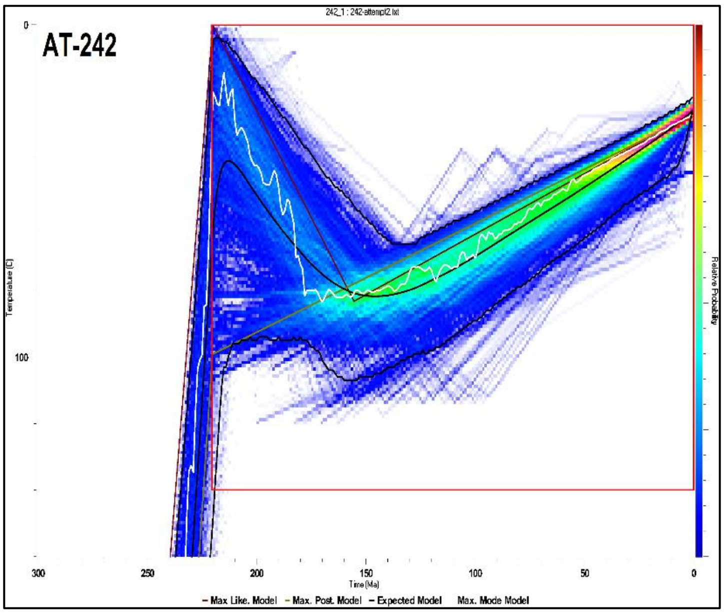
AT-242
Temperature (C)
Time (Ma)
Relative Probability
Max Like. Model
Max. Post. Model
Expected Model
Max. Mode Model

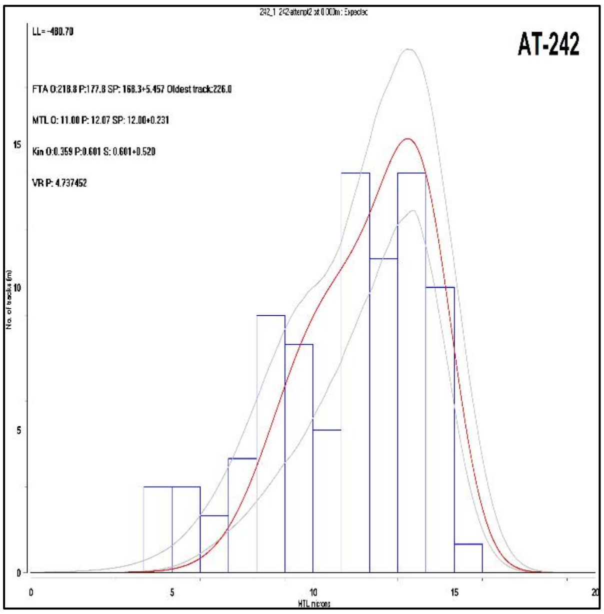
LL= -480.70
AT-242
FTA O:218.8 P:177.8 SP: 168.3+5.457 Oldest track:226.0
MTL O: 11.00 P: 12.07 SP: 12.00+0.231
Kin O:0.359 P:0.601 S: 0.601+0.520
VR P: 4.737452
No. of tracks (m)
MTL microns

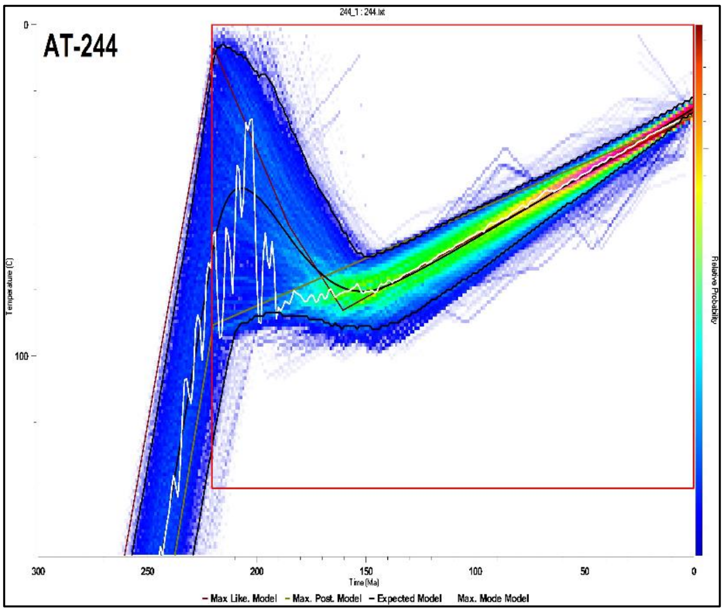
AT-244
Temperature (C)
Time (Ma)
Relative Probability
Max Like. Model
Max. Post. Model
Expected Model
Max. Mode Model

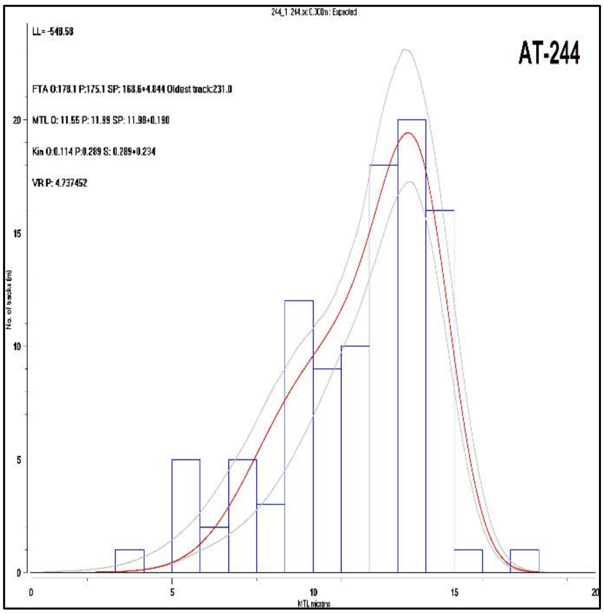
LL= -548.58
AT-244
FTA O:178.1 P:175.1 SP: 168.6+4.844 Oldest track:231.0
MTL O: 11.55 P: 11.99 SP: 11.98+0.190
Kin O:0.114 P:0.289 S: 0.289+0.234
VR P: 4.737452
No. of tracks (m)
MTL microns

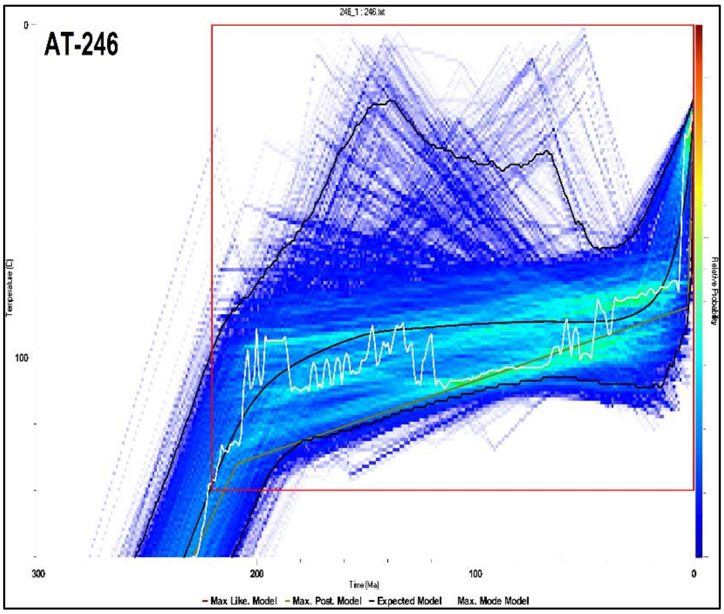
246_1 : 246.txt
AT-246
Temperature (C)
Time (Ma)
Relative Probability
Max Like. Model
Max. Post. Model
Expected Model
Max. Mode Model

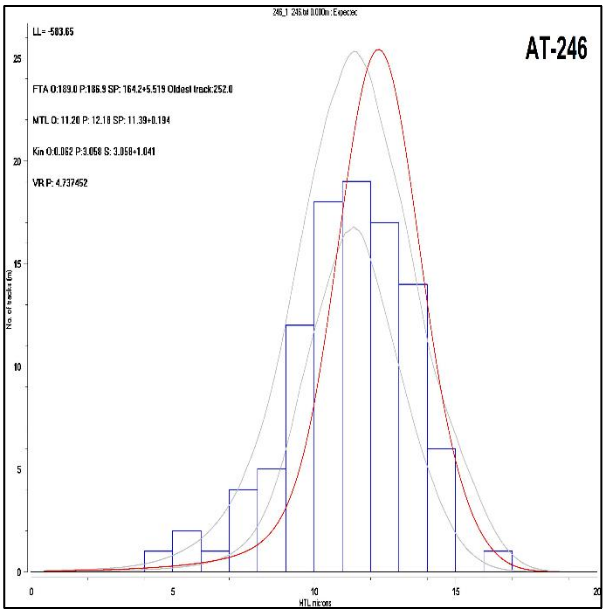
246_1 246.txt 0.000m : Expected
AT-246
LL= -583.65
FTA O:189.0 P:186.9 SP: 164.2+5.519 Oldest track:252.0
MTL O: 11.20 P: 12.18 SP: 11.39+0.194
Kin O:0.062 P:3.058 S: 3.058+1.041
VR P: 4.737452
No. of tracks (m)
HTL microns

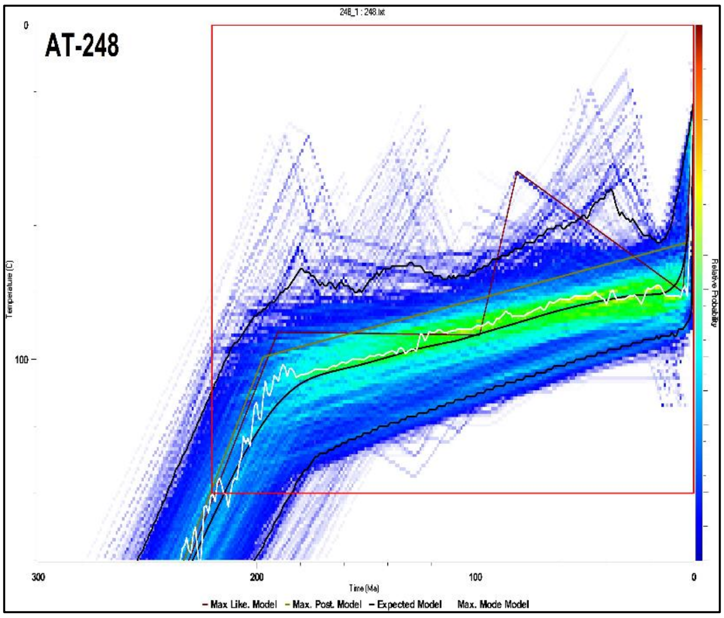
248_1 : 248.txt
AT-248
Temperature (C)
Time (Ma)
Relative Probability
Max Like. Model
Max. Post. Model
Expected Model
Max. Mode Model

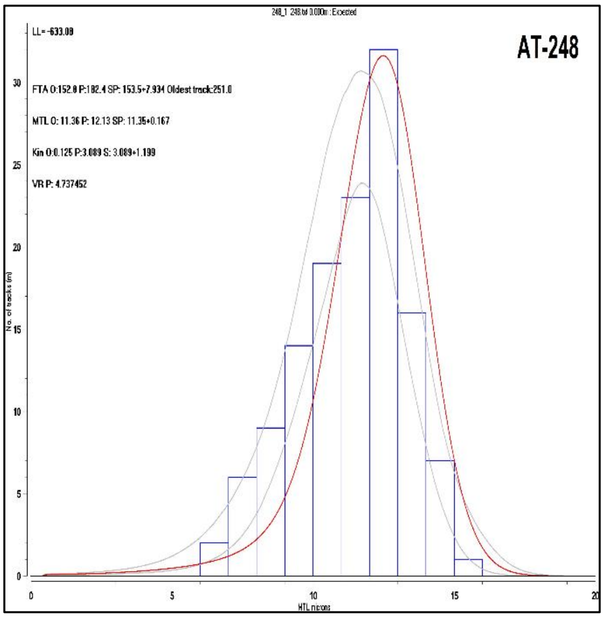
248_1 248.txt 0.000m : Expected
AT-248
LL= -633.08
FTA O:152.0 P:182.4 SP: 153.5+7.934 Oldest track:251.0
MTL O: 11.36 P: 12.13 SP: 11.35+0.167
Kin O:0.125 P:3.089 S: 3.089+1.199
VR P: 4.737452
No. of tracks (m)
HTL microns

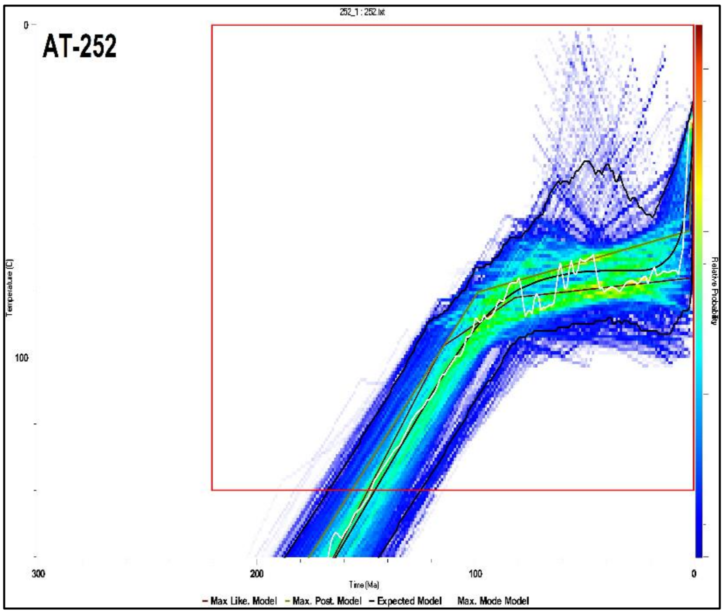
252_1 : 252.txt
AT-252
Temperature (C)
Time (Ma)
Relative Probability
Max Like. Model
Max. Post. Model
Expected Model
Max. Mode Model

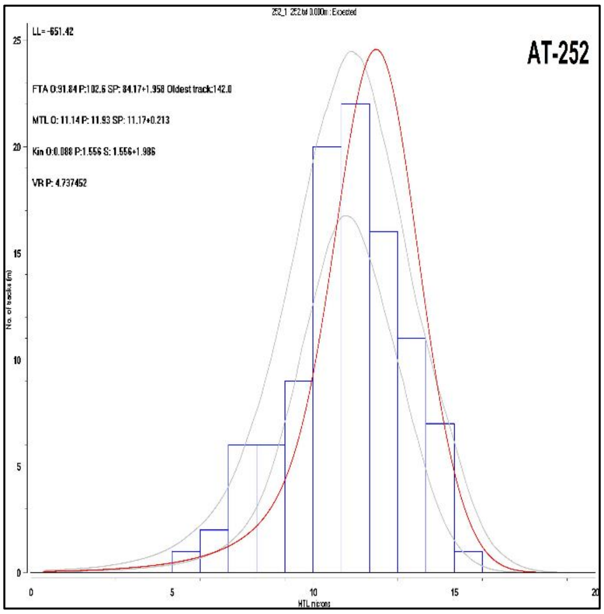
252_1 252.txt 0.000m : Expected
AT-252
LL= -651.42
FTA O:91.84 P:102.6 SP: 84.17+1.958 Oldest track:142.0
MTL O: 11.14 P: 11.93 SP: 11.17+0.213
Kin O:0.088 P:1.556 S: 1.556+1.986
VR P: 4.737452
No. of tracks (m)
HTL microns

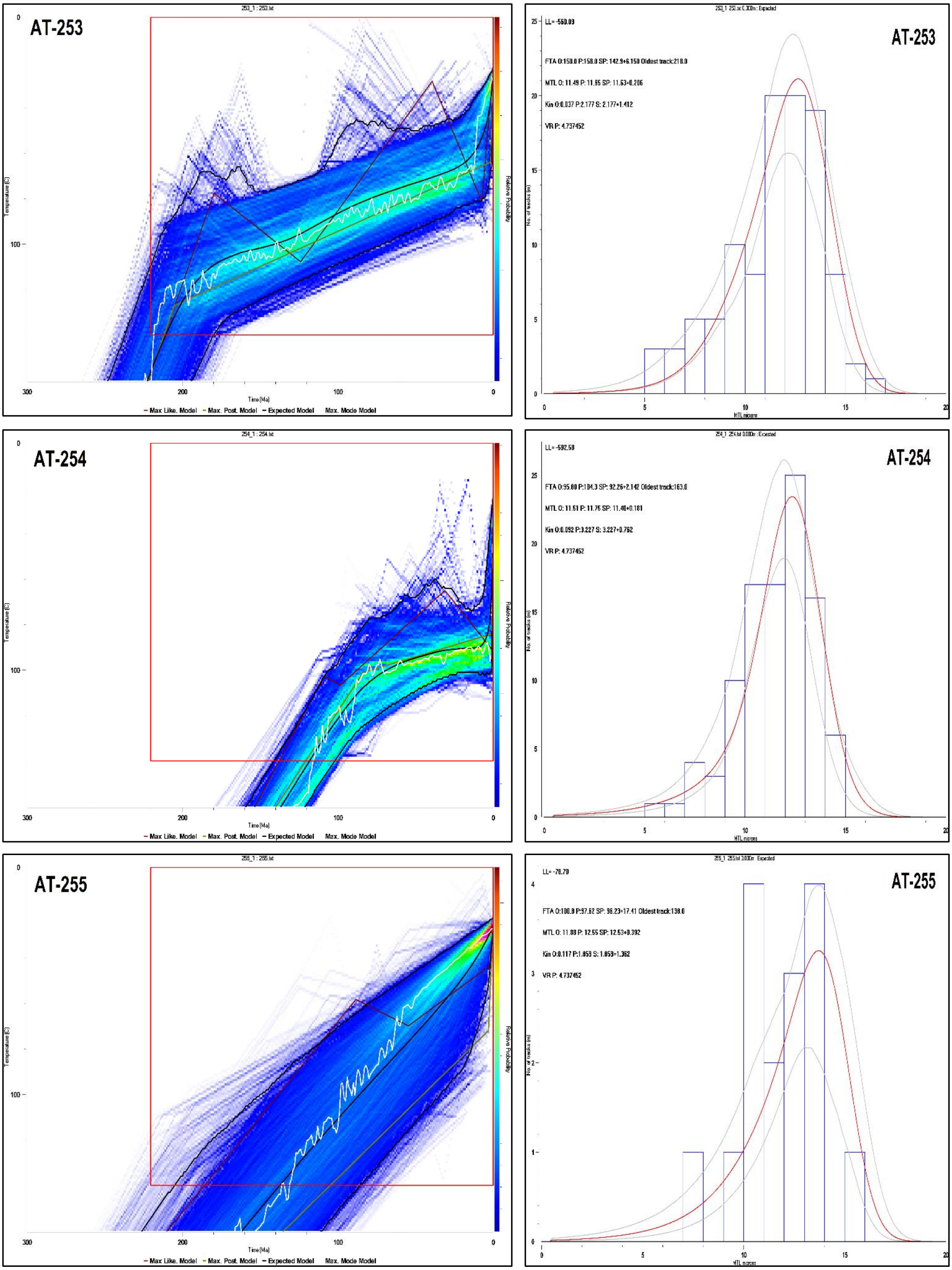

Figure 20 – Additional thermal history models and mean track length histograms.